The Flow Past Elliptic-nosed Cylinders and Bodies of Revolution in Supersonic Air Streams*

D. W. HOLDER and A. CHINNECK
(Aerodynamics Division, National Physical Laboratory)

Summary: The flow past families of two-dimensional cylinders and bodies of revolution with elliptic noses at zero incidence has been examined at free stream Mach numbers between 1·42 and 1·82. The observations include schlieren photographs and measurements of the pressure distributions at the surface.

The measured pressure distributions and positions of the detached bow waves are found to be in fair agreement with values calculated by a number of methods. The drag coefficients of the slender two-dimensional elliptic noses are considerably higher than those calculated for wedges of the same axis ratio with attached shock waves, but the drags become almost equal when the axis ratio approaches the value for subsonic flow behind the bow wave of the wedge. For most axis ratios the drag coefficients of the elliptic-nosed bodies of revolution are lower than those for cones of the same axis ratio.

1. Introduction

The general nature of the flow past a blunt-nosed body placed in a supersonic air stream is illustrated by Fig. 1 (p. 321) which shows a 12 per cent. thick conventional aerofoil† held in a wind tunnel giving a free stream Mach number of 1·60. The bow shock wave is curved and detached from the nose, and there is a limited region of subsonic flow between the apex of the bow wave and the body. Farther downstream the flow becomes supersonic again, and the conditions over the rear of the aerofoil are similar to those for a sharp leading edge and an attached bow wave. A flow which is physically similar to that described for a two-dimensional aerofoil occurs at the front of a blunt-nosed body of revolution.

In addition to its practical importance, the study of the motion near the front of a blunt-nosed body is of fundamental interest because it is an example of mixed subsonic and supersonic flow in which the interaction between a shock wave and a boundary layer is not usually involved. The present investigation was designed to provide systematic information on the conditions close to the noses of two- and three-dimensional bodies with detached bow waves. This information is compared with some of the existing theories, and it is hoped that it will be of value in connection with further theoretical work and for design purposes.

*Some preliminary results of this investigation are described in A.R.C. 12,418, 12,660, 12,495.

†The front half of this two-dimensional aerofoil (EC.1250) is a semi-ellipse of axis ratio $\lambda = 8{\cdot}33$ (*see* Fig. 2).

Originally received November 1951.
[The Aeronautical Quarterly, Volume IV, February 1954]

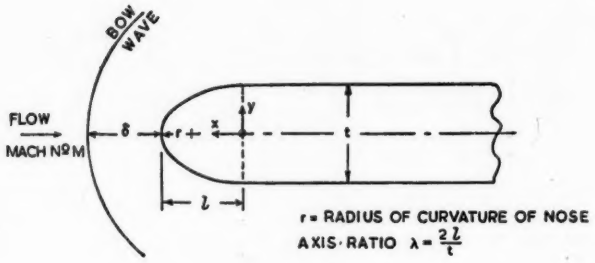

Fig. 2.
Sketch showing the notation.

Notation

C_D	drag coefficient, defined by equations (1) or (2)
D	drag, defined by equations (3) or (4)
H_2	total head behind a normal shock wave
l	length of body nose (*see* Fig. 2)
M	free stream Mach number
p	static pressure at body surface
p_0	free stream static pressure
r	radius of curvature of body nose
t	plate or body thickness (*see* Fig. 2)
U	free stream velocity
x, y	rectangular co-ordinates (*see* Fig. 2)
γ	ratio of specific heats
δ	distance of bow wave ahead of body nose (*see* Fig. 2)
$\lambda = 2l/t$	
ρ	free stream density
ϕ	surface angle (*see* equation (5))
ψ	false angle given by equation (6)

2. The Apparatus and Techniques used in the Experiments

The observations were made in the 9 in. × 3 in. induced-flow tunnel[1] at the N.P.L. which can be fitted with liners designed to give uniform supersonic flows at Mach numbers of 1·4, 1·6 and 1·8. The actual mean Mach numbers obtained with these liners were calculated from measurements with a suitably designed static tube[2] traversed along the tunnel axis in the position occupied by the model under test.

The noses of the two-dimensional plates and of the bodies of revolution tested had elliptic generators; the axis ratios λ (*see* Fig. 2) used were 8, 4, 2, 1, 0·5, and 0 (square nose). All the plates were 3/16 in. thick; they were supported by tongues passing through slots cut in the glass side walls of the tunnel. Pressure holes were

fitted in the surface of each plate and were connected to the manometer by hypodermic tubing passing out of the tunnel through the supporting tongues. The pressure holes were of 0·005 in. diameter in regions of high surface curvature, and 0·01 in. diameter elsewhere. The bodies of revolution were 9/16 in. diameter, and were supported on a sting. The sides of the plates and bodies of revolution were parallel downstream of the nose sections.

Toepler-schlieren and direct-shadow photographs were taken with a spark light source[3] giving an exposure of the order of 1 microsecond. The optical system used in most of the work was based on 9 in. diameter spherical mirrors of 9 ft. focal length, but some of the schlieren photographs were taken with an apparatus[4] fitted with 2 in. diameter, 14 in. focal length lenses, giving a larger working range and a higher image magnification.

Care was taken in the experimental work to ensure that the reflections of the bow wave from the tunnel walls struck the model well downstream of the length on which the pressures were measured, and that the region of subsonic flow behind the bow wave did not extend to the tunnel walls. Unless otherwise stated, therefore, the observations are free from tunnel interference.

The tunnel operated with atmospheric intake pressure, and the Reynolds number per inch was approximately $0{\cdot}4 \times 10^6$.

3. Expression of the Results

The symbols used in expressing the results are defined in Fig. 2. The nose shape is specified by the ratio λ of the semi-axis l parallel to the free stream to the perpendicular semi-axis $t/2$.

The measured static pressure p at the surface is expressed in non-dimensional form by dividing by the total head H_2 behind a normal shock wave. This total head has been calculated from the measured values of the Mach number and total head upstream of the bow wave. In determining the position of the sonic point it is assumed that it is sufficiently accurate to take the total head just outside the boundary layer equal to H_2 so that the sonic point occurs when

$$\frac{p}{H_2} = \left(\frac{2}{\gamma+1}\right)^{\frac{\gamma}{\gamma-1}} \quad (i.e.\ 0{\cdot}528 \text{ for } \gamma = 1{\cdot}40).$$

The following coefficients are used in calculating the drag due to the noses of the plates and bodies

$$C_D = \frac{D}{\frac{1}{2}\rho U^2 t} \quad \text{for the plates} \quad . \quad . \quad . \quad . \quad (1)$$

and

$$C_D = \frac{D}{\frac{1}{2}\rho U^2 \frac{\pi}{4} t^2} \quad \text{for the bodies,} \quad . \quad . \quad . \quad (2)$$

KRESGE-HOOKER SCIENTIFIC LIBRARY WAYNE UNIVERSITY

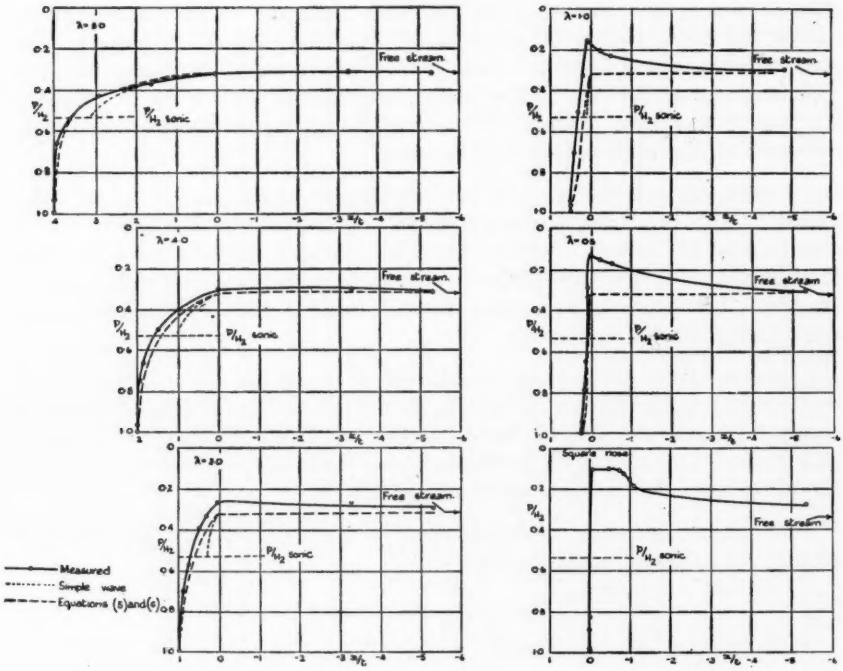

Fig. 3.
Pressures on the two-dimensional cylinders at $M=1{\cdot}42$.

where the drag per unit span of the plates is given by

$$D=2\int_0^{t/2}(p-p_0)\,dy, \qquad (3)$$

and the drag on the nose of the bodies by

$$D=2\pi\int_0^{t/2}(p-p_0)\,y\,dy, \qquad (4)$$

where p_0 is the free stream static pressure, and the quantity $\frac{1}{2}\rho U^2$ is based on free stream conditions.

4. Discussion of the Results

4.1. Two-dimensional cylinders

The pressure distributions measured on the surfaces of the two-dimensional cylinders are shown in Figs. 3, 4, 5 and 6. (The results for the square-nosed plate at $M=1{\cdot}42$ are subject to tunnel interference, and should be used with caution.)

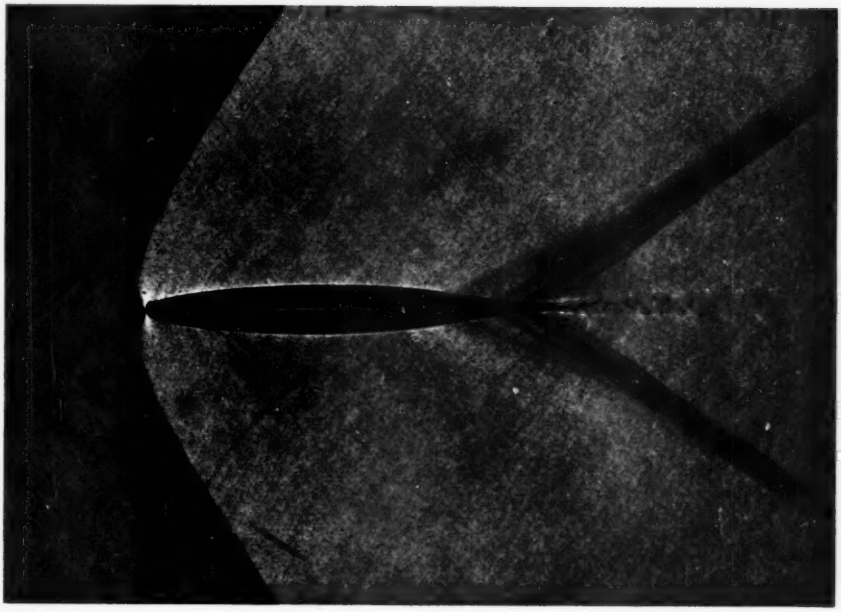

Fig. 1.
Flow past a round-nosed aerofoil.

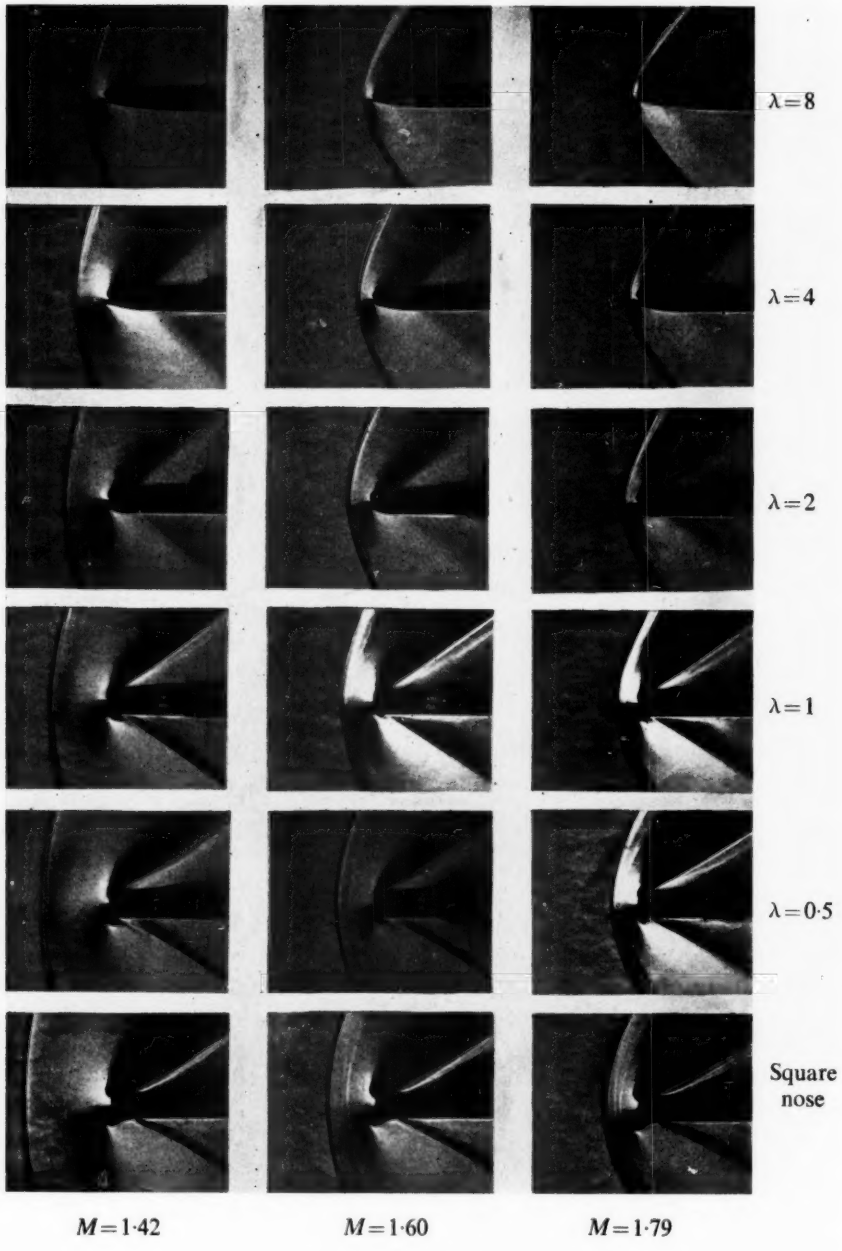

Fig. 7.
Schlieren photographs for the two-dimensional cylinders.

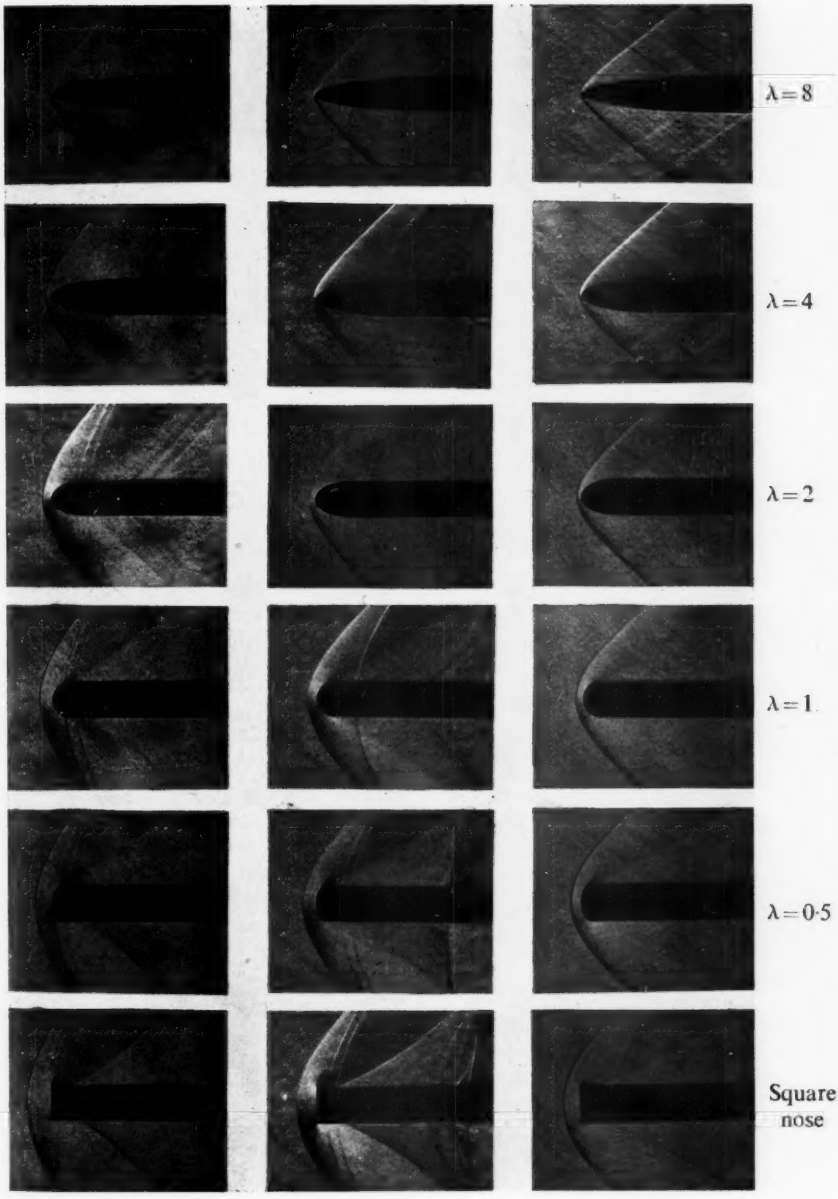

Fig. 14.
Schlieren photographs for the bodies of revolution.

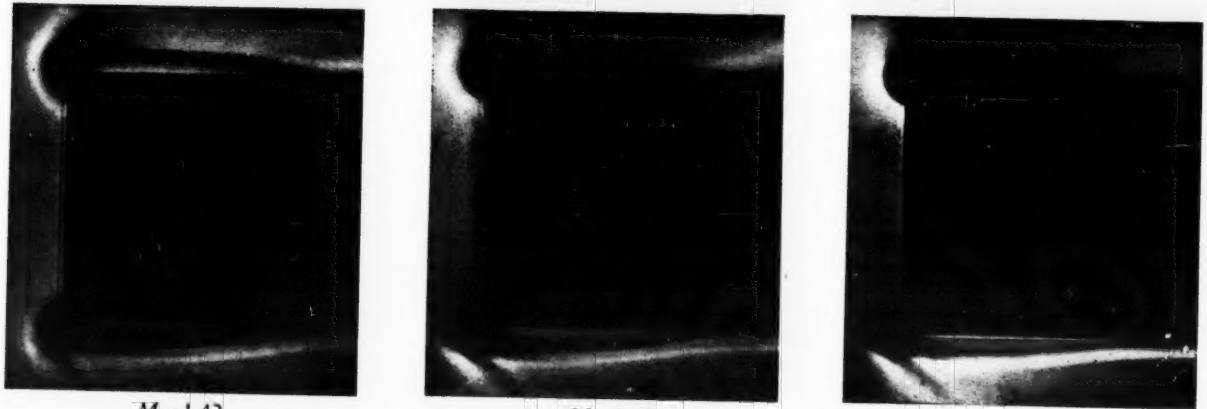

$M = 1{\cdot}42$ $M = 1{\cdot}60$ $M = 1{\cdot}79$

Fig. 8.
Schlieren photographs of the front of the square-nosed two-dimensional plate.

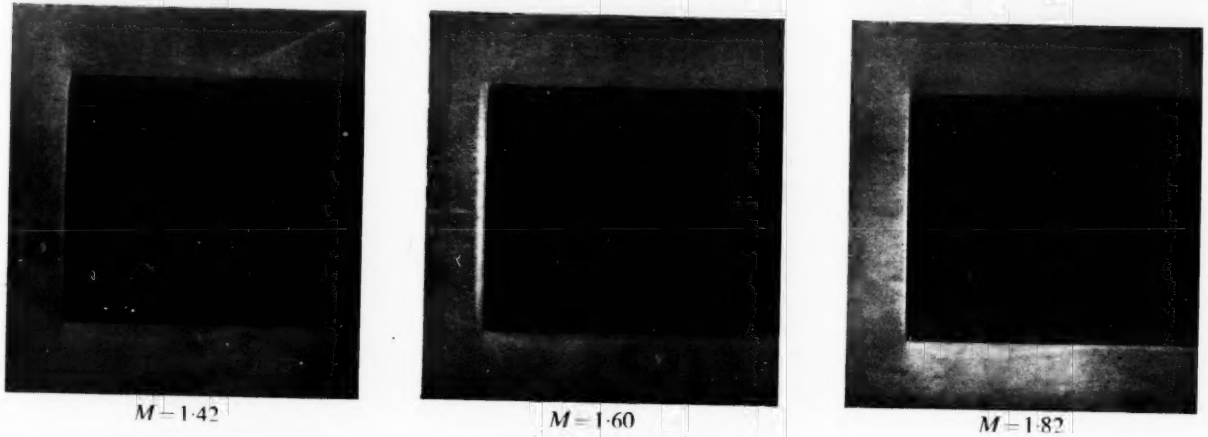

$M = 1{\cdot}42$ $M = 1{\cdot}60$ $M = 1{\cdot}82$

Fig. 15.
Schlieren photographs of the front of the square-nosed body of revolution.

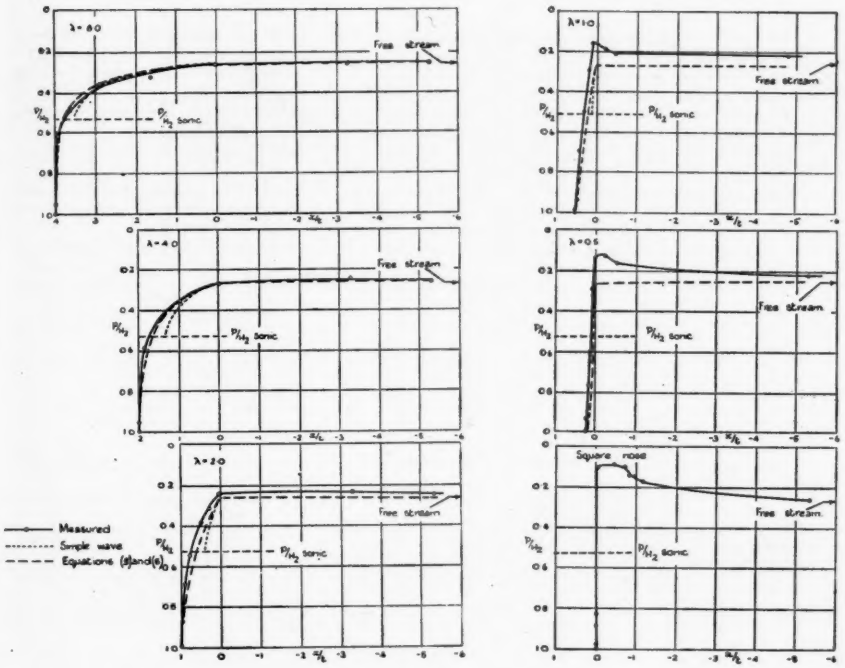

Fig. 4.
Pressures on the two-dimensional cylinders at $M = 1{\cdot}60$.

The pressure falls from a value at the nose which is closely equal to the theoretical total head behind a normal shock wave (*i.e.* $p/H_2 = 1{\cdot}0$), to a value approaching the free stream static pressure far back on the plate. In Fig. 6 the results for the semi-circular nose ($\lambda = 1{\cdot}0$) are compared with Ferri's measurements[5] on a circular cylinder at $M = 1{\cdot}85$ and $2{\cdot}13$. The agreement* is quite good, and this (together with the agreement of the results of the present measurements at $M = 1{\cdot}42$, $1{\cdot}60$ and $1{\cdot}79$) suggests that for this axis ratio the distribution of p/H_2 is insensitive to changes of free stream Mach number.

For the slender nose shapes the fall of pressure along the surface takes place monotonically, but for the blunter noses a pressure minimum occurs near the shoulder. This minimum value of p/H_2 is insensitive to changes of free stream Mach number over the range covered. For this reason the recompression which occurs behind the shoulder becomes more pronounced as the Mach number is reduced because the free stream static pressure (which must be reached far down

*In Ferri's measurements the theoretical total head behind a normal shock wave was not reached at the nose. The agreement is improved if the measured pressure at the nose is used instead of the theoretical pressure in determining p/H_2.

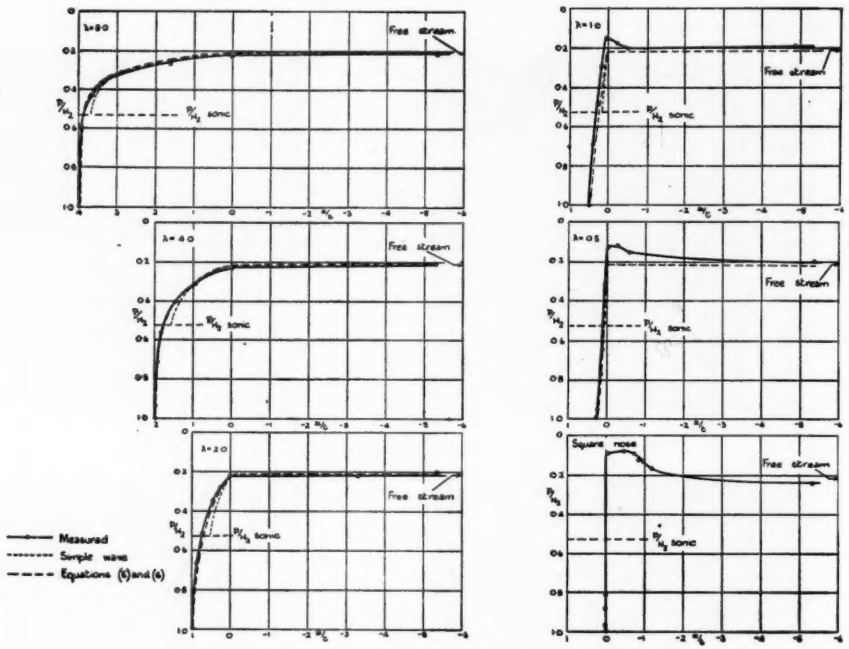

Fig. 5.
Pressures on the two-dimensional cylinders at $M = 1{\cdot}79$.

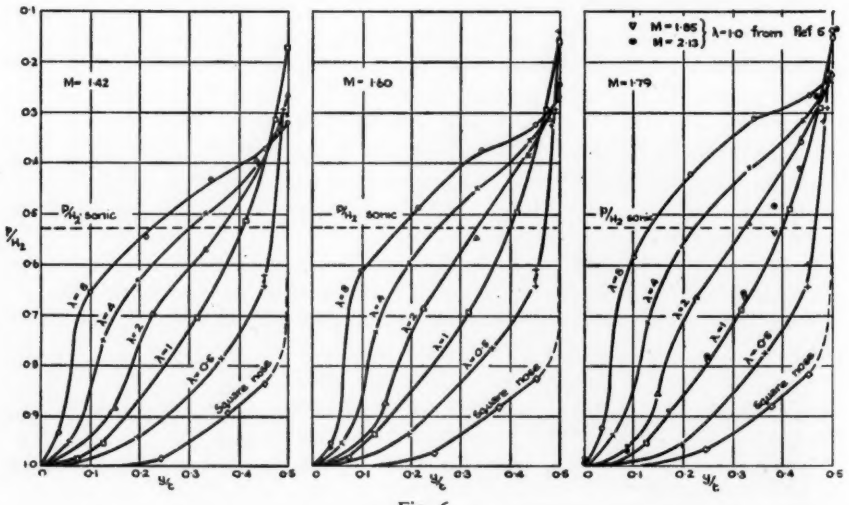

Fig. 6.
Variation of pressure across the noses of the two-dimensional cylinders.

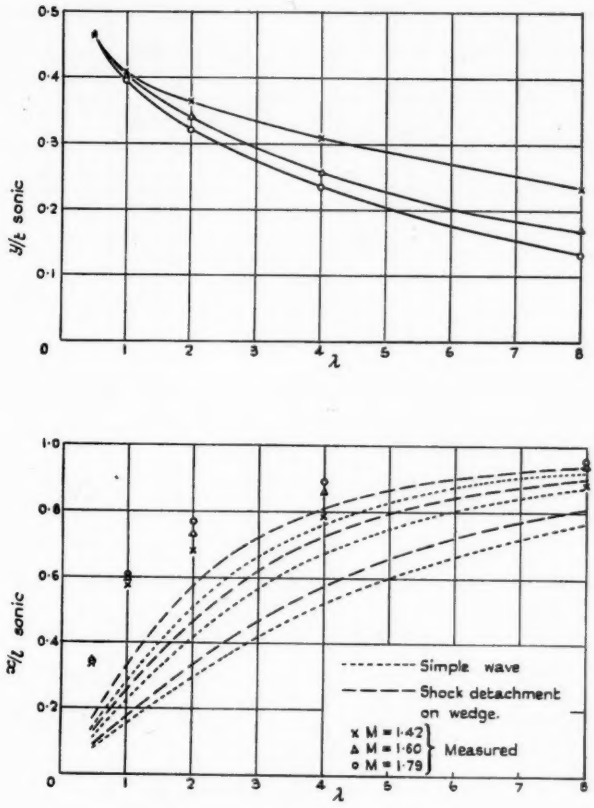

Fig. 9.
Positions of the sonic points on the two-dimensional cylinders.

stream) is raised. The expansion† leading to the fall of pressure is visible in the schlieren photographs reproduced in Fig. 7 (p. 322) as a region of low illumination above, and high illumination below the plate. In cases where a pressure minimum occurs, these photographs also show the region of compression (distinguished by changes of illumination of opposite sign to those in the expansion), or the shock wave, which follows the expansion.

For some of the cylinders there is evidence that the occurrence of the pressure minimum is associated with a local separation and reattachment of the flow behind the shoulder. This is shown for the square-nosed plate in the schlieren photographs reproduced in Fig. 8 (p. 324). The small shock wave visible near the front of the separated region is thought to arise from the condensation of moisture in the rapid expansion round the shoulder. An expansion takes place round the "bubble" of

†The expansion is preceded by a region of compression close to the stagnation point at the nose.

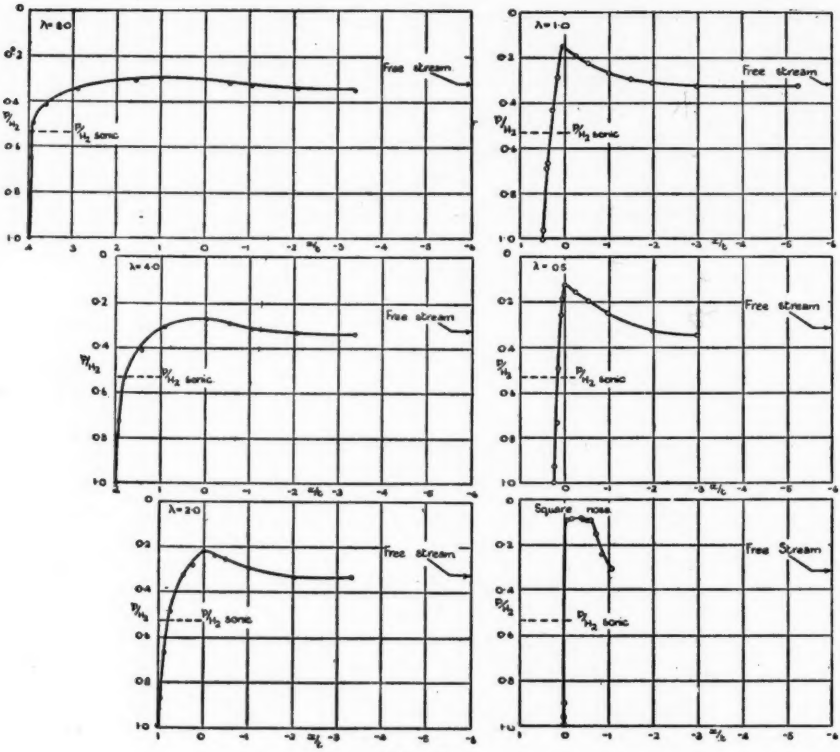

Fig. 10.
Pressures on the bodies of revolution at $M = 1{\cdot}42$.

separated flow, and a compression occurs at the rear where the flow re-adheres and becomes parallel to the surface. The extent and shape of the bubble appears from Fig. 8 (p. 324) to be insensitive to changes of free stream Mach number within the range covered. Experiments in which a layer of oil was placed on the surface revealed a small amount of reversed flow in the bubble. Attempts were made to produce turbulent flow in the boundary layer ahead of the shoulder by fixing an 0·003 in. diameter wire to the front of the plate 0·05 in. below the shoulder, but no detectable changes of flow pattern or pressure distribution were produced.

The positions of the sonic point on the surfaces of the cylinders have been estimated from the experimental results shown in Figs. 3, 4 and 5, and are plotted in Fig. 9 against the axis ratio λ. The sonic point moves back towards the shoulder as the axis ratio is reduced.

It has sometimes been argued[6] that the sonic point for a body with a shoulder formed between two plane surfaces (such as the square-nosed plate) occurs at the shoulder, and that the sonic line is perpendicular to the streamlines. On this basis

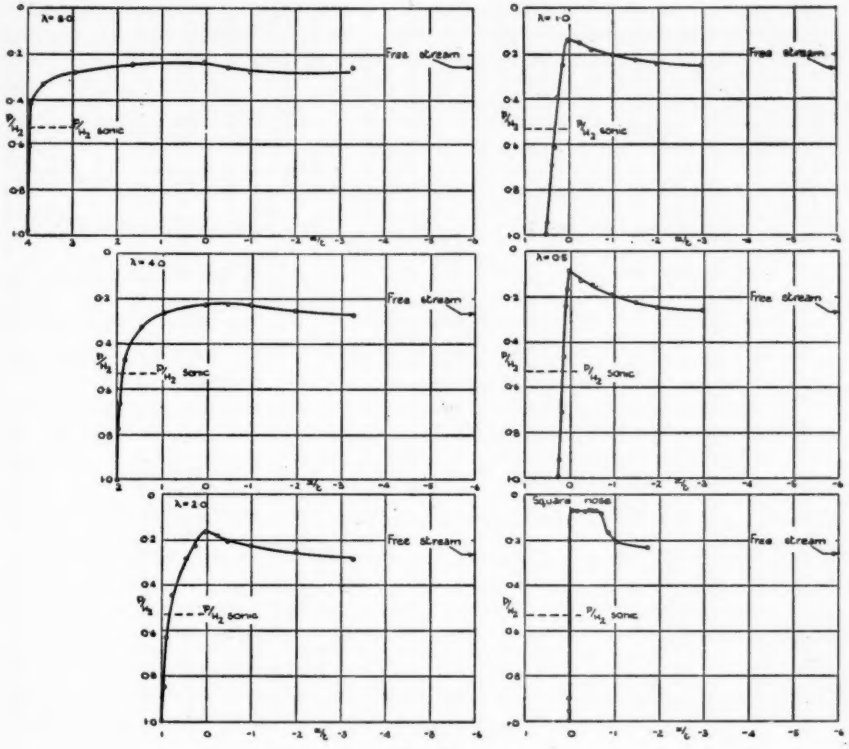

Fig. 11.

Pressures on the bodies of revolution at $M = 1{\cdot}60$.

Liepmann has suggested[7] that the Mach number behind the shoulder should be independent of the free stream conditions, because it corresponds to an expansion from the speed of sound through an angle which depends only on the shape of the body. As already remarked, the present experiments suggest that the minimum value of p/H_2, and hence the maximum Mach number, are in fact roughly independent of the free stream Mach number, and that the strength of the recompression rises as the free stream Mach number is reduced, as would be expected from Liepmann's argument. On this basis the strength of the recompression presumably tends to zero as the free stream Mach number tends to the value reached in an expansion from sonic conditions round the shoulder.

For the square-nosed plate the angle turned through in the expansion round the shoulder would be 90° in the absence of separation, and the values of p/H_2 and M corresponding to a Prandtl-Meyer expansion through this angle are 0·0003 and 6·8 respectively. The effect of separation is to increase the angle slightly. For the flow deflection occurring in Fig. 8 (p. 324), the observed angle of the shock wave

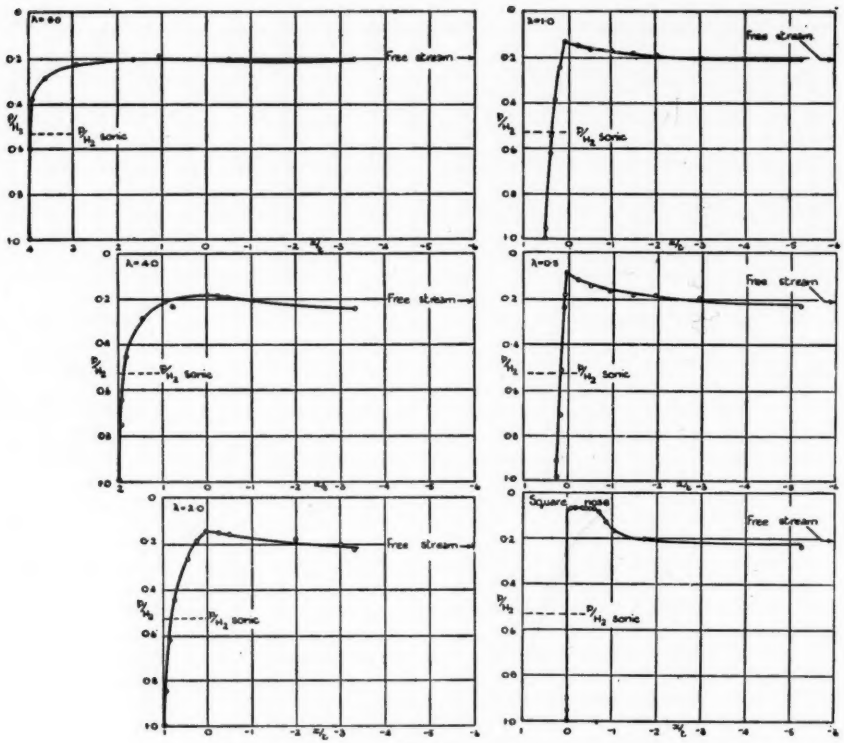

Fig. 12.
Pressures on the bodies of revolution at $M = 1{\cdot}82$.

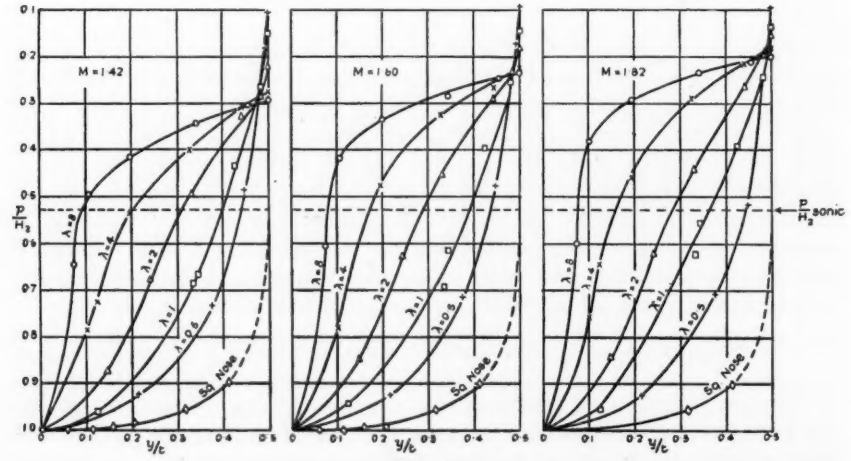

Fig. 13.
Variation of pressure across the noses of the bodies of revolution.

behind the shoulder suggests that the upstream Mach number is much lower than this value. A possible explanation is that the sonic point occurs, in practice, not at the shoulder but a little downstream on the surface of the bubble of separated flow. It seems, therefore, that the main effect of the separation is to make the nose less blunt and to move the effective shoulder back so that the angle turned through in the expansion beyond the sonic point, and the strength of the final shock wave, are reduced.

4.2. *Bodies of revolution*

The pressure distributions on the bodies of revolution are shown in Figs. 10, 11, 12 and 13, and photographs of the flow are reproduced in Figs. 14 (p. 323) and 15 (p. 324). The general nature of the flow appears to be similar to that for the two-dimensional cylinders, but the pressure minimum close to the shoulder seems to be present for a more slender nose shape. The minimum pressures reached with the blunter nose shapes, and the shapes and extent of the bubbles of separation for the square nose, appear to be almost the same as for the corresponding two-dimensional cylinders.

4.3. *Positions of the bow waves*

The shapes and positions of the bow waves have been measured from direct-shadow photographs and are shown in Figs. 17 and 18. The direct-shadow image of a shock wave consists of a dark band on the low-density side followed by a light band. The position of the shock wave corresponds most closely with the front of the dark band in the image. As expected, the bow wave is closer to the nose of a three-dimensional body than a two-dimensional one, and in both cases it recedes from the nose as the axis ratio or the Mach number is lowered.

The distance between the apex of the bow wave and the nose is plotted in Fig. 19 against the radius of curvature* r of the nose expressed non-dimensionally, and in Fig. 20 against the free stream Mach number. As the radius is increased, the bow wave first moves upstream rapidly, but the rate of upstream movement falls, and reduction of the nose radius below that for $\lambda=\frac{1}{2}$ has comparatively little effect. Values obtained by observations on a two-dimensional circular cylinder and on a two-dimensional aerofoil of EC.1250 section are included in Fig. 19, and are in good agreement with values observed in the tests on the plates. The results obtained in other tests[6,8] on spheres and flat-nosed bodies of revolution are included in Fig. 20, and good agreement is obtained with the present results. The agreement of the results for the aerofoil, cylinder and sphere shows that, at least for $\lambda \geqslant 1$, the conditions downstream of the shoulder have little effect on the bow-wave position. This is because the flow behind the shoulder is supersonic.

4.4. *Drag*

The drag coefficients defined in Section 3 have been evaluated by integrating the pressure distributions, and are plotted in Fig. 21 against $1/\lambda$. Curves calculated

*For an ellipse $r/t=1/(2\lambda)$.

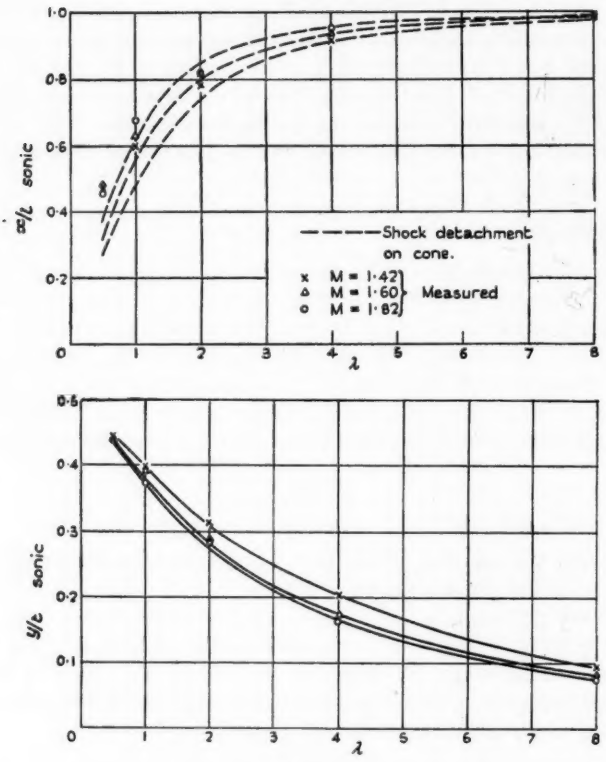

Fig. 16.
Positions of the sonic points on the bodies of revolution.

for wedges and cones are included up to the values of $1/\lambda$ at which theory predicts subsonic flow behind the bow wave. For small values of $1/\lambda$ the drag coefficients of the elliptic-nosed plates are considerably higher than for the wedges, but the additional drag decreases as $1/\lambda$ is raised, and the drags become roughly equal when the value of $1/\lambda$ is reached for subsonic flow behind the bow wave of the wedge. This value is close to that for shock detachment from the wedge. The drag coefficients of the round-nosed bodies of revolution are greater at small values of $1/\lambda$, and less at large values of $1/\lambda$, than the values for cones.

5. Comparison with Theory

In calculating the pressures over the rear of a two-dimensional blunt-nosed aerofoil it is known (*see*, for example, Ref. 9) that it is often sufficiently accurate to assume that the total head just outside the boundary layer is equal to that downstream of a normal shock wave, and that the free stream static pressure is reached at the point where the surface is parallel to the free stream flow. Starting at this

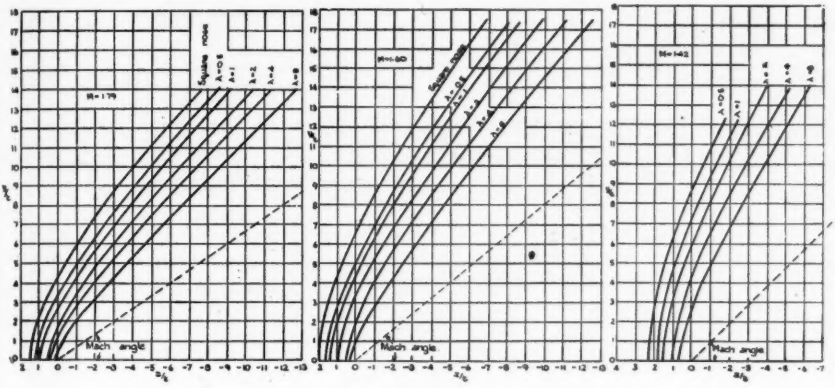

Fig. 17.
Observed bow waves for the two-dimensional cylinders.

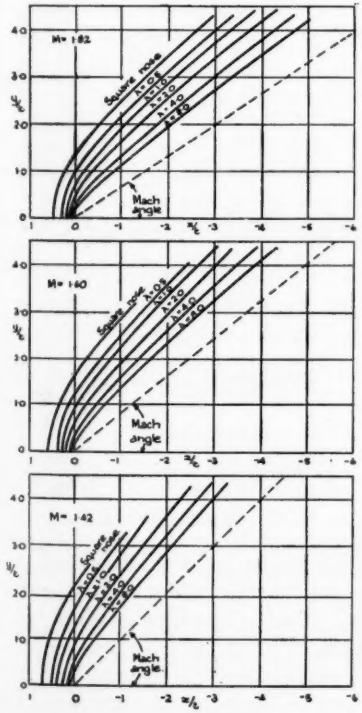

Fig. 18.
Observed bow waves for the bodies of revolution.

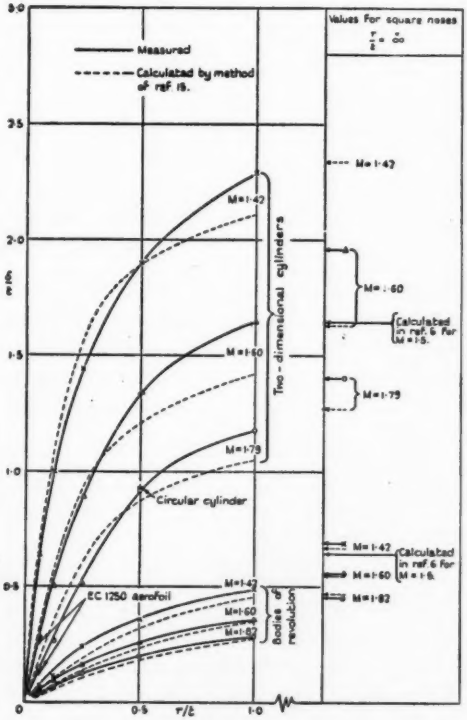
Measured
Calculated by method of ref 15.
Values for square noses
Two-dimensional cylinders
Bodies of revolution
Circular cylinder
EC 1250 aerofoil
Calculated in ref 6 for M = 1·5.
Calculated in ref 6 for M = 1·9.

Fig. 19.
Variation of the position of the bow wave with nose radius.

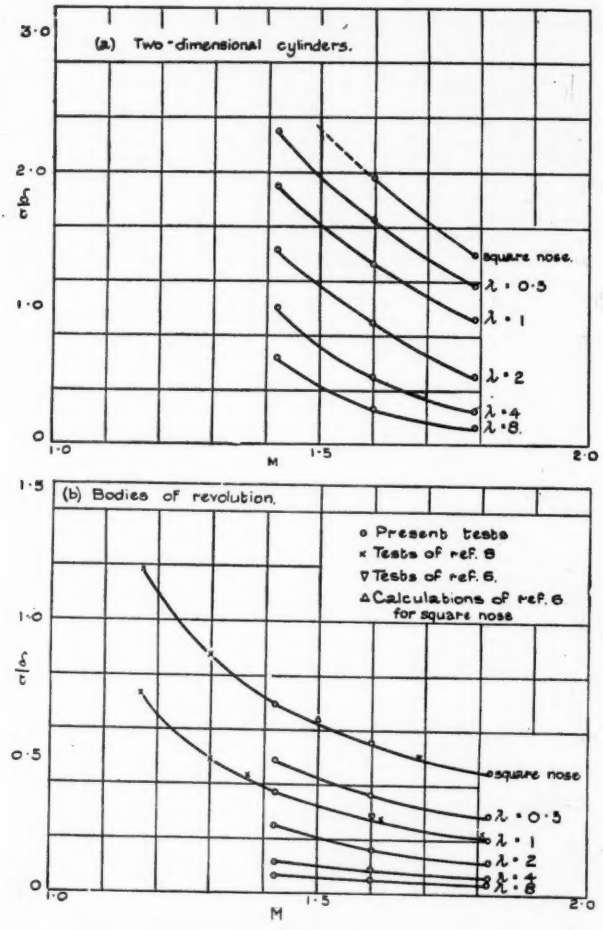

Fig. 20.
Variation of the position of the bow wave with free-stream Mach number.

point, simple-wave theory is used. The agreement between the pressures calculated by this method and those measured usually becomes progressively worse* as the region of subsonic flow at the nose is approached. This is illustrated by Figs. 3, 4 and 5 where the measured pressures are compared with those calculated on the foregoing assumptions. The calculated values are too high in general and, of course, do not show a minimum near the shoulder. The agreement improves as

*Discrepancies may also occur at the tail because of separation or thickening of the boundary layer ahead of the shock wave there (*see*, for example, Refs. 9, 10, 11 and 12).

the Mach number is raised. The calculated positions of the sonic points are compared in Fig. 9 with the measured positions, and are seen to be too far downstream.

On the basis of a suggestion by Hilton[13], Mair has proposed[14] an empirical formula for calculating the pressures on two-dimensional blunt-nosed bodies. Here the surface inclination ϕ in Ackeret's formula

$$C_P = \frac{p - p_0}{\frac{1}{2}\rho U^2} = \frac{\phi}{\sqrt{(M^2 - 1)}} \quad . \quad . \quad . \quad . \quad . \quad (5)$$

is replaced by a false angle ψ given by Mair as

$$\psi = \phi(1 + A_1 \sin\phi + A_2 \sin 2\phi) \quad . \quad . \quad . \quad . \quad (6)$$

where A_1 and A_2 depend on the free stream Mach number. To give better agreement with Ferri's measurements[5] on circular cylinders at $M = 1{\cdot}85$ and $2{\cdot}13$, Mair suggested the use of a third term in the bracket chosen so that the arbitrary condition $\psi = \phi$ when $\phi = \pi/4$ was satisfied. The inclusion of this third term leads to worse agreement with the present measurements at $M = 1{\cdot}42$ and $M = 1{\cdot}60$, and the term has therefore been omitted.

The variation of ψ with ϕ required to give the present experimental results when used in equation (5) is compared in Fig. 22 with the curves given by equation (6). The agreement is seen to improve as the Mach number is raised, and as the value of λ is increased. It appears, however, that a simple empirical formula of this kind which includes no terms in λ is not highly accurate.

The pressure distributions calculated by Mair's method are compared in Figs. 3, 4 and 5 with experiment and are, as expected, in better agreement than values calculated by simple-wave theory. The general tendency is still, however, to predict pressures which are too high, and the calculated drag coefficients plotted in Fig. 21(*a*) are correspondingly high.

An approximate method for calculating the position of the detached bow wave for both two-dimensional and three-dimensional bodies has been described[15] by Moeckel. He assumes that, between the apex and the position of the sonic point on the shock wave, the shock wave is a hyperbola asymptotic to the free stream Mach lines; also that the sonic line is straight and inclined at an angle depending only on the free stream Mach number. Following a suggestion[16] by Busemann, the sonic point on the body is taken as the point where the slope of the surface is equal to the slope for shock detachment on a wedge or cone. The positions of the sonic points calculated in this way are compared in Figs. 9 and 16 with the measured positions. The calculated values are too far downstream, but for the two-dimensional plates they are in better agreement with experiment than values calculated by simple-wave theory. The positions of the shock waves calculated by Moeckel's method are compared in Fig. 19 with the observed positions.

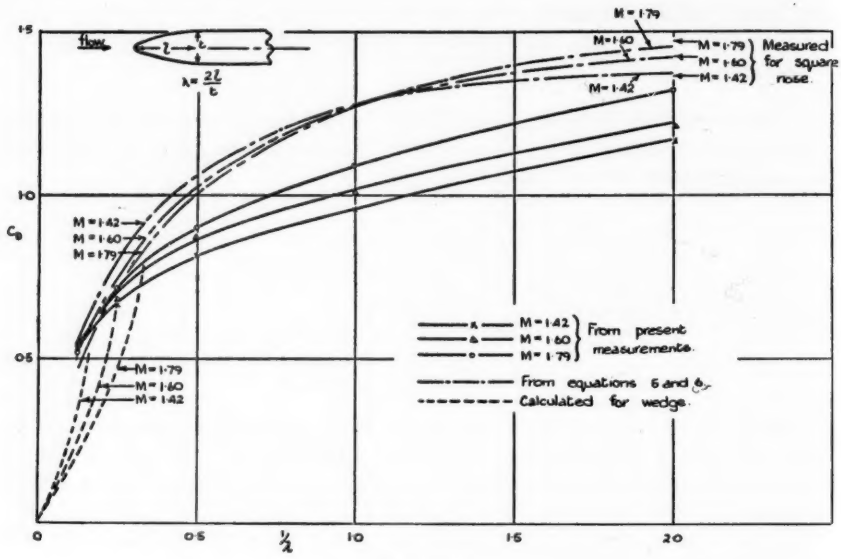

Fig. 21(*a*).
Drag coefficients for the two-dimensional cylinders.

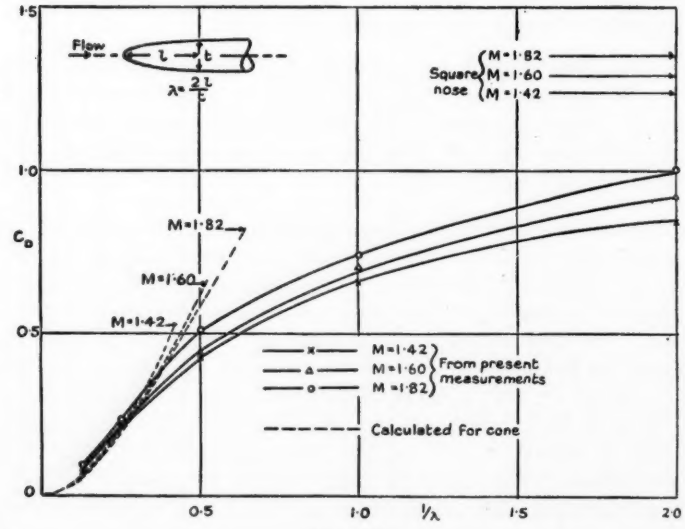

Fig. 21(*b*).
Drag coefficients for the bodies of revolution.

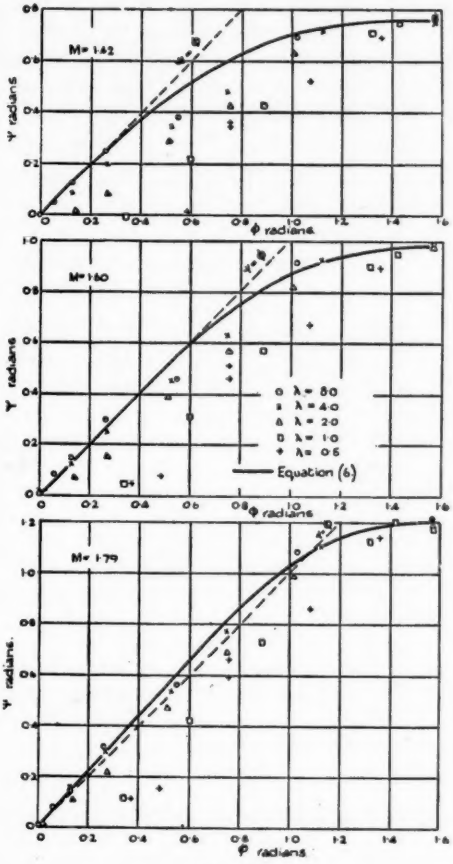

Fig. 22.
Variation of the false angle ψ with the surface angle ϕ for the two-dimensional cylinders.

The most detailed calculations of the flow past bodies with detached bow waves which are known to the authors are those described by Maccoll and Codd[6]. The examples which they considered included a square-nosed plate and a square-nosed body of revolution moving at a Mach number of 1·5. The calculated pressure distributions are shown in Fig. 23 to be in good agreement with experiment. The calculated distance between the apex of the bow wave and the nose of the body of revolution is also in good agreement with experiment (*see* Fig. 20), but there is a considerable discrepancy for the two-dimensional plate. Thus Maccoll and Codd find that the apex of the bow wave is $1{\cdot}65t$ ahead of the nose, whereas the present observations suggest a value of $2{\cdot}3t$.

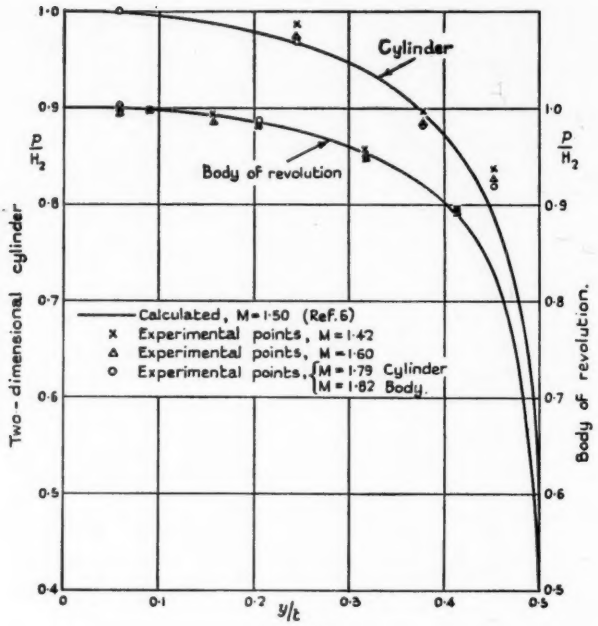

Fig. 23.

Comparison between the measured pressures on the square-nosed cylinder and body of revolution and those calculated in Ref. 6.

6. Conclusions

The main conclusions which may be drawn from the investigation are:—

(*i*) The static pressure p at the surface falls from a value at the front stagnation point which is closely equal to the theoretical total head H_2 behind a normal shock wave to a value downstream of the shoulder which approaches the free stream static pressure. In some cases there is a pressure minimum near the shoulder which becomes more pronounced as the nose is made blunter, and is followed by a compression. Ahead of this compression the distribution of p/H_2 for the blunter nose shapes is insensitive to changes of free stream Mach number over the range covered (1·42 to 1·82). When the nose is square, the pressure minimum and the subsequent compression are associated with a local separation and reattachment of the flow. A local separation may also be present for some of the other nose shapes.

(*ii*) The sonic point on the surface moves towards the nose as the Mach number is raised, and towards the shoulder as the nose is made blunter. For the square-nosed plate and body there is some (but not conclusive) evidence that the sonic point occurs on the bubble of separated flow a little behind the shoulder.

(*iii*) The drag coefficients of the slender two-dimensional elliptic noses are considerably higher than those calculated for wedges of the same axis ratio with attached shock waves, but the drags of the ellipses and wedges become almost equal when the axis ratio becomes equal to the value for subsonic flow behind the bow wave of the wedge. The drag coefficients of the elliptic-nosed bodies of revolution are lower for most axis ratios than those for cones of the same axis ratio.

(*iv*) For the square nose shape, the pressure distributions calculated by Maccoll and Codd for both two- and three-dimensional bodies, and the position of the apex of the bow wave ahead of the three-dimensional body are in good agreement with the measurements. There is a discrepancy between the measured and calculated positions of the bow wave ahead of the two-dimensional body.

(*v*) The pressure distributions calculated by an empirical method suggested by Mair are for slender nose shapes in reasonably good agreement with the measurements on the two-dimensional plates. It is probable that the agreement for specific families of nose shapes could be improved by modifying Mair's formulae, and that the method could be extended to deal with bodies of revolution.

ACKNOWLEDGMENT

The work described formed part of the research programme of the Aerodynamics Division of the National Physical Laboratory, and this paper is published by permission of the Director.

REFERENCES

1. HOLDER, D. W. and NORTH, R. J. (1949). The 9 in. × 3 in. N.P.L. Induced-Flow High-speed Wind Tunnel. R. & M. 2781, 1949.

2. HOLDER, D. W., NORTH, R. J. and CHINNECK, A. (1950). Experiments with Static Tubes in a Supersonic Airstream. R. & M. 2782, 1950.

3. NORTH, R. J. and HOLDER, D. W. (1949). A Spark Light Source for Schlieren and Direct-shadow Photography. Unpublished N.P.L. Report, 1949.

4. HOLDER, D. W. and NORTH, R. J. (1950). The Toepler-Schlieren Apparatus. R. & M. 2780, 1950.

5. FERRI, A. (1942). Influenza del Numero di Reynolds ai Grandi Numeri di Mach. Atti di Guidonia 67, 68 and 69, 1942. *See also* The Influence of the Reynolds Number at Large Mach numbers. A. Eula (*L'Aerotecnica*, Vol. XX, No. 1, Jan. 1940, pp. 20-29). Translated by M. Flint. Air Ministry Translation No. 1015. A.R.C. 4469, F.M. 449.

6. MACCOLL, J. W. and CODD, J. (1945). Theoretical Investigations of the Flow around various Bodies in the Sonic Region of Velocities. A.R.C. 9315, 1945.

7. LIEPMANN, H. W. and BRYSON, A. E. (1950). Transonic Flow Past Wedge Sections. *Journal of the Aeronautical Sciences*, December 1950.

8. HEBERLE, J. W., WOOD, G. P. and GOODERUM, P. B. (1950). Data on Shape and Location of Detached Shock Waves on Cones and Spheres. N.A.C.A. T.N. 2000, 1950.

9. HOLDER, D. W., CHINNECK, A. and NORTH, R. J. (1950). Pressure Measurements in a Supersonic Tunnel on a Two-dimensional Aerofoil of R.A.E. 104 Section. A.R.C. Current Paper No. 62, 1950.

10. HOLDER, D. W. and NORTH, R. J. (1950). Observations of the Interaction Between the Shock Waves and Boundary Layers at the Trailing Edges of Aerofoils in Supersonic Flow. A.R.C. Current Paper No. 53, 1950.

11. BEASTALL, D. and PALLANT, R. J. (1950). Wind Tunnel Tests on Two-dimensional Supersonic Aerofoils at $M=1{\cdot}86$ and $M=2{\cdot}48$. R. & M. 2800, 1950.

12. HOLDER, D. W., CHINNECK, A. and HURLEY, D. G. (1950). Observations of the Supersonic Flow Round a 6 per cent. thick Double Wedge. A.R.C. Current Paper No. 63, 1950.

13. HILTON, W. F. (1946). Force Coefficients on Round Nosed Aerofoils at Supersonic Speeds. A.R.C. 9756, 1946.

14. MAIR, W. A. (1947). A Note on Hilton's Empirical Method of Calculating Pressure Distributions on Round Nosed Aerofoils at Supersonic Speeds. A.R.C. 10,719, 1947.

15. MOECKEL, W. E. (1949). Approximate Method for Predicting Form and Location of Detached Shock Waves ahead of Plane or Axially Symmetric Bodies. N.A.C.A. T.N. 1921, 1949.

16. BUSEMANN, A. (1949). A Review of Analytical Methods for the Treatment of Flows with Detached Shocks. N.A.C.A. T.N. 1858, 1949.

The Influence of the Exit Velocity Profile on the Noise of a Jet*

ALAN POWELL

(*Department of Aeronautical Engineering, University of Southampton*)

Summary: The noise levels of a jet issuing from a long pipe are compared with those of a jet having a square velocity profile at the exit. A subsonic noise reduction of between 2½ and 5 decibels for various conditions is found for the case of the flow emerging with an approximately "turbulent pipe-flow" velocity profile for the same maximum jet velocity, but this is at the expense of a loss in thrust of a quarter. On comparison with a jet of smaller diameter which has an equal thrust for the same maximum jet velocity, it is found that the changes in noise level are rather smaller. For jets of equal diameters, the effects on the subsonic aerodynamic noise generated of a reduction of velocity gradient near the boundary are more than offset by the increased velocities necessary near the centre of the jet to obtain equal thrust. It is concluded that if the effect of differences in initial turbulence can be neglected the use of an auxiliary flow forming a comparatively thin sheath of slower moving fluid at the exit is not likely to result in *large* decreases in the subsonic noise level, and that a general reduction in jet velocity is more effective.

Above the critical pressure larger reductions of up to 10 decibels are found. These are consistent with a delay of the onset of the self-maintained shock-produced noise.

1. Introduction

Professor Lighthill has evolved a general theory concerning the generation of aerodynamic noise due to turbulent mixing[1], and he has shown how the instantaneous intensity of the radiated sound depends on the product, after certain simplifying approximations, in tensor notation†,

$$\frac{\partial^2}{\partial x_i \partial x_j} \rho_0 v_i v_j,$$

where ρ_0 is the mean density of the fluid and v_i and v_j are the total velocities in the i and j directions. If the mean value of one of the factors is large it will result in larger fluctuations of the product than if both fluctuated about a mean which was small. Now in jet flow (if $(\ )_1$ indicates the jet direction and $(\ )_2$ the direction out of the flow) the term $\partial v_1/\partial x_2$ has a large mean, $\partial \bar{v}_1/\partial x_2$, representing the mean shear of the jet, so that $2\rho_0 (\partial \bar{v}_1/\partial x_2)(\partial v_2/\partial x_1)$ is comparatively large. This is the basis for suggesting that turbulent velocity fluctuations, of the type $\partial v_2/\partial x_1$ across the velocity gradient $\partial \bar{\ }_1/\partial x_2$ may play a dominating part in the noise production of a turbulent jet.

*Based on a former paper "An Examination of the Influence of the Exit Velocity Profile of a Two-inch Diameter Jet," A.R.C. 15,473, July 1952, revised and extended.

†Repeated suffixes are to be summed 1 to 3.

Received May 1953. Communicated by Professor E. J. Richards.

Now the greatest mean shear in a jet occurs at the free boundary layer at the exit, where it has a very high value; the turbulent fluctuations probably reach their peak some few diameters downstream. Hence it does not seem unreasonable to infer that an appreciable fraction of the total noise energy of such a jet may emanate from a region fairly close to the exit where both the velocity gradients and the turbulence are comparatively high: the reduction of the velocity gradient at the exit, by introducing a velocity distribution more closely resembling that occurring in jet flow proper (and consequently eliminating some of the turbulent mixing as well) would therefore be expected to result in a lower noise output, particularly of the higher frequencies emanating from close to the exit.

In the case of a choked jet, *i.e.* one in which the pressure ratio exceeds that appropriate to sonic exit velocity, a certain type of self-maintained motion may set in and this may give rise to noise levels many times greater than that due to the turbulent mixing. This motion is caused by the sound pressure radiating from eddy-shockwave interaction creating embryo disturbances at the orifice[2, 3]. Being a resonance effect, its magnitude is susceptible to a weakening of any of the linkages in the cycle. The instability of disturbances in a free boundary layer becomes increasingly small as the thickness of the layer increases (*see* for example Ref. 4 where the laminar jet is discussed) and since the growth of the embryo disturbances provides the energy input to the self-maintained motion it is easily seen that the reduction of the velocity gradients at the exit may produce an appreciable reduction in amplitude. Moreover, since the jet will have an appreciable subsonic sheath it is plausible that the shock waves too will be weakened, resulting in a decreased sound production.

Thus the modification of the velocity profile may be expected to result in a decrease in the noise energy radiated by a jet, both when the noise is due to turbulence mixing alone and also when it is accompanied by emission characteristic to the choked jet. It is the purpose of this paper to investigate the magnitude of these reductions and to find whether it might be a worthwhile means of jet noise reduction (on the hypothesis that a suitable scheme could be evolved) in view of the increasing severity of the problem[5].

There are several methods of obtaining a modified exit velocity profile, and various schemes were considered. The main question which arises is whether the main flow should be surrounded by a sheath of slower moving fluid from another energy level, and if so whether it should be an induced or forced flow. An induced auxiliary flow was not thought to be very conducive to large noise reductions, since it is the early turbulent mixing which would induce the secondary flow, and this is the very origin of the sound which it is wished to reduce*, the only difference from an ordinary jet being the existence of a rigid boundary over part of the length of the turbulent mixing. Thus it was felt that a forced auxiliary flow would be much preferable, provided that the auxiliary flow was itself silenced up to the exit. However, such a scheme is by its very nature complicated structurally and it was felt desirable

*This conclusion is borne out in work done later, *see* Ref. 6.

to obtain some indications of the magnitude of the changes of noise level likely to be realised before proceeding with a forced auxiliary flow rig.

It is for this reason that noise measurements have been made on the flow from a long pipe, since the onset of "pipe flow" will at least partially achieve the desired changes of velocity profile.

Notation

ρ_0	mean air density
x_i, x_j	orthogonal co-ordinates in i and j directions
v	velocity (ft./sec.)
R	pressure ratio
p_j'	measured dynamic head of jet (lb./in.^{2})
p_a	atmospheric pressure (lb./in.^{2})
p_0	stagnation pressure of jet (lb./in.^{2})
P_0	total pressure (lb./in.^{2})
p_s	static pressure (lb./in.^{2})
M	Mach number
C_p	specific heat at constant pressure
γ	ratio of specific heats
T	temperature
P	thrust
db.	decibel, the value of 10 $\log_{10}(E/E_0)$
E	sound level
E_0	reference sound level, corresponding to sound pressure of 0·0002 dynes/cm.^{2}
r_0	radius of jet exit

2. Experimental Apparatus

2.1. The test rig

A Lancashire boiler having a storage volume of 1,200 cubic feet was used as the air reservoir, being charged to a pressure of 150 lb./in.^{2} by a 40 h.p. electrically driven compressor. No air-drying plant was used: some degree of drying was achieved by draining the reservoir when at maximum pressure.

A six-inch diameter main connected the air supply to the laboratory in which the experiment was performed, the control valves being situated in the main in such a way that they could be operated from a convenient point within the laboratory.

A pressure reduction valve immediately followed by a manually operated full-way gate valve was used to control the air flow. These valves were situated some

25 feet from the jet nozzle, so that the intermediate length of piping would act to some extent as a settling chamber. Two silencers, each six feet long, were inserted in this region so as to eliminate so far as possible any noise which may arise from the valve gear. The silencers had a perforated steel core, the annular space between this and the airtight outer shell being packed with sound absorbant material.

The light alloy nozzle body had a designed contraction[7] from the six-inch diameter main to the two-inch exit so as to reduce the possibilities of breakaway of the flow. The exit edge, which was right angled, was clean and as sharp as is consistent with good workshop practice. The nozzle body was mounted on the stub end of the last silencer, which carried a pressure tapping connected to a seven foot mercury manometer. It also carried a thermocouple which was insulated thermally and electrically from the steel stub end. It was found that the air temperature before the contraction (*i.e.* the stagnation temperature, very nearly) varied by only a small amount from the ambient temperature.

A pipe 28 diameters long was attached to this two-inch diameter nozzle for the experiments with a modified velocity profile. The pipe, of 18 S.W.G. copper, had been specially selected for the purpose. It was carefully checked for departure from a truly circular section, it being found that the maximum ovalities* were 0·7 per cent. and 0·4 per cent. at the ends, the end having the larger value being adapted for attachment to the existing nozzle body by a short hand-finished transition piece. At no time has there been any suggestion of the pipe giving rise to any form of resonance, the jet noise produced being indistinguishable in quality from that of the jet issuing from the nozzle alone. Alternatively, a short contraction could be fitted to the nozzle body so as to reduce the exit diameter without introducing a *vena contracta.*

A traverse mechanism was constructed so that pitot and static pressure traverses could be made across the jet at the exit, and was supported from the nozzle body by a yoke, the streamlined traversing part being at a distance of eight times its diameter from the nozzle exit; its interference with the exit velocities could therefore be safely ignored.

The heads of the pitot and static tubes were made from 0·041 in. outside diameter hypodermic tubing, the static pressure holes being 0·009 in. diameter and at 10 tube diameters from the shaped tip. In order to prevent lateral vibrations of the measuring heads, the tubing was backed up by heavier gauge brass tubing (0·125 in. outside diameter) to a point about an inch from the pressure transmission holes. These brass tubes had screwed ends to provide interchangeability with the body of the traversing part.

2.2. *The noise recording apparatus*

Noise measurements were made with a Standard Telephones and Cables Objective Noise Meter Type 74100 A, in conjunction with a Bruël-Kjaer High-speed Level Recorder.

*$(d_{max} - d_{min})/d_{mean}$.

The microphone, an integral part of the equipment, is of the moving coil type, its response being moderately flat over most of the working range between roughly 30 and 10,000 c.p.s., at which frequencies the response begins to fall very steeply.

The output of the S.T.C. amplifier was fed into the level recorder instead of the meter normally used. If desired two overlapping sets of eight octave filters could be used at an intermediate stage to enable spectral analyses to be made. The recorder enabled many more noise measurements to be taken during the limited duration of a test, and it was particularly valuable to have a permanent mechanically produced record, this obviating to a large extent the difficulties of estimating a mean value from a meter whose pointer is fluctuating irregularly, sometimes violently.

The level recorder works as an electromagnetic servo mechanism. The input is led into a potentiometer with a sliding contact, the output from the amplified and rectified signal being used to move the slide, which carries the potentiometer contact and recording stylus, to a position giving a certain datum voltage input to the amplifier. Unfortunately, owing to the nature of the averaging process of the recorder, the instrument does not measure root mean square values. A series of calibration tests was performed to establish suitable corrections, and the effective overall response of the apparatus is as given in Table I.

TABLE I

Filter band c.p.s.	37·5 75	50 100	75 150	100 200	150 300	200 400	300 600	400 800
Effective response: db.	−6·5	−5·0	−4·0	−3·0	−1·00	−0·5	0	0
Filter band c.p.s.	600 1,200	800 1,600	1,200 2,400	1,600 3,200	2,400 4,800	3,200 6,400	4,800 9,600	6,400 12,800
Effective response: db.	−0·5	−1·5	−3·5	−4·0	−5·0	−4·0	−5·0	−6·0

A transformer-coupled oscillator provided a calibration and linkage signal for the noise meter amplifier and the level recorder, a function diagram of the apparatus being shown in Fig. 1. *All noise levels quoted are in decibels relative to a sound pressure of 0·0002 dynes/cm.²*, whether octave energy or total energy.* This unit is used in acoustical measurements because of the very large range of powers encountered—the human ear will tolerate an intensity of about 10^{12} times the lowest audible intensity. It is a logarithmic ratio defined as

$$10 \times \log_{10} E/E_0$$

where E is the sound energy under consideration and E_0 is the datum energy, often expressed in terms of the equivalent r.m.s. sound pressure. Thus if a noise level

*This is approximately the threshold of hearing, and is about 0·2 db. less than 10^{-16} watts/cm.²

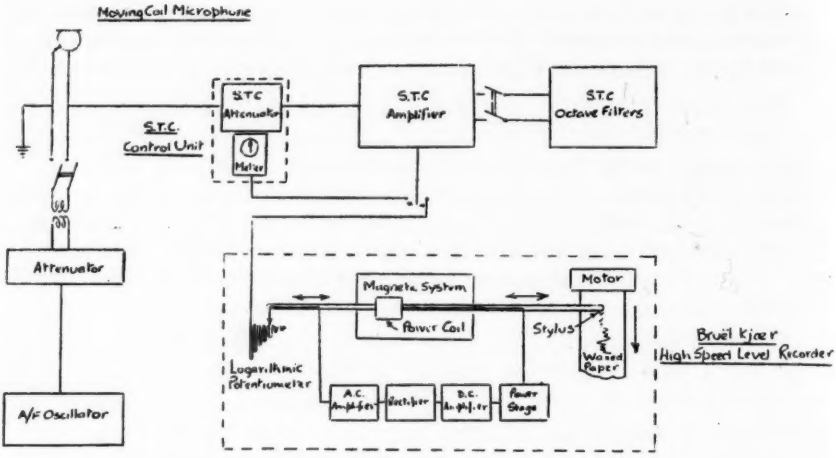

Fig. 1.
Functional diagram of noise recording apparatus.

is doubled, its intensity increases by 3 decibels, a tenfold increase by 10 decibels, hundredfold by 20 decibels and so on. It should be carefully noted that the *decibel* as conventionally used refers to the physical energy of the sound waves traversing a given area, and should be distinguished from subjective loudness (usually measured in *phons*) depending upon the response characteristics of the ear, which may be simulated in some instruments.

The total of the noise energy at a point may be obtained in two ways. The first is to measure the total microphone output. In this case the signal is subject to the frequency response of the microphone and instrument and therefore gives only an approximate result. A correction can be applied if the shape of the noise spectrum is known; this has been done, ignoring any change in shape between various spectra. Hence measurements of this sort, which we shall denote as "Total" Noise Level, are approximate. The second method is to make frequency analyses of the noise—*i.e.* its variation of intensity with frequency, and to integrate the result. This is the preferable method, but clearly takes longer. Both methods have been used where convenient in the work described here, and both are limited by the microphone response.

2.3. *Accuracy of measurement*

Several sources of almost unavoidable errors arise in making measurements of noise level, a fact not unusual in acoustical work. The initial calibration of the noise meter, which was very kindly performed by the Acoustics Department of the National Physical Laboratory, is probably accurate to within 0·5 db.; the actual reading of the noise level possibly involves a similar uncertainty, and more than this

at the low frequency end of the spectra where the intensity fluctuates irregularly with time. Errors in the octave analysis due to the slope of the spectrum may involve a further decibel, again towards the lower frequencies where the slope is greatest.

Further, owing to the experiments being performed in a confined space, roughly 33 ft. × 22 ft. × 11 ft., certain errors arising from reflected noise will be present, although some sound absorbent material had been introduced. These errors have been considered in some detail and it has been found that the reflected noise level is practically constant at various points within the laboratory. In general the subsonic measurements cannot have an error exceeding +2 db. at the 30° position or +3 db. at the 90° position and in fact are probably appreciably less. Above choking the errors will be of the same order, except if directional minima happen to occur, in which case the reflected noise would mask the minima and a value not far different from the average would be obtained. The position here is further complicated by the possibility of standing waves being established within the room, since the choked jet noise is characterised by possessing a discrete frequency or frequencies.

Thus the error in absolute value of the noise intensity may be of the order of several decibels, although comparative values are probably correct to within a decibel. It will be noticed that some spectra display a zig-zag irregularity: this usually arises from a slight variation in jet pressure during the test. Attention is drawn to this and the effect on the spectrum as a whole is mitigated by passing through the sets of filters in turn. This error does not arise in "Total" measurements since the pressure was slowly and steadily reduced, marking lines being produced on the recording at the appropriate point. Finally it should be noted that the characteristic noise above choking of the jet is underestimated by up to four decibels, since the correction applied over the whole range was appropriate to the subsonic jet-type noise.

2.4. *Measuring stations*

The noise measurements were made at two microphone positions, both four feet from the nozzle exit (*i.e.* at 24 exit diameters for the two-inch jet), and at angles of 30° and 90° to the direction of the jet axis. These positions were chosen as being a suitable compromise between an acceptable error due to reflected sound energy and the desirability to be as far as possible from the noise-generating region of the jet. Later work[6, 12] indicates that the measurements cannot really be considered as distant-field values; the changes in noise level far from the jet will not necessarily correspond exactly to the measured values.

The jet parameter chosen is the excess pressure in the stream immediately before contraction, denoted by p_j' and consequently is very nearly equal to the initial stagnation pressure of the jet. The pressure ratio is then

$$R=(p_j'+p_a)/p_a$$

where p_a is the atmospheric pressure. It is convenient to quote p_j' in lb./in.^{2}

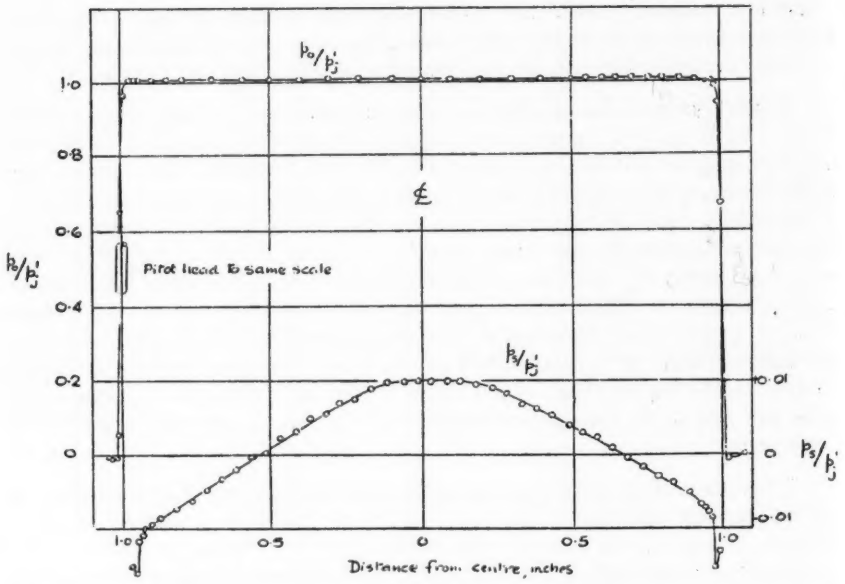

Fig. 2.

Traverses across 2 inch diameter plain jet exit. p_0 is the stagnation pressure and p_s the static pressure. p_j' is the measured initial jet pressure.
Case 1: $p_j' = 5$ lb./in.^{2}, $M = 0{\cdot}66$.

3. On the Exit Velocity Profiles and Thrust

Pitot and static pressure traverses were made in the plane of the exits, using the mechanism described earlier.

The traverses for the designed nozzle are shown in Fig. 2. Here p_0 is the stagnation pressure; since in measuring p_j' the velocity head prior to the contraction has been ignored, p_0/p_j' exceeds unity by about 0·8 per cent. as observed away from the walls. p_s is the static pressure in the jet, measured relative to the ambient atmospheric pressure far from the exit.

The pitot pressure is seen to be very nearly constant across the orifice, the thickness of the boundary layer being less than the pitot tube diameter. The boundary layer is thought to be about 0·020 in. or 0·030 in. in thickness. The slight negative pressures (from which 0·008 should be subtracted) were registered when the pitot head was abutting the outside face of the nozzle, with a clearance of two or three thousandths of an inch.

The static pressure varies from $+1$ per cent. to about -1 per cent. of p_j' from the centre to the wall of the nozzle. Small but steep minima were recorded very close to the wall, the holes of the static tube being placed in the circumferential direction.

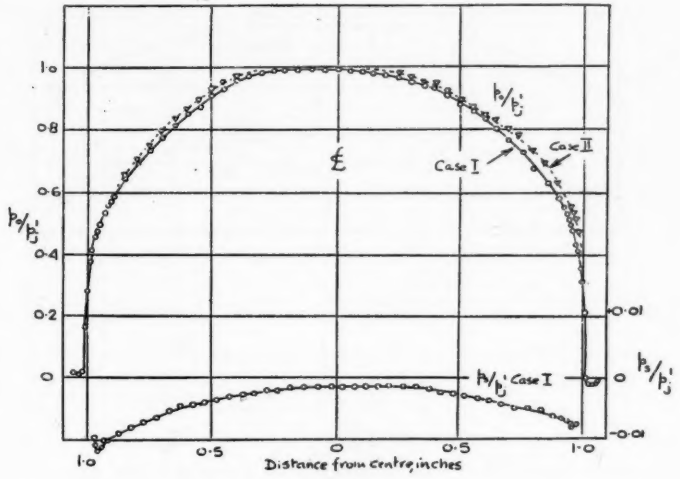

Fig. 3.

Traverses across 2 inch diameter pipe exit. p_0 is the stagnation pressure and p_s the static pressure. p_j' is the measured initial jet pressure.

Case I: $p_j' = 5$ lb./in.^{2}, $M_{max} = 0{\cdot}66$.

Case II: $p_j' = 12$ lb./in.^{2}, $M_{max} = 0{\cdot}96$.

The corresponding traverses across the exit of the pipe are shown in Fig. 3, for two values of the jet pressure:—

Case I: $p_j' = 5$ lb./in.^{2}

Case II: $p_j' = 12$ lb./in.^{2}

The values for the pitot traverse of Case II are not appreciably different from those of Case I, except where indicated.

The pitot pressure is almost constant over a short distance near the centre of the flow, but the ratio p_0/p_j' does not quite reach unity, indicating some loss of total head.

The boundary layers have thickened very considerably, a slight asymmetry across the pipe being present. Although a pressure loss at the centre has occurred, suggesting that pipe flow has been fully established, the fact that there appears to be a region of constant pitot pressure at the centre indicates that the flow is still in a state of transition. Nikuradse's work supports the suggestion that it is unlikely that complete pipe flow has been established, a transition length nearer to 40 diameters being required. However, Latzko's theoretical result indicates 20 diameters, although his result is generally accepted as being an under-estimate (*see*, for example, Ref. 8). The ratio $(\rho v)_{max}/(\rho v)$ is found to be 1·18 and 1·16 for the two cases, suggesting that development towards the usual (incompressible) value of 1·2 or so is still taking place.

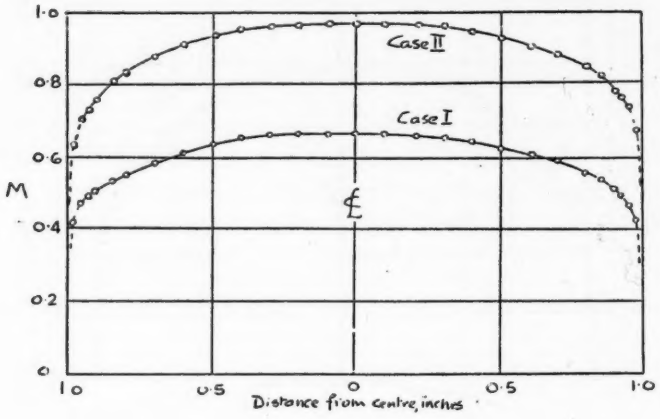

Fig. 4.

Mach number distributions across exit of 2 inch diameter pipe.

The static pressure is slightly below the atmospheric value into which the jet was exhausting, and decreases (negatively) towards the boundaries of the flow. The variation is less than that observed for the flow exhausting from the nozzle.

If certain assumptions are made the variation in axial velocity across the exit can be estimated. Firstly it will be assumed that heat transfer can be neglected. Since the Prandtl number, $\sigma = \mu C_p / k$ is close to unity for a turbulent flow, the use of the normal energy equation is unlikely to lead to appreciable errors.

It will also be assumed that condensation effects are negligible. Although in Case I no condensation effects were apparent, a "core" of condensed water vapour extending along the centre of the pipe was clearly visible at the higher pressure. The difficulties encountered in attempting to estimate a proper correction to allow for the resulting loss in total head (which may account in whole or in part for the observed loss near the centre of the pipe) are very considerable. Apart from the problem of deciding exactly what takes place at the pitot head, *i.e.* whether the droplets pass around the pitot head, or pass into it, or are small enough to evaporate[9], conditions vary in a marked fashion across the exit and the absolute humidity of the air is very uncertain. For these reasons no attempt has been made to allow for condensation effects. It should also be noted that the influence of turbulent velocity fluctuations on total and static heads has similarly been ignored. The general accuracy of the noise measurements does not justify a great deal of labour in estimating various flow parameters, and the resulting approximate estimates are considered sufficiently accurate for the present applications; however, it should be remembered that these simplifying steps have been made.

Since in the total head gradient across the pipe exit the effective centre of the pitot tube will not coincide with the geometric centre, a correction according to

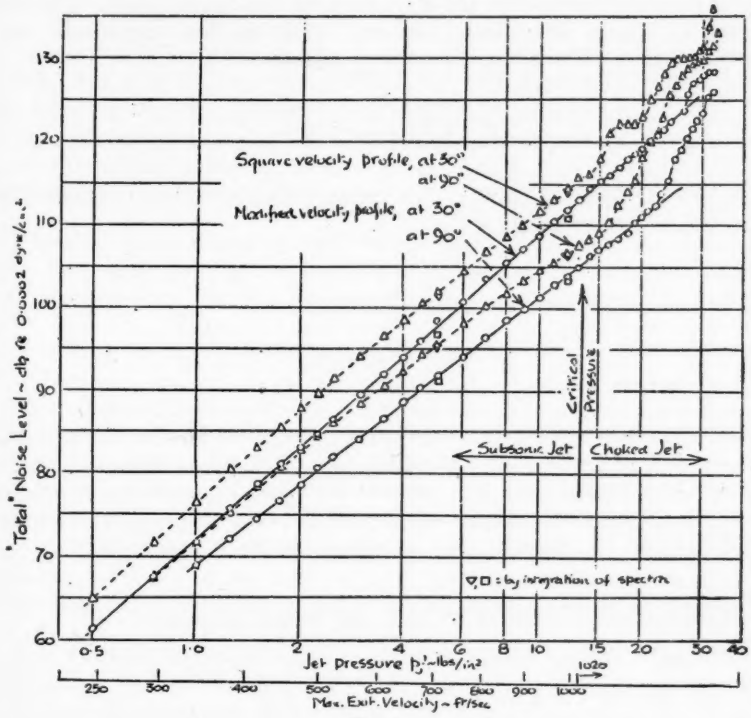
Square velocity profile, at 30°
at 90°
Modified velocity profile, at 30°
at 90°
Critical Pressure
Subsonic Jet
Choked Jet
▽,□ : by integration of spectra
"Total" Noise Level ~ db re 0·0002 dyne/cm²
Jet pressure p_j ~ lbs/in²
Max. Exit Velocity ~ ft/sec

Fig. 5.
Comparative noise levels for 2 inch diameter jet with square and modified exit velocity profiles.

Maas and Young[10] has been applied. Very close to the boundaries, *i.e.* at distances less than the pitot head radius, the observed pressures will diverge considerably from the actual values: a suitable curve has been sketched in over this distance so as to give the correct value of zero velocity at the wall. This does not apply to Figs. 2 or 3 which show experimental points.

Since the compression at the pitot can be considered to be isentropic, the Mach number can be obtained directly from the expression

$$M^2 = \frac{2}{\gamma - 1}\left\{\left(\frac{P_0}{p_s}\right)^{\frac{\gamma-1}{\gamma}} - 1\right\} \quad . \quad . \quad . \quad . \quad . \quad (1)$$

where P_0 is the total pressure and p_s the static pressure. As zero heat transfer has been assumed

$$\tfrac{1}{2}v^2 + C_p T = T_r = T_0 \quad . \quad . \quad . \quad . \quad (2)$$

T_r is the reservoir temperature and T_0 is the total value at the pitot. The former is known to remain very nearly constant. Thus the flow temperature can be found from

$$T=T_r\left(1+\frac{\gamma-1}{2}M^2\right)^{-1} \quad . \quad . \quad . \quad . \quad . \quad (3)$$

and the velocity follows from (2). The corresponding densities are obtained from the gas law, the thrust being

$$P=2\pi\int_{-r_0}^{+r_0}\rho v^2 r\,dr \quad . \quad . \quad . \quad . \quad . \quad (4)$$

where r_0 is the exit radius.

The Mach number distribution is a by-product of the calculation and is shown in Fig. 4. On performing the integrations the reductions in thrust for the "pipe flow" are 26·6 per cent and 25·6 per cent. for Cases I and II respectively. The values appropriate to the square velocity profile were obtained by assuming an effective diameter of 1·98 inches as an allowance for the boundary layer.

4. Influence of Modified Profile on Noise Levels

4.1. "Total" noise levels

4.1.1. SUBSONIC EXIT VELOCITY

The variation in "Total" noise level (*i.e.* as obtained from total microphone output when suitably corrected) as the jet pressure increases, at the two measuring stations for the flow from the nozzle (with the square exit velocity profile) and for the flow from the pipe (with the modified exit velocity profile) is shown in Fig. 5 which is a logarithmic plot of sound energy against jet pressure, *i.e.* decibels plotted against $\log p_j'$.

In the 30° position the subsonic noise levels in decibels are linear with $\log p_j$ for both the square and modified exit velocity profiles, so that the following empirical laws for the "Total" noise level "T" fit to within one decibel.

$$\text{Square velocity profile: } \text{"}T\text{"}=76+36\log_{10}p_j'$$

$$\text{Modified velocity profile: } \text{"}T\text{"}=71{\cdot}5+37{\cdot}5\log_{10}p_j'$$

valid for $0{\cdot}5<p_j'<13{\cdot}2$, $(0{\cdot}2<M<1)$, choking occurring at the higher limit. The decrease in noise level of about 4½ decibels becomes smaller as the velocity increases, being about 2½ decibels at choking. Similar remarks apply to the 90° position where the noise levels are somewhat lower, the smaller slopes indicating a change in the directional properties of the jet as its exit velocity increases so as to increase the downstream emission[1]. The reductions at 90° are also somewhat smaller.

4.1.2. SONIC EXIT VELOCITY—JET CHOKED

Consider first the jet with the square exit profile. At a certain pressure exceeding that at which choking first occurs the noise levels commence to increase much more rapidly, after progressing as a continuation of the subsonic laws. These increases, displaying a stepped appearance, especially at 30°, are characteristic of the self-maintained motion peculiar to choked jets[3], and are audible as harsh "whistling" or "hooting."

The effect of modifying the exit velocity profile is to *delay* the onset of this motion to a higher jet pressure, at which point the increases commence, similarly to the previous case. At 90°, for example, the slopes increase so as to indicate

$$\text{Noise energy} \propto p^{8 \cdot 6}.$$

The fact that this pressure appears different for the two measuring stations may be attributable to the highly directional nature of that form of noise[2, 3] or to a susceptibility of the generation of the motion to external conditions which varied slightly at the tests, or to refraction. This may arise since the initial shock waves forming in the jet will probably be "internal," *i.e.* separated from the edge of the jet by the thick boundary layer. Hence sound generated at the shock may be refracted through it, and this would result in little noise being radiated to the 30° position until the strength and lateral dimensions of the shock had increased.

It is interesting to note that the noise levels above choking, but before the characteristic noise arises, again follow continuations of the subsonic laws to an excess pressure considerably above that at choking. This suggests that the type of noise so measured* (*i.e.* due to turbulent mixing) depends less on the details of the flow close to the orifice, which are of course widely different below and above choking, than on the total momentum of the jet in conjunction with the large scale turbulent mixing further downstream.

Hence the effect above choking is to *delay* the onset of the characteristic choked jet noise. The reduction in "Total" noise level is irregular, reaching a maximum of about 10 decibels.

4.2. Analysis of spectra

The spectra given in Fig. 6 were obtained for the jet pressures of Cases I and II; the maximum velocities are thus the same, as is the jet diameter. The spectra are all of the type associated with subsonic jets, *i.e.* extending over many octaves and having a single flat maximum.

Two changes due to the modified profile are apparent. Firstly, the high frequency part of the spectrum is lowered, as was anticipated. The reduction

*Subjected to the effective response of the instruments (Table I), *see* Ref. 3.

TABLE II

COMPARISON OF TOTAL NOISE LEVELS

(Equal maximum velocities and exit diameters)

Jet Pressure p_j' lb./in.^{2}	V_{max} ft./sec.	M_{max}	*Thrust Change** per cent.	*Angle to jet*	*Total Noise Levels:* db.		
					Velocity Profile		*Change** db.
					Square	*Modified*	
12	990	0·96	−25·6	30°	114	110·5	−3·5
				90°	106	103·5	−2·5
5	708	0·66	−26·6	30°	101·5	96·5	−5·0
				90°	95	91	−4·0

*From square to modified velocity profile.

varies between about 3 and 7 decibels depending on speed and position, and there seems no reason why this should not continue and possibly increase at extended frequencies above the microphone range. Secondly, the energy carried at the low frequencies is also decreased, though by a smaller amount; since this noise arises some distance from the exit[6], where the influence of the exit conditions will have become largely masked by the free turbulence, the reason for this decrease may perhaps be sought in the decreased momentum of the jet.

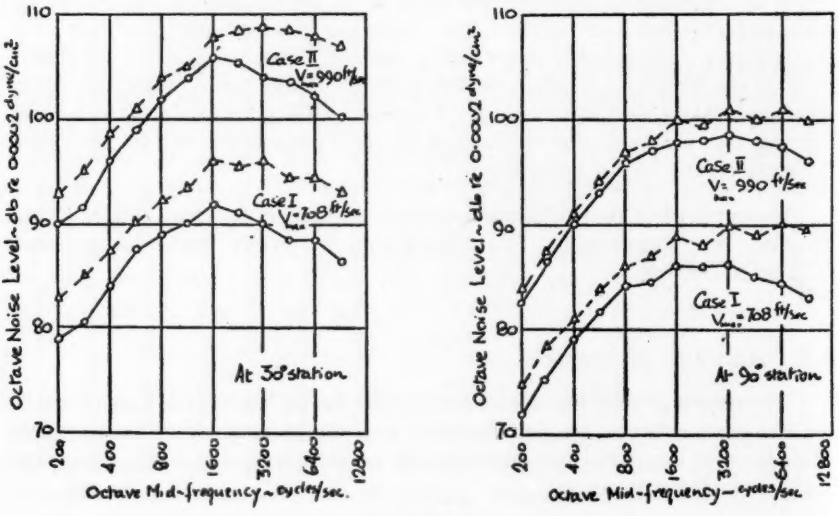

Fig. 6.

Effect of modified velocity profile on spectra of 2 inch diameter jet.
—Δ--Δ--Δ--Δ-- Square exit velocity profile.
—O—O—O—O— Modified exit velocity profile.

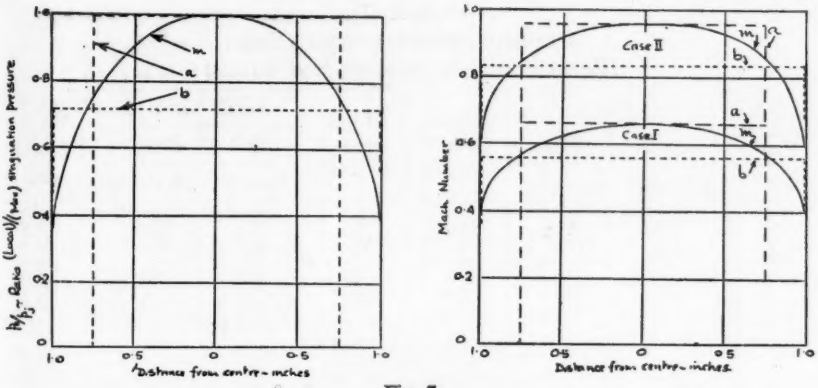

Fig. 7.
Mean distributions of stagnation pressure for equal thrust, and Mach number distributions for the thrust of Cases I and II (2 inch diameter jet).

Integration of the spectra gives a more accurate estimate of the total noise. Owing to the slightly different forms of that part of the spectra neglected, the square profile values, especially at 90°, may be slightly underestimated relative to the others. Hence the changes noted in Table II are slightly conservative as are the total values. The levels obtained by integration of spectra are marked on Fig. 5 for comparison with the values obtained by the other method.

5. Implications

The modification of the exit velocity profile has resulted in decreased noise levels, being associated with a decrease in thrust of a quarter, *i.e.* by approximately one decibel*. Viewed in this way one may say the efficiency of noise generation has been reduced, since the noise levels have decreased by between 2½ and 5 decibels.

But this comparison is not a practical one. No engine designer could be expected even to consider sacrificing so much propulsive efficiency to obtain a relatively modest noise reduction, at least in comparison to the desired reductions.

It is more useful therefore to make comparisons on a basis of equal thrust. This can be done in two ways,

(*a*) Equal maximum velocities, but diameters adjusted to give same thrust.

(*b*) Equal diameters, but maximum velocities adjusted to give same thrust.

The resultant profiles giving the same thrust are shown in Fig. 7.

5.1. Equal maximum velocities, diameters adjusted for equal thrust

Here the central velocity remains unaltered, but is reduced towards the edges of the jet, so that a relatively larger jet with increased mass flow is needed. In

*Equivalent to 26 per cent.

TABLE III

COMPARISON OF TOTAL NOISE LEVELS
(Equal maximum velocities and thrusts)

Jet Pressure p_j' lb./in.²	V_{max} ft./sec.	M_{max}	*Thrust Change** per cent.	*Angle to jet*	*Total Noise Level:* db.		
					Velocity Profile		*Change** db.
					Square†	*Modified*‡	
12	990	0·96	nil	30°	113	110·5	−2·5
				90°	104	103·5	−0·5
5	708	0·66	nil	30°	100	96·5	−3·5
				90°	93	91	−2·0

*From square to modified
†Jet diameter: 1·72 in.
‡Jet diameter: 2·0 in.

practice, this will approximate to ducted fan or by-pass engines where the outer velocity is less than the central.

The shape of the exit velocity profiles as actually used are shown in Fig. 7 (profiles "a" and "m"), Fig. 8 gives the spectra obtained, and the total noise levels are given in Table III with the other relevant details.

A comparison with the first case shows that reducing the plain jet diameter from 2·0 to 1·72 inches to equalise the thrust has resulted in a decrease in noise

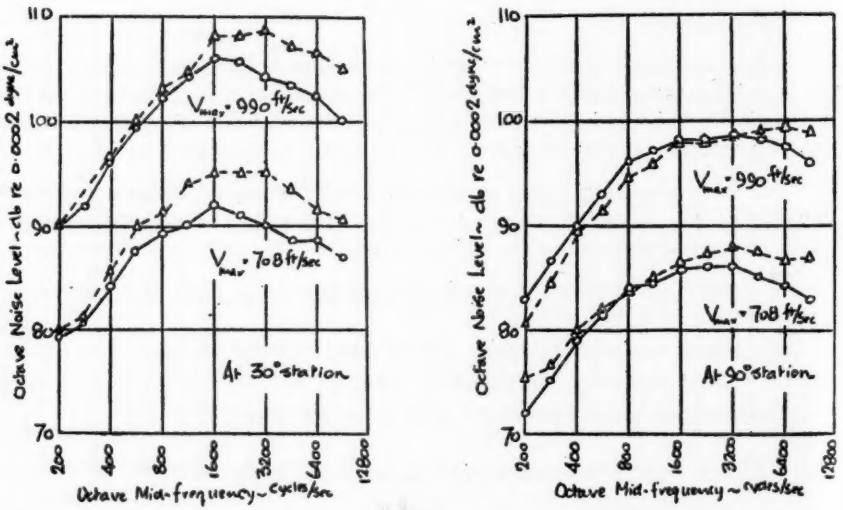

Fig. 8.
Comparison "a" against spectra for plain and modified jets having the same maximum velocity and thrust.
—Δ--Δ--Δ--Δ-- Square exit velocity profile, jet diameter 1·72 inches.
—O—O—O—O— Modified exit velocity profile, jet diameter 2·00 inches.

TABLE IV

COMPARISON OF NOISE LEVELS
(Equal diameters and thrusts)

Jet Pressure p_j' lb./in.²	V_{max} ft./sec.	M_{max}	*Thrust Change**	*Angle to jet*	*Total Noise Levels:* db.		
					Velocity Profile		*Change** db.
					Square	*Modified*	
8·5†, 12‡	875†, 990‡	0·83†, 0·96‡	nil	30° 90°	108·5 102	110·5 103·5	+2·0 +1·5
3·55†, 5‡	610†, 708‡	0·56†, 0·66‡	nil	30° 90°	96 90·5	96·5 91	+0·5 +0·5

*From square to modified velocity profile
†Square velocity profile
‡Modified velocity profile.

level of between 1 and 2 decibels, the shape of the spectra remaining practically unchanged. Consequently the reductions obtained by modifying the velocity profile are less by this amount. While the reductions are not large—between ½ and 3½ decibels—*it can be concluded that reducing the velocity gradient at the boundary of the jet results in less noise for a given thrust.* Hence one would expect the presence of a secondary flow, as in by-pass or ducted fan engines, to result in less jet noise than for the equivalent plain jet.

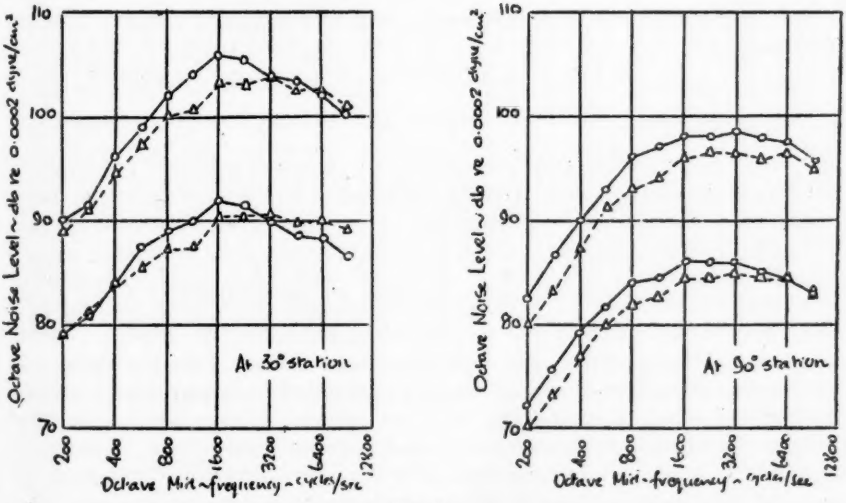

Fig. 9.
Comparison "*b*" against spectra for plain and modified jets having the same diameter (2 inches) and thrust.
—Δ--Δ--Δ--Δ--Δ-- Square exit velocity profile (V_{max}=875 or 610 ft./sec. resp.).
—O—O—O—O— Modified exit velocity profile (V_{max}=990 or 708 ft./sec. resp.).

5.2. *Equal diameters, velocities adjusted to give same thrust*

Here the profiles are "b" and "m" in Fig. 7.

The results are shown in Fig. 9 and Table IV. The position is now reversed. The plain jet is the less noisy, and it appears that the increased velocity near the centre of the modified jet more than offsets the effect of reducing the velocity gradients. Moreover, owing to the reduction of the higher frequencies, the maximum of the spectra is at a lowered frequency, giving the illusion of a larger diameter jet, so that insulation difficulties will be somewhat enhanced and attenuation through the atmosphere will be less.

Hence for given jet thrust and fixed diameter, a constant velocity across the exit is preferable to the modified type.

This is a point of some importance: the reduction of efflux velocity is the more effective method of reducing the noise*. *A decrease of jet velocity of only* 13 *per cent. (i.e.* ½ *decibel) results in noise reductions of between* 2 *and* 4½ *decibels, even when the jet diameter is increased to equalise the thrust.* This is in fair agreement with a dimensional analysis of the simple theoretical quadrupole field[1] which indicates the noise level to vary as $(\text{velocity})^8 \times (\text{diameter})^2$, so that velocity changes have a much greater influence than the corresponding diameter changes. In fact for constant thrust, theoretically and under simplified conditions

$$\text{Noise energy} \propto v^6$$

where v is the exit velocity. Hence a 3 decibel reduction might have been anticipated.

6. Conclusions

Firstly, attention is drawn to the fact that a change of the initial turbulence of the jet occurs simultaneously with the modification of the velocity profile, being inherent in the process of the development of the latter. This turbulence will give rise to some aerodynamic noise *within* the pipe, but there is no evidence to suggest that this is other than very small in comparison with the jet noise. The effect of this initial turbulence on the jet flow, and consequently on its noise production, is much more of an unknown quantity; for while, in view of the growing evidence that a large fraction of the noise is generated some distance from the orifice, one might think the effects to be of secondary importance, certain tests[11] recently performed in America suggest that this is not necessarily so. However, the fact that the stability of the modified jet boundaries are less susceptible to disturbances of arbitrary frequency than for a plain jet with velocity discontinuities[4] (as in the tests just noted), and the fact that the changes in spectrum shape were as anticipated support the assumption of smallness of the effect in this work, unless the turbulence

Note added in proof: It is for this reason that the R.R. Conway is 8-10 db. quieter than the Avon at the same thrust[12].

frequencies happened to have a large energy content near the frequency for maximum instability of the jet. In the latter case the conclusions drawn would be pessimistic; they are subject to the assumed ineffectiveness of the initial turbulence on the noise produced*, an assumption which can only be clarified after a considerable amount of further work, including correlation of turbulence, shear and the noise produced. Since turbulence must be introduced to produce the finite velocity gradients, the results can be considered to be of practical importance. The case of a *separate* auxiliary flow around a plain jet is rather different, new turbulence being generated at the intersurface, causing a rounding off of the velocity profile. This contrasts with the case investigated (where the corresponding turbulence, functionally, was initially present), which may be taken to indicate the order of the changes in sound output arising from the introduction of an auxiliary flow. This is permissible if the *difference* in turbulence does not alter the noise output by an amount comparable with the changes noted, a point which must await further work.

It has been shown that the modification of a square exit velocity profile to one approximating to that of fully established turbulent pipe flow results in a decrease in noise level varying between 2½ and 5 decibels in the subsonic region for the same exit diameter and maximum velocity. This reduction in noise level is accompanied by a considerable loss of thrust, being one quarter of the original value.

On comparing the subsonic noise levels arising from various jets having the *same thrust*, and *either* the same maximum velocities or equal diameters, it is found that the changes occurring are smaller and opposite in nature. A noise reduction is apparent if the velocity gradients can be reduced, but only if the jet can be made larger to obtain the thrust, the position being worsened if instead the central velocity is raised to give the same thrust. Thus, in Fig. 7, the velocity profiles in the order "a," "m" and "b" give successively lower noise levels.

Above the critical pressure, the increased noise levels are delayed, and are reduced to very little more than a continuation of the subsonic law at the 30° station. This is consistent with a delay in the formation of shock waves within the stream to a higher pressure ratio and/or to a decreased instability of the eddy system with consequent refraction away from the stream direction of the sound resulting from the interaction of stream disturbances with the shock waves. Owing to the delay of the onset of the characteristic choked jet noise, the reduction in noise level is variable up to a maximum of 10 decibels.

The reason for the comparative ineffectiveness of the modification to the velocity profile on the noise produced by the turbulent mixing is probably that the bulk of the noise is generated some distance from the jet exit, so that alterations in the velocity profile at the exit are largely masked by the free turbulence before reaching that region. The contours of equal intensity determined for a one-inch diameter jet[6] appear to confirm that the major bulk of the noise is not produced within the first few diameters distance from the exit.

*The increased turbulence due to re-heat does not appear to give rise to additional noise; F. B. Greatrex, Aeronautical Acoustics, *Journal of the Royal Aeronautical Society*, April 1954.

Although the experiments described and the comparisons drawn are by no means conclusive with regard to the possibilities of the introduction of an auxiliary flow, it is suggested that the subsonic noise reductions attainable by such a technique are not likely to be large in comparison with the magnitude of reduction considered desirable[5], and that a reduction in jet efflux velocity as a whole is the more effective, a 13 per cent. reduction decreasing the higher noise levels by 4 decibels. However, in view of the increasing severity of the problem, even these modest reductions may be worth serious consideration. The results are possibly very slightly pessimistic, due to the approximations made in drawing comparisons but, like possible small instrument errors, this is hardly likely to affect the general conclusions. It should be emphasised that these experiments were performed with a "cold" air jet exhausting from a stationary nozzle into an otherwise still atmosphere, and that the modified profile used was equivalent to a comparatively small auxiliary flow.

REFERENCES

1. LIGHTHILL, M. J. (1952). On Sound Generated Aerodynamically. *Proc. Roy. Soc.* A.211, p. 564, 1952.
2. POWELL, A. (1953). On the Noise Emanating from a Two-dimensional Jet above the Critical Pressure. *Aeronautical Quarterly*, Vol. IV, Part II, February 1953.
3. POWELL, A. (1953). On the Mechanism of Choked Jet Noise. *Proc. Phys. Soc.* B, 66, p. 1039, 1953.
4. POWELL, A. (1953). On Edge Tones and Associated Phenomena. *Acustica*, Vol. 3, p. 233, 1953.
5. RICHARDS, E. J. (1953). Research Work on the Aerodynamic Noise from Jets and Associated Problems. *Journal of the Royal Aeronautical Society*, May 1953.
6. WESTLEY, R. and LILLEY, G. M. (1950). An investigation of the Noise Field from a Small Jet and Methods for its Reduction. College of Aeronautics Report No. 53, 1952.
7. HARROP, R. (1951). Method for Designing Wind Tunnel Contractions. *Journal of the Royal Aeronautical Society*, 55, p 169, March 1951.
8. GOLDSTEIN, S. (Ed.) (1938). *Modern Developments in Fluid Dynamics.* O.U.P., 1st Edition, 1938.
9. TAYLOR, G. I. (1948). Pitot Pressures in Moist Air. R. & M. 2248, 1948.
10. YOUNG, A. D. and MAAS, J. N. (1937). The Behaviour of a Pitot Tube in a Transverse Total-pressure Gradient. R. & M. 1770, 1937.
11. LASSITER, W. and HUBBARD, H. H. (1952). Experimental Studies of Noise from Subsonic Jets in Still Air. N.A.C.A., T.N. 2757, August 1952.
12. POWELL, A. (1954). A Survey of Experiments on Jet Noise. *Aircraft Engineering*, January 1954.

The Second Order Terms in Two-Dimensional Tunnel Blockage

L. C. WOODS, D.Phil., A.F.R.Ae.S.

(formerly New Zealand Scientific Defence Corps, seconded to the Aerodynamics Division of the National Physical Laboratory; now Lecturer, University of Sydney)

Summary: This paper gives a new calculation of the solid and wake blockage for compressible subsonic flow about a symmetrical two-dimensional aerofoil, midway between symmetrically disposed tunnel walls, which need not be straight. Previous calculations have been based on the theory of sources, and the results obtained have usually involved only first order terms. At high subsonic Mach numbers the second order terms become important; they are given in this paper. The theory is based on an integral equation, which is exact for incompressible flow, and which is more accurate than linear pertubation theory in compressible flow. The effect on blockage of a possible increase in the boundary layer displacement thickness on the tunnel wall, due to the presence of the aerofoil, is investigated, and finally a method of calculating the total blockage from wall pressure measurements is given.

1. Introduction

The free-stream characteristics of full-scale wings must often be obtained from experiments on models between wind tunnel walls. Two basic corrections must be applied to these wind tunnel results, namely Reynolds number corrections, and corrections arising from the constraining effect of the tunnel walls on the flow. Reynolds number corrections can be reduced by using larger models, but for a given wind tunnel this increases the magnitude of the latter corrections. Moreover tunnel wall effects increase with Mach number, an increase which is especially rapid near the speed of sound. Thus the steady increase in the size and speed of aircraft over recent years has increased the importance of a knowledge of second order terms in wind tunnel corrections. Of course, second order terms in any approximate theory should be calculated, if possible, even when there is no intention of using them, as they give useful information about the range of validity of the first order terms.

This paper deals with that effect of wind tunnel walls on the flow about two-dimensional bodies known descriptively as "blockage effect." The subject was initiated by Lock[4] in 1929 and has been developed by a number of people to the stage described by Thompson in Ref. 6. Apart from the numerical investigations of Thom[11], the calculations, which have usually been confined to first order terms, have been based on a representation of the aerofoil by a line-source distribution and the linear pertubation theory of compressible flow[7]. The method of this paper is based on an integral equation, which is exact in incompressible flow and

Originally received November 1952.

[The Aeronautical Quarterly, Volume IV, February 1954]

which is more accurate than the linear pertubation theory in compressible flow. It is not valid, however, in the transonic range†.

The principal results of the paper are embodied in equations (38), (39), (40), (44) and (48), the novelty of which is in the second order terms.

Notation

The following list defines the most important symbols:—

x, y	the physical plane
H	tunnel width an infinite distance upstream
$H-2k$	effective tunnel width an infinite distance downstream
b	width of the solid sting representing the wake
s, n	distances measured along and normal to a streamline respectively
q, θ	velocity vector in polar co-ordinates
ϕ, ψ	plane of velocity equipotentials (ϕ=constant) and streamlines (ψ=constant) defined by $$d\phi = qds, \quad d\psi = \frac{\rho}{\rho_0} qdn \quad . \quad . \quad . \quad (1)$$
ρ, ρ_0	local and stagnation densities respectively
U, V	velocities at an infinite distance up and down stream respectively
M	local Mach number
β	$=(1-M^2)^{\frac{1}{2}}$
r	is defined by $$r = \int_{q=U}^{q} \beta d\left(\log \frac{U}{q}\right) \quad . \quad . \quad . \quad . \quad (2)$$
m	$=\beta\rho_0/\rho$
γ	ratio of the specific heats
δ	$=q/U-1$
p	the pressure
C_p	pressure coefficient
C_D	drag coefficient
a	defined in Fig. 1
c	aerofoil chord
ct	maximum thickness of the aerofoil
A	area of aerofoil profile
$J(x)$	second moment of area of profile about x
ε	the blockage factor, defined by equation (12)

Suffixes and Indices

∞	denotes values at $\phi=-\infty$ (upstream)
*	distinguishes free-stream quantities from corresponding quantities in the tunnel
$_h$	denotes tunnel wall values
$_1$	denotes values at an infinite distance downstream

†Transonic blockage receives some attention in Ref. 10.

2. The Basic Integral Equation

A few expansions useful in the subsequent theory can be derived by replacing q/U by $1+\delta$ in the well-known relation

$$M^2 = \frac{(q/U)^2 M_\infty^2}{1-\frac{1}{2}(\gamma-1)M_\infty^2\{(q/U)^2-1\}}. \quad . \quad . \quad . \quad . \quad (3)$$

Then from the definitions of the various quantities it is found that†

$$\beta = \beta_\infty\left\{1-\frac{M_\infty^2}{\beta_\infty^2}\left(1+\frac{\gamma-1}{2}M_\infty^2\right)\delta\right\}+O(\delta^2) \quad . \quad . \quad . \quad (4)$$

$$\frac{\rho_\infty}{\rho} = 1+M_\infty^2\delta+O(\delta^2). \quad . \quad . \quad . \quad . \quad . \quad . \quad . \quad . \quad (5)$$

$$m = m_\infty\left\{1+\frac{\gamma+1}{2\beta_\infty^2}M_\infty^4\delta\right\}+O(\delta^2) \quad . \quad . \quad . \quad . \quad . \quad (6)$$

and

$$r = -\beta_\infty\delta\left\{1-\frac{\delta}{2\beta_\infty^2}\left(1+\frac{\gamma-1}{2}M_\infty^4\right)\right\}+O(\delta^3). \quad . \quad . \quad (7)$$

Similarly, since

$$C_p \equiv \frac{p-p_\infty}{\frac{1}{2}\rho_\infty U^2},$$

$$C_p = -2\delta(1+\tfrac{1}{2}\beta_\infty^2\delta)+O(\delta^3),$$

i.e.

$$\delta = -\tfrac{1}{2}C_p(1+\tfrac{1}{4}\beta_\infty^2 C_p)+O(C_p^3). \quad . \quad . \quad . \quad . \quad (8)$$

Finally from (7) and (8),

$$\frac{r}{\beta_\infty} = \tfrac{1}{2}C_p\left\{1+\tfrac{1}{2}\left(1+\frac{\gamma+1}{4}\frac{M_\infty^4}{\beta_\infty^2}\right)C_p\right\}+O(C_p^3). \quad . \quad . \quad (9)$$

In Ref. 1 the author showed that when the approximation

$$m = m_\infty \quad . \quad . \quad . \quad . \quad . \quad . \quad . \quad (10)$$

is admissible, r and θ are conjugate harmonic functions in the $(\phi, m_\infty\psi)$-plane††, from which it is possible to establish the solution[2]

$$r+i\theta = \frac{1}{HU\beta_\infty}\int_{-\infty}^{\infty}\left\{\theta_0\coth\frac{\pi}{HU\beta_\infty}(\phi'-\phi-im_\infty\psi)-\theta_h\tanh\frac{\pi}{HU\beta_\infty}(\phi'-\phi-im_\infty\psi)\right\}d\phi'$$
$$+\tfrac{1}{2}\int_{q=U}^{V}\beta d\left(\log\frac{U}{q}\right), \quad . \quad . \quad . \quad . \quad (11)$$

†See the footnote to equation (13).

††Equations (2) and (10) are due to von Kármán[3], who used them to show that ϕ and ψ are approximately harmonic functions in the (r, θ)-plane.

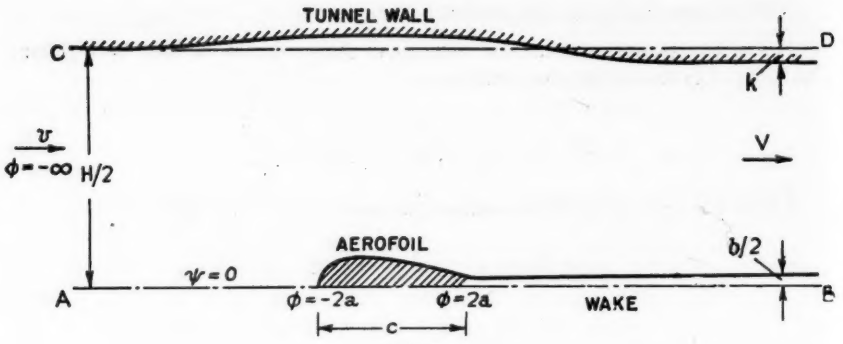

Fig. 1.

where θ_0 specifies the flow direction on the tunnel centre line, $\psi=0$, and θ_h specifies the flow direction on the tunnel wall where, from equation (1), $\psi=HU\beta_\infty/(2m_\infty)$.

It is apparent from equations (4) and (6) that in subsonic flow the approximation (10) is an improvement over the approximation of linear perturbation theory, namely $\beta=\beta_\infty$.

As in Fig. 1 the aerofoil is assumed to lie on $\psi=0$ in $-2a\leqslant\phi\leqslant 2a$. CD is parallel to and at a distance of $\frac{1}{2}H$ from the tunnel axis AB. The distances y_0 and y_h will be measured from AB and CD respectively. It is assumed that the curved wall shown in the figure has been displaced downwards to include the effect of the displacement thickness of the boundary layer that occurs on the wall when the tunnel is running empty. Most wind tunnels have straight walls, *i.e.* $\theta_h=0$, but this will not be assumed here because (*i*) flexible wall tunnels are sometimes employed, and (ii) the presence of the aerofoil may result in an increment to the boundary layer displacement thickness on the tunnel wall. It is because of this last possibility that the tunnel wall has been given a downwards displacement k downstream at infinity in Fig. 1.

The effect of the aerofoil wake is assumed to be equivalent to that of a sting of width b extending for an infinite distance downstream from the trailing edge of the aerofoil. In Section 3 it is shown that b is related to the drag coefficient C_D.

Equation (11), on which the theory of this paper is based, is essentially an integral equation. The functions $\theta_0(\phi')$ and $\theta_h(\phi')$ cannot be assigned until the relation $s=s(\phi')$ is known on both the aerofoil and the wall, and in turn this relation is unknown until $q=q(\phi')$, or equivalently $r=r(\phi')$ is known on the boundaries. An iterative method of solving the equation is given in Ref. 2.

The tunnel blockage factor ε is defined by the simultaneous equations

$$q^*_\infty=U\{1+\varepsilon(x,y)\}, \quad q(x,y)=q^*(x,y), \quad . \quad . \quad . \quad (12)$$

which in words may be interpreted thus:—the velocity q is determined at some point (x,y) in the tunnel, the walls are then removed, but at the same time the

velocity at infinity is increased to $U(1+\varepsilon)$ so as to maintain the same velocity at (x, y). The importance of ε lies in the fact that on the aerofoil surface its dominant term is a constant.

3. Calculation of the Blockage Factor

The calculation of ε in this section depends on an initial assignment of the order of magnitude of various quantities associated with the aerofoil and the tunnel.

The most important assumption is that†

$$\left(\frac{c}{\beta_\infty H}\right)^2 = O(t), \quad . \quad . \quad . \quad . \quad . \quad . \quad (13)$$

where t is the ratio of the maximum aerofoil thickness to the chord. For conventional aerofoils,

$$\frac{A}{c^2} = O(t), \quad . \quad . \quad . \quad . \quad . \quad . \quad (14)$$

and, except near the nose,

$$\theta_0 = O(t), \quad . \quad . \quad . \quad . \quad . \quad . \quad (15)$$

and

$$\frac{q}{U} = 1 + \frac{t}{\beta_\infty} O(1) + O(t^2),$$

i.e.

$$\beta_\infty \delta = O(t). \quad . \quad . \quad . \quad . \quad . \quad . \quad (16)$$

It is shown later that

$$\varepsilon = O(t^2), \quad . \quad . \quad . \quad . \quad . \quad . \quad (17)$$

a result which it is necessary to know during the calculation. It is assumed, for the wall displacement k and the wake displacement b, that

$$\frac{b+2k}{\beta_\infty^3 H} = O(t^2). \quad . \quad . \quad . \quad . \quad . \quad (18)$$

On the tunnel wall it will be assumed that

$$\theta_h = O(t), \quad . \quad . \quad . \quad . \quad . \quad . \quad (19)$$

while in the next section it is shown that the velocity on the tunnel wall q_h is

$$q_h = U\{1 + O(t^2)\}. \quad . \quad . \quad . \quad . \quad (20)$$

The first step in the determination of ε is to perform the calculation implicit in equation (12). If H tends to infinity, then on $\psi = 0$, equation (11) reduces to

$$\int_{q=U}^{q^*} \beta d\left(\log \frac{U}{q}\right) = \frac{1}{\pi} \int_{-\infty}^{\infty} \frac{\theta^* d\phi'}{\phi' - \phi}.$$

†By the "O" notation in this paper is meant $\left(\frac{c}{\beta_\infty H}\right)^2 \leqq Kt$, where $K \simeq 1$.

Next the velocity at infinity is increased to $U(1+\varepsilon)$ so that $q^*=q$, when

$$\int_{q=U(1+\varepsilon)}^{q} \beta d\left(\log\frac{U}{q}\right)=\frac{1}{\pi}\int_{-\infty}^{\infty}\frac{\theta^*_0\,d\phi'}{\phi'-\phi}. \quad . \quad . \quad . \quad . \quad . \quad (21)$$

Now if ε were constant the functions $\theta_0(\phi')$ and $\theta^*_0(\phi')$ would be identical. The variable part of ε is shown later to be $O(t^3)$, from which it can be deduced that

$$\theta_0=\theta^*_0(1+O(t^3))=\theta^*_0+O(t^4). \quad . \quad . \quad . \quad . \quad . \quad (22)$$

On $\psi=0$ equation (11) becomes

$$\int_{q=U}^{q}\beta d\left(\log\frac{U}{q}\right)=\frac{1}{HU\beta_\infty}\int_{-\infty}^{\infty}\left\{\theta_0\coth\frac{\pi}{HU\beta_\infty}(\phi'-\phi)-\theta_h\tanh\frac{\pi}{HU\beta_\infty}(\phi'-\phi)\right\}d\phi'+$$

$$+\tfrac{1}{2}\int_{q=U}^{V}\beta d\left(\log\frac{U}{q}\right). \quad . \quad . \quad . \quad . \quad . \quad (23)$$

Thus it follows from equations (21), (22) and (23) that

$$-\int_{q=U}^{U(1+\varepsilon)}\beta d\left(\log\frac{U}{q}\right)=\frac{1}{HU\beta_\infty}\int_{-2a}^{2a}\theta_0\left\{\frac{1}{\frac{\pi}{HU\beta_\infty}(\phi'-\phi)}-\coth\frac{\pi}{HU\beta_\infty}(\phi'-\phi)\right\}d\phi'+$$

$$+\frac{1}{HU\beta_\infty}\int_{-\infty}^{\infty}\theta_h\tanh\frac{\pi}{HU\beta_\infty}(\phi'-\phi)\,d\phi'-\tfrac{1}{2}\int_{q=U}^{V}\beta d\left(\log\frac{U}{q}\right)+O(t^4), \quad . \quad (24)$$

where the range of one integral has been reduced, since outside $-2a\leqslant\phi'\leqslant 2a$ the function $\theta_0(\phi')$ vanishes.

By means of equations (4) and (17),

$$-\int_{q=U}^{U(1+\varepsilon)}\beta d\left(\log\frac{U}{q}\right)=\beta_\infty\varepsilon+O(t^4). \quad . \quad . \quad . \quad . \quad . \quad (25)$$

The effective tunnel width downstream at infinity is $(H-b-2k)$ where the density is ρ_1. Thus from equations (5), (18) and the continuity of mass

$$V=\frac{\rho_\infty}{\rho_1}\left(\frac{UH}{H-b-2k}\right)$$

$$=U\left\{1+\frac{b+2k}{\beta_\infty{}^2H}+O(t^4)\right\}; \quad . \quad . \quad . \quad . \quad . \quad (26)$$

hence

$$-\tfrac{1}{2}\int_{q=U}^{V}\beta d\left(\log\frac{U}{q}\right)=\frac{b+2k}{2\beta_\infty H}+O(t^4). \quad . \quad . \quad . \quad . \quad . \quad (27)$$

Now the largest value of $(\phi'-\phi)/U$ occurring in the first integral of equation (24) is approximately equal to c, so that expanding the integrand in a power series, and making use of equations (13), (25) and (27), gives

$$\varepsilon = -\frac{\pi}{3H^2U^2\beta_\infty{}^3}\int_{-2a}^{2a}\theta_0(\phi'-\phi)\left\{1-\frac{1}{15}\left(\frac{\pi}{HU\beta_\infty}\right)^2(\phi'-\phi)^2+O(t^2)\right\}d\phi' +$$

$$+\frac{1}{HU\beta_\infty{}^2}\int_{-\infty}^{\infty}\theta_h\tanh\frac{\pi}{HU\beta_\infty}(\phi'-\phi)\,d\phi'+\frac{b+2k}{2\beta_\infty{}^2H}+O(t^4). \quad . \quad (28)$$

When ϕ tends to $-\infty$, equations (23) and (27) yield

$$\frac{1}{U}\int_{-2a}^{2a}\theta_0 d\phi' = \frac{1}{U}\int_{-\infty}^{\infty}\theta_h\,d\phi'+\tfrac{1}{2}b+k+O(t^4),$$

but from (19) and (20)

$$\frac{1}{U}\int_{-\infty}^{\phi}\theta_h\,d\phi' = \int_{-\infty}^{\phi}\{1+O(t^2)\}\,dy_h = y_h\{1+O(t^2)\} \quad . \quad . \quad . \quad . \quad (29)$$

In particular
$$\frac{1}{U}\int_{-\infty}^{\infty}\theta_h\,d\phi' = -k\{1+O(t^2)\}, \quad . \quad . \quad . \quad . \quad . \quad . \quad . \quad (30)$$

therefore
$$\frac{1}{U}\int_{-2a}^{2a}\theta_0 d\phi' = \tfrac{1}{2}b\{1+O(t^2)\}, \quad . \quad . \quad . \quad . \quad . \quad . \quad . \quad (31)$$

assuming b and k to be of the same order. This equation is but a special case of

$$\frac{1}{U}\int_{-2a}^{\phi}\theta_0 d\phi' = y_0\{1+O(t^2)\}, \quad . \quad . \quad . \quad . \quad . \quad . \quad . \quad (32)$$

which receives further justification in the Appendix.

On the aerofoil,

$$d\phi' = U\{1+\delta+O(t^2)\}\,dx', \quad . \quad . \quad . \quad . \quad . \quad . \quad (33)$$

whereas on the wall, from (20),

$$d\phi' = U\{1+O(t^2)\}\,dx'. \quad . \quad . \quad . \quad . \quad . \quad . \quad (34)$$

If equation (28) is now integrated by parts, it follows from equations (17), (18) and (29)-(34) that

$$\varepsilon = \frac{\pi}{6H^2\beta_\infty{}^3}\,2\int_{-\frac{1}{2}c}^{\frac{1}{2}c}y_0\left\{1-\frac{1}{5}\left(\frac{\pi}{H\beta_\infty}\right)^2(x'-x)^2+\delta\right\}dx'+\frac{b}{2\beta_\infty{}^2H}\left\{1+\frac{\pi}{3\beta_\infty H}(x-\tfrac{1}{2}c)\right\}-$$

$$-\frac{\pi}{\beta_\infty{}^3H^2}\int_{-\infty}^{\infty}y_h\,\mathrm{sech}^2\frac{\pi}{H\beta_\infty}(x'-x)\,dx'+O(t^{3\cdot5}), \quad . \quad . \quad . \quad (35)$$

where the origin of x has been taken at the mid-chord point. To complete the theory it remains to calculate the quantities b and δ.

The value of b is easily calculated from the conservation of momentum equation, which yields

$$-D=(p_\infty+\rho_\infty U^2-p_1-\rho_1 V^2)H,$$

where the suffix "1" denotes values an infinite distance downstream and D is the drag per unit span on the aerofoil. (k is put equal to zero in this calculation, otherwise part of D will be a resultant horizontal pressure acting on the tunnel walls.) From (18) and (26),

$$\frac{V}{U}-1\equiv\delta_1=\frac{b}{\beta_\infty{}^2H}=O(t^2),$$

while from (5) and (8)

$$p_1=p_\infty-\rho_\infty U^2\{\delta_1+O(t^4)\},$$

$$\rho_1=\rho_\infty\{1-M_\infty{}^2\delta_1+O(t^4)\}.$$

By these equations the expression for D can be reduced to

$$D=\rho_\infty U^2 b\{1+O(t^2)\}.$$

Thus

$$\frac{b}{c}=\tfrac{1}{2}C_D\{1+O(t^2)\}. \quad . \quad . \quad . \quad . \quad . \quad . \quad . \quad (36)$$

A reasonable approximation to the value of δ can be obtained from equation (21). From equations (4), (16) and (33) it is found that

$$\delta=-\frac{1}{\beta_\infty\pi}\int_{-\frac{1}{2}c}^{\frac{1}{2}c}\frac{dy(x')}{x'-x}+O(t^2). \quad . \quad . \quad . \quad . \quad . \quad (37)$$

By equations (36) and (37) the equation for ε may be written in the form

$$\varepsilon=\frac{\pi A}{6H^2\beta_\infty{}^3}\left\{1+\frac{\Delta}{\beta_\infty}-\frac{1}{5}\left(\frac{\pi}{H\beta_\infty}\right)^2\frac{J(x)}{A}\right\}+\frac{cC_D}{4\beta_\infty{}^2H}\left\{1+\frac{\pi}{3\beta_\infty H}(x-\tfrac{1}{2}c)\right\}-$$

$$-\frac{\pi}{\beta_\infty{}^3H^2}\int_{-\infty}^{\infty}y_h\operatorname{sech}^2\frac{\pi}{H\beta_\infty}(x'-x)\,dx'+O(t^{3\cdot5}), \quad . \quad . \quad . \quad (38)$$

where

$$\Delta=-\frac{2}{\pi A}\int_{-\frac{1}{2}c}^{\frac{1}{2}c}\int_{x'=-\frac{1}{2}c}^{\frac{1}{2}c}\frac{dy(x')}{x'-x}y(x)\,dx. \quad . \quad . \quad . \quad . \quad . \quad (39)$$

It is apparent from (38), (13) and (15) that the dominant term in ε (assuming y_h negligible) will certainly be $O(t^2)$, as already assumed, if, for example, $M\leqslant0{\cdot}90$, $t\leqslant0{\cdot}1$ and $C_D\leqslant0{\cdot}06$. The variable term in ε is clearly $O(t^3)$.

The first and second terms in equation (38) are for obvious reasons, termed the "solid" and "wake" blockage factors respectively. The first order terms in this equation are well known[5, 6]. The blockage equation reveals that the solid blockage is a maximum at the centre of area of the profile and falls off towards the trailing and leading edges. This variation in solid blockage has been obtained by Thom[11] using arithmetical methods. It will be noticed from (38) that, as stated in the Summary, the second order terms in the blockage factor gain in relative importance with increasing Mach number.

Some idea of the magnitude of the second order terms in the solid blockage factor can be gained by considering the following simple examples:—
(*a*) a circular arc profile defined by (approximately)

$$y_0=\tfrac{1}{2}tc\left\{1-\left(\frac{2x}{c}\right)^2\right\},$$

for which the solid blockage is found to be

$$\varepsilon_s=\frac{\pi}{9}\left(\frac{c}{H}\right)^2\frac{t}{\beta_\infty{}^3}\left\{1+\frac{3}{\pi}\frac{t}{\beta_\infty}-\frac{\pi^2}{100}\left[1+20\left(\frac{x}{c}\right)^2\right]\left(\frac{c}{H\beta_\infty}\right)^2\right\},$$

and (*b*) an elliptic profile for which

$$y_0=\tfrac{1}{2}tc\left\{1-\left(\frac{2x}{c}\right)^2\right\}^{\frac{1}{2}},$$

when

$$\varepsilon_s=\frac{\pi^2}{24}\left(\frac{c}{H}\right)^2\frac{t}{\beta_\infty{}^3}\left\{1+\frac{t}{\beta_\infty}-\frac{\pi^2}{80}\left[1+16\left(\frac{x}{c}\right)^2\right]\left(\frac{c}{H\beta_\infty}\right)^2\right\}.$$

Thompson[6] gives as a general result

$$\varepsilon_s=\frac{\pi A}{6\beta_\infty{}^3H^2}(1+1{\cdot}2t),$$

where 1·2 is an empirical constant.

Two applications of the third term on the right hand side of equation (38) suggest themselves:—

(*i*) If the flexible wall is adjusted so that ε vanishes, then (38) can be regarded as an integral equation for y_h; alternatively y_h can be determined for vanishing ε from a knowledge of the position of a "constant pressure wall"[2].

(*ii*) Suppose, as suggested in Section 2, that the varying pressure gradient produced on the wall by the aerofoil causes an increment k in the boundary layer displacement thickness on the wall, starting at $x=f$ and extending downstream to infinity, then from (38) the contribution to ε will be

$$\varepsilon_k=\frac{k}{\beta_\infty{}^2H}\left\{1-\tanh\frac{\pi}{H\beta_\infty}(f-x)\right\},$$

i.e.

$$\varepsilon_k\simeq\frac{k}{\beta_\infty{}^2H}\left\{1+\frac{\pi}{H\beta_\infty}(x-f)\right\}. \quad . \quad . \quad . \quad . \quad . \quad (40)$$

Some evidence on the existence of k appears in the next section.

4. Calculation of Blockage from Wall Pressure Measurements

On the tunnel wall, *i.e.* on $\psi=HU\beta_\infty/(2m_\infty)$, equation (11) yields, after an integration by parts,

$$\frac{r_h}{\beta_\infty} = -\frac{cC_D}{4\beta_\infty{}^2 H}\left\{1-\tanh\frac{\pi}{HU\beta_\infty}(2a-\phi)\right\} - \frac{\pi}{H^2\beta_\infty{}^3 U}\int_{-2a}^{2a} y_0\,\mathrm{sech}^2\frac{\pi}{HU\beta_\infty}(\phi'-\phi)\,d\phi' +$$

$$+\frac{\pi}{H^2\beta_\infty{}^3 U}\int_{-\infty}^{\infty} y_h\,\mathrm{cosech}^2\frac{\pi}{HU\beta_\infty}(\phi'-\phi)\,d\phi' + O(t^4), \quad . \quad . \quad (41)$$

in the calculation of which equations (18), (27), (29)-(32) and (36) have been used. The value of r_h/β_∞ is given in terms of the pressure coefficient on the wall by equation (9).

It follows from (9), (18) and (41) that, at an infinite distance downstream,

$$c_{p1} + \frac{cC_D}{\beta_\infty{}^2 H} + \frac{4k}{\beta_\infty{}^2 H} = 0, \quad . \quad . \quad . \quad . \quad . \quad . \quad (42)$$

which can be written as

$$\frac{k}{c} = -\tfrac{1}{4}\left\{\left(\frac{H}{c}\right)^2 \beta_\infty{}^2 C_p + C_D\right\}. \quad . \quad . \quad . \quad (43)$$

This equation has been applied to some results obtained in the Royal Aircraft Establishment High Speed Tunnel by Mair and Gamble[9]. In this tunnel, for which $H=10$ ft., three different sized aerofoil models of section N.A.C.A. 0015 were tested at various Mach numbers, and wall pressure measurements were made. Fig. 2 shows values of k calculated from the results obtained in these experiments. These values of k are almost double the corresponding values of $\frac{1}{2}cC_D$, the wake displacement thickness ! These results are not conclusive evidence of the existence of k but if k is zero, the discrepancy between the values of C_p and C_D remains to be explained. This discrepancy has been experienced in other tunnels. Direct measurements of the tunnel wall boundary layer in the presence and absence of the aerofoil would provide conclusive evidence.

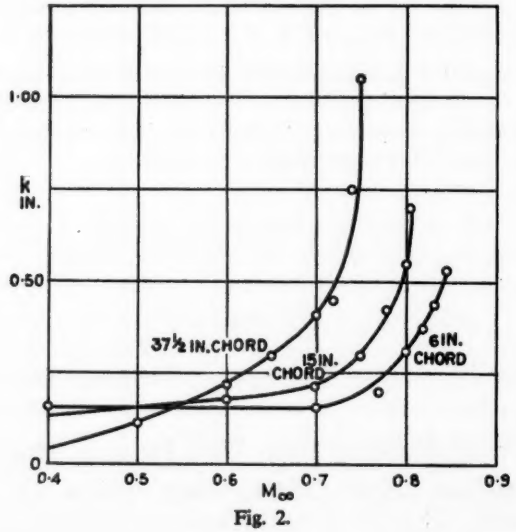

Fig. 2.

For points on the wall opposite the aerofoil a calculation similar to that of Section 3 reduces (41) to

$$-\frac{r_h}{\beta_\infty}=\frac{cC_D}{4\beta_\infty^2 H}\left\{1+\frac{\pi}{H\beta_\infty}(x-\tfrac{1}{2}c)\right\}+\frac{\pi A}{2H^2\beta_\infty^3}\left\{1+\frac{\Delta}{\beta_\infty}-\left(\frac{\pi}{H\beta_\infty}\right)^2\frac{J(x)}{A}\right\}+$$

$$+\frac{\pi}{H^2\beta_\infty^3}\int_{-\infty}^{\infty} y_h\,\mathrm{cosech}^2\frac{\pi}{H\beta_\infty}(x'-x)\,dx'+O(t^{3\cdot5}). \quad . \quad (44)$$

If it is assumed for simplicity that $y_h=0$, then equations (38), (42) and (44) yield

$$\varepsilon=-\frac{r_h}{3\beta_\infty}-\frac{1}{6}C_{p1}+\frac{2}{15}\left(\frac{\pi}{H\beta_\infty}\right)^2\times\frac{J(x)}{H\beta_\infty^2}, \quad . \quad . \quad . \quad (45)$$

by which it is possible to estimate ε from a knowledge of the values of the wall pressure coefficients opposite the aerofoil and well downstream.

5. The Increase in Drag due to Blockage

The drag on an aerofoil in a wind tunnel is larger than that in free air for two reasons:—(*i*) because of the increase in velocity at the aerofoil caused by the tunnel walls, and (*ii*) because of the existence of a pressure gradient due mainly to the presence of the wake.

From Bernoulli's theorem the pressure gradient due to the blockage is

$$\frac{\partial p}{\partial x}=-\rho U^2\frac{\partial\varepsilon}{\partial x}.$$

The drag increment ΔD due to this is given by

$$\Delta D=\oint p\,dy=-2\int_{-\frac{1}{2}c}^{\frac{1}{2}c} y\frac{\partial p}{\partial x}\,dx$$

$$\simeq 2U^2\int_{-\frac{1}{2}c}^{\frac{1}{2}c} y\rho_\infty\{1-M_\infty^2\delta\}\frac{\partial\varepsilon}{\partial x}\,dx, \text{ from (5).}$$

Thus from (36), (38) and (40)

$$\Delta D\simeq\frac{\pi A}{6H^2\beta_\infty^3}D\left(1+\frac{6k}{b}\right), \quad . \quad . \quad . \quad (46)$$

where the contribution to ΔD from the integral of $\partial J/\partial x$ has been ignored, since J is very nearly a symmetric function about the mid-chord point.

Now if D^* is the free stream drag for a velocity at infinity of $U(1+\varepsilon_m)$, ε_m being the mean value of ε over the aerofoil chord, then clearly

$$D^*=D-\Delta D=D\left\{1-\frac{\pi A}{6H^2\beta_\infty^3}\left(1+\frac{6k}{b}\right)\right\},$$

$$i.e.\ \rho^*_\infty(1+\varepsilon_m)^2C_D^*=\rho_\infty C_D\left\{1-\frac{\pi A}{6H^2\beta_\infty^3}\left(1+\frac{6k}{b}\right)\right\}. \quad . \quad . \quad (47)$$

By an application of (5)

$$\rho^*_\infty = \rho_\infty (1 - M_\infty^2 \varepsilon_m),$$

so that (47) can be written

$$\frac{C_D^* - C_D}{C_D} \simeq - \left\{ (2 - M_\infty^2)\varepsilon_m + \frac{\pi A}{6H^2\beta_\infty^3}\left(1 + \frac{6k}{b}\right)\right\} . \qquad (48)$$

From this equation it appears that a relatively small value of k can have a significant effect on the correction to the drag coefficient.

APPENDIX

An Alternative Method for Incompressible Flow

The value of the blockage in incompressible flow can be deduced from the exact equation[2]

$$\frac{Ue^{i\theta}}{q} = 1 - \frac{\pi}{H^2 U}\int_{-\infty}^{\infty} \left\{ y_0 \operatorname{cosech} \frac{\pi}{HU}(\phi' - \phi - i\psi) - y_h \operatorname{sech} \frac{\pi}{HU}(\phi' - \phi - i\psi)\right\} d\phi',$$

by a calculation similar to that based on equation (11) in Section 3. The result, which is obtained without the use of equations (29) and (32), is that given by (38) and (39) with $\beta_\infty = 0$.

References

1. Woods, L. C. (1950). The Two-dimensional Subsonic Flow of an Inviscid Fluid about an Aerofoil of Arbitrary Shape. R. & M. 2811.
2. Woods, L. C. (1952). Compressible Subsonic Flow in Two-dimensional Channels: The Direct and Indirect Problems. A.R.C. 14,838.
3. Kármán, Th. von (1941). Compressibility Effects in Aerodynamics. *Journal of the Aeronautical Sciences*, Vol. 8, No. 9, October 1941.
4. Lock, C. N. H. (1929). The Interference of a Wind Tunnel on a Symmetrical Body. R. & M. 1275.
5. Thom, A. (1943). Blockage Corrections in a Closed High Speed Wind Tunnel. R. & M. 2033.
6. Thompson, J. S. (1948). Present Methods of Applying Blockage Corrections in a Closed Rectangular High Speed Wind Tunnel. Unpublished M.O.S. Report.
7. Golstein, S. and Young, A. D. (1943). The Linear Perturbation Theory of Compressible Flow with Applications to Wind Tunnel Interference. R. & M. 1909.
8. Thom, A. (1946). The Method of Influence Factors in Arithmetical Solutions of Certain Field Problems. R. & M. 2440.
9. Mair, W. A. and Gamble, H. E. (1944). The Effect of Model Size on Measurements in the High Speed Wind Tunnel. Part I: Drag of Two-dimensional Symmetrical Aerofoils at Zero Incidence. R. & M. 2527.
10. Thom, A. (1947). Tunnel Wall Effect from Mass Flow Considerations. R. & M. 2442.
11. Thom, A. (1947). Some Arithmetical Studies of the Compressible Flow past a Body in a Channel. A.R.C. 11,010.

Adiabatic One-Dimensional Flow of a Perfect Gas through a Rotating Tube of Uniform Cross Section

K. KESTIN and S. K. ZAREMBA

(Formerly Department of Mechanical Engineering, Polish University College, London. Mr. Kestin is now at Brown University and Mr. Zaremba is now Chief Mathematician, Boulton Paul Aircraft Ltd.)

Summary: The paper contains an analysis of the flow of a perfect gas with constant specific heats through a rotating channel of constant cross-sectional area, as used in certain helicopter propulsion systems and wind-driven gas turbines. The analysis is restricted to the adiabatic one-dimensional treatment, the Coriolis accelerations acting across a section being disregarded.

The equations of motion and energy are deduced and, together with the equation of continuity, reduced to an ordinary non-linear differential equation of the first order, involving a dimensionless form of velocity and distance.

The patterns of the integral curves of the differential equation are discussed and sketched by examining their asymptotic behaviour as well as that in the neighbourhood of singular points. It is shown that there exists a critical value of the angular velocity below which the flow remains subsonic in the pipe, if the entrance velocity is subsonic; it may, however, become sonic at the exit of the pipe. For supercritical angular velocities the flow may become sonic or supersonic in the pipe if the entrance velocity attains a given "correct" but subsonic value. A method of examining for the possibility of shock formation is indicated.

The initial conditions for the differential equation are deduced for the design and for the performance problem, two new flow functions being introduced and tabulated to facilitate practical calculations. Formulae are also deduced for the calculation of the pressure and Mach number variation from the previously calculated velocity variation along the pipe.

Finally an approximate solution in closed terms is given for the case of small entrance velocities.

1. Statement of Problem and Assumptions

In some systems of jet-propelled helicopters[1, 2] and in some systems of wind driven gas turbines[3] the gaseous working fluid is transmitted through rotating channels of constant cross-sectional area, which are accommodated in the arm of the rotor, the pipes being in turn connected with a channel in the vertical hollow axis. To establish the optimum running conditions it is necessary to analyse the flow through the rotating channel and to connect the solution with the boundary conditions imposed by the design of the duct. In the arm, the gas takes part in the rotary motion about its axis at constant angular velocity ω and moves relative to the pipe

Originally received March 1952.

[The Aeronautical Quarterly, Volume IV, February 1954]

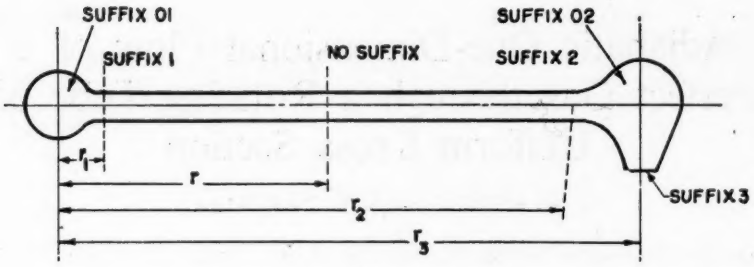

Fig. 1.

with an acceleration $V\,dV/dr$, where V is the velocity of the gas particle relative to the pipe, and r is the co-ordinate measured along the rotating arm. The object of the present paper is to write down and to discuss the equations governing the steady motion of a perfect gas under those conditions.

Figure 1 represents diagrammatically one rotating arm for a helicopter rotor, but the extension to the case of the wind-driven gas turbine application presents no difficulty. It is assumed that the fluid, whose initial state is known, is supplied along the hollow axis to a container on the axis, in which the flow velocity may be assumed to be negligible. The state of the gas in this container will be denoted by symbols with subscript "01," the gas being assumed perfect, and having constant specific heats. The isentropic index of the gas is denoted by γ.

The gas is assumed to expand through a well-rounded nozzle, ending with section "1," which is the inlet section to a constant-area pipe. The expansion from state "01" to state "1" is assumed isentropic, the gas velocity after expansion being denoted by V_1. The distance from the axis of rotation O_1 to section "1" will be denoted by r_1.

In its passage through the tube, whose constant area is denoted by A, and whose hydraulic diameter is denoted by D, the gas is accelerated due to the combined action of the pressure gradient and the dynamic acceleration in the rotating arm. The influence, if any, of a variation in level will be neglected, and also any pressure gradients, acting in the plane of a cross-section, which are due to Coriolis' accelerations. This last assumption evidently requires experimental verification, as the existence of transverse pressure gradients may cause secondary flows. However, if the cross-sectional dimensions of the tube are small compared with its length, the assumption appears to be reasonable.

It is now clear that the conventional equations of motion and energy[4, 5, 6, 7] of a compressible fluid, flowing through a constant-area pipe at rest must be modified, to take into account the inertia force, but the equation of continuity remains unaltered.

From section "2" at the end of the pipe, the gas is assumed to be compressed isentropically through a divergent, well-rounded nozzle, so that it comes to rest

relative to the arm in the second container, placed at a distance r_3 from the axis of rotation, and attains a pressure P_{02} and temperature T_{02}.

From the second container the gas is expanded isentropically through a convergent, or convergent-divergent nozzle so that it leaves the container at right angles to the axis of the pipe, the thrust thus developed providing the turning moment.

It is assumed in this paper that the driving nozzle is convergent and has an exit area A^*, there being no difficulty in extending the results to include the case of a convergent-divergent driving nozzle, if due care is taken to allow for the possibility of shock formation.

Denoting the external ("atmospheric") pressure by P_a, we have to consider two patterns of flow through the nozzle. If the pressure ratio across the driving nozzle exceeds the critical value, *i.e.* if

$$\frac{P_a}{P_{02}} > \left(\frac{2}{\gamma+1}\right)^{\frac{\gamma}{\gamma-1}} \quad . \quad . \quad . \quad . \quad . \quad . \quad (1)$$

the flow will be subsonic in the nozzle exit, and consequently the exit pressure in the nozzle, P_3, will be equal to the atmospheric pressure; thus

$$P_3 = P_a \quad . \quad . \quad . \quad . \quad . \quad . \quad (1a)$$

If, on the other hand, the pressure ratio across the nozzle is less than the critical value, *i.e.* if

$$\frac{P_a}{P_{02}} < \left(\frac{2}{\gamma+1}\right)^{\frac{\gamma}{\gamma-1}} \quad . \quad . \quad . \quad . \quad . \quad . \quad (2)$$

the exit pressure P_3 has a fixed value and depends solely upon P_{02}, being in particular independent of P_a; thus

$$P_3 = \left(\frac{2}{\gamma+1}\right)^{\frac{\gamma}{\gamma-1}} \times P_{02}. \quad . \quad . \quad . \quad . \quad . \quad (2a)$$

The flow in the nozzle exit is then sonic, and the flow velocity is equal to

$$V_3 = \left(\frac{2}{\gamma+1}\right)^{\frac{1}{2}} \times a_{02} \quad . \quad . \quad . \quad . \quad . \quad (2b)$$

where, in turn, a_{02} depends solely on the stagnation temperature T_{02}.

In the following analysis the flow is regarded as isentropic everywhere, except in the pipe, when friction in the boundary layer between sections "1" and "2" will be taken into account in an elementary way[4, 5, 6, 7]. The flow will be assumed adiabatic everywhere.

In actual applications there may be two different formulations of the general problem. It may be necessary to *design* the exit area A^* to pass a given mass flow

m' for a given state "01," the cross-section A and the hydraulic diameter D of the pipe being usually given in advance to conform to the profile of the rotating arm. The driving nozzle having been designed, it may be desired to assess the *performance* of the system under varying conditions.

Notation

A cross-sectional area of pipe

A^* exit area of driving nozzle

a speed of sound

D hydraulic diameter of pipe

F friction force

G dimensionless angular velocity defined by equation (7)

h enthalpy (total heat)

I d'Alembert (inertia) force

J Jacobian $(\mathrm{D}(X, Y)/\mathrm{D}(x, y))$

k slope of integral curve

M velocity ratio $(=V/a_{01})$

M' Mach number

m quantity defined by equation (13*c*)

m' rate of mass flow

P pressure

P_a external pressure

p quantity defined by equation (13*a*)

q quantity defined by equation (13*a*)

R Reynolds number

r distance from axis of rotation

s quantity defined by equation (33)

T absolute temperature

u quantity defined by equation (33*c*)

V velocity

v specific volume

X function defined by equation (14*a*)

X_1 linear part of function X after translation to singular point (equation (27*b*))

X_4 homogeneous polynomial of degree 4 defined in equation (21*a*)

x dimensionless co-ordinate

Y function defined by equation (14*a*)

Y_1 linear part of function Y after translation to singular point (equation (27*b*))

Y_4 homogeneous polynomial of degree 4 defined in equation (21*a*)

y square of velocity ratio ($=M^2$)

γ ratio of specific heats

Δ discriminant of equation (16)

η dependent variable after inversion, equation (20)

λ coefficient of pipe friction; slope of integral curve at singular point

$\tilde{\omega}$ pressure ratio defined by equation (35*c*)

ξ independent variable after inversion (equation (20))

ρ density

Ψ flow function defined by equation (35*a*)

ψ density of mass flow ($=m'/A$)

Ω flow function defined by equation (34*b*)

ω angular velocity

Suffixes

$_{01}$ stagnation point on axis

$_{02}$ stagnation point at end of pipe

$_1$ entrance to pipe

$_2$ exit from pipe

$_3$ exit from driving nozzle

* asterisk refers to singular point (sonic section)

$\bar{}$ bar refers to system of co-ordinates translated to singular point (equations (27*a*) and (27*b*))

2. The Basic Equations

As usual, the problem is determined by the equations of continuity, motion and energy. The *equation of continuity* is

$$\psi=\frac{V}{v}=\frac{V_3}{v_3}\frac{A^*}{A}=\text{constant} \quad . \quad . \quad . \quad . \quad (3)$$

where V is the velocity *relative to the channel* at any point, v is the specific volume, and ψ is the density of mass flow,

$$\psi=\frac{m'}{A} \quad . \quad . \quad . \quad . \quad . \quad . \quad (3a)$$

per unit area of pipe.

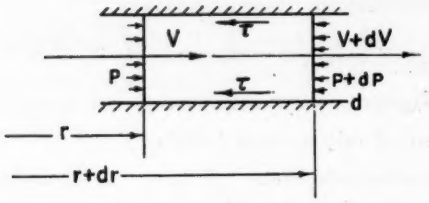

Fig. 2.

In order to derive the *equation of motion* let us fix our attention on the fluid particle shown in Fig. 2.

The dynamic action of the rotary motion can be accounted for by writing down the equation of motion with respect to the moving tube in which, in conformity with d'Alembert's principle, a fictitious force

$$dI = \frac{A}{v}\omega^2 r\,dr \qquad . \quad . \quad . \quad . \quad (4)$$

is assumed acting in the positive direction of r. Consequently the element of mass

$$dm = \frac{A}{v}\,dr$$

moves with an acceleration $V\,dV/dr$ under the influence of the inertia force dI, the pressure force $A\,dP$ and the friction force

$$dF = \tau\frac{4A}{D}\,dr$$

with

$$\tau = \lambda\frac{V^2}{2v}$$

and λ depending on the Reynolds number R, according to the Blasius formula[8] or the Nikuradse formula[8]. As a first approximation λ may be assumed to be a constant over the length of the pipe, particularly if the pipe is not ideally smooth, when the value of λ is larger than in the foregoing equations, but varies less with the Reynolds number[8].

With these approximations, the equation of motion becomes

$$\frac{A}{v}\,dr \times V\frac{dV}{dr} = -A\,dP - \frac{2\lambda A V^2}{vD}\,dr + \frac{A}{v}\omega^2 r\,dr \qquad . \quad . \quad (4a)$$

which simplifies to

$$v\,dP + V\,dV + \frac{2\lambda}{D}V^2 dr - \omega^2 r\,dr = 0. \qquad . \quad . \quad . \quad (4b)$$

The energy equation can be deduced at once by applying the First Law of Thermodynamics to the *open system*[4, 9] contained between the radii r and $r+dr$ as shown in Fig. 2, and remembering that the quantity of work $\omega^2 r\,dr$ enters the system. Thus

$$dh+V\,dV-\omega^2 r\,dr=0 \qquad . \quad . \quad . \quad . \quad (5)$$

where h denotes enthalpy. Introducing the velocity of sound a from the equation

$$h=\frac{a^2}{\gamma-1} \qquad . \quad . \quad . \quad . \quad . \quad . \quad (6)$$

we have

$$a\,da+\frac{\gamma-1}{2}V\,dV-\frac{\gamma-1}{2}\omega^2 r\,dr=0. \qquad . \quad . \quad . \quad (5a)$$

The energy equation integrates at once to

$$a_{01}{}^2=a^2+\frac{\gamma-1}{2}V^2-\frac{\gamma-1}{2}\omega^2 r^2. \qquad . \quad . \quad . \quad (5b)$$

Introducing the dimensionless ratios

$$\left.\begin{aligned} M&=V/a_{01}\\ x&=r/D\\ G^2&=\omega^2 D^2/a_{01}{}^2 \end{aligned}\right\} \qquad . \quad . \quad . \quad . \quad . \quad (7)$$

we have

$$\frac{a_{01}{}^2}{a^2}=1-\frac{\gamma-1}{2}M^2+\frac{\gamma-1}{2}G^2x^2. \qquad . \quad . \quad . \quad (5c)$$

In particular

$$\frac{a_{02}{}^2}{a_{01}{}^2}=1+\frac{\gamma-1}{2}G^2x_3{}^2. \qquad . \quad . \quad . \quad . \quad (5d)$$

The preceding equations are rather obvious extensions of the ordinary energy equation if it is noticed that the kinetic energy of a unit mass of gas rotating with an angular velocity ω on an arm r is $\frac{1}{2}\omega^2 r^2$.

It should be noted for further reference that the stagnation temperature, as well as the temperature in any section or in the second reservoir, can be calculated without difficulty, the stagnation temperature depending only on the initial stagnation temperature T_{01}, the radius r, and the angular velocity ω. They are independent of pressure or mass flow.

3. Integrable Form of the Fundamental Equation of the Problem

By eliminating pressure and specific volume from the basic equations (3), (4*b*) and (5*c*), we can derive an equation connecting the dimensionless velocity ratio M

with the dimensionless distance x, which is the fundamental differential equation of the problem. From the continuity equation (3)

$$v=\frac{V}{\psi} \quad . \quad . \quad . \quad . \quad . \quad . \quad . \quad (8)$$

so that with $$a^2=\gamma Pv=\frac{\gamma PV}{\psi},$$

we have, from equation (5*b*),

$$P=\left(\frac{a_{01}{}^2}{\gamma V}-\frac{\gamma-1}{2\gamma}V+\frac{\gamma-1}{2\gamma}\frac{\omega^2}{V}r^2\right)\psi \quad . \quad . \quad . \quad (9)$$

and $$\frac{dP}{dr}=\left[\frac{\gamma-1}{\gamma}\frac{\omega^2 r}{V}-\left(\frac{\gamma-1}{2\gamma}+\frac{a_{01}{}^2}{\gamma V^2}+\frac{\gamma-1}{2\gamma}\frac{\omega^2 r^2}{V^2}\right)\frac{dV}{dr}\right]\psi. \quad . \quad (9a)$$

Substituting v from (8) and dP/dr from (9*a*) into the equations of motion (4*b*) and introducing the abbreviations (7), we obtain finally

$$\frac{dM^2}{dx}=\frac{2M^2(2\lambda\gamma M^2-G^2x)}{1-\frac{\gamma+1}{2}M^2+\frac{\gamma-1}{2}G^2x^2}. \quad . \quad . \quad . \quad (10)$$

This is a non-linear first-order differential equation in M^2 which, as far as could be ascertained, cannot be integrated in close terms.

It can be verified that for $G^2=0$ it reduces to the well-known pipe equation[5].

The velocity distribution along the pipe depends on the properties of the gas expressed through the isentropic index γ, on the coefficient of friction λ, and on the parameter G, which includes the effect of the angular velocity ω, hydraulic diameter D, and initial velocity of sound a_{01}. Apart from that, the velocity distribution also depends on the value of the velocity in section "1," which is the initial value for the internal curve defined by equation (10). This initial value, in turn, depends on P_{01} and m', but P_{01} does not influence the velocity distribution directly.

4. Mach Number

Since equation (10) embraces only continuous solutions, it is necessary to analyse the variation of the Mach number M' along the tube and, in particular, to determine the locus of sonic sections, in order to determine the length of pipe over which shocks are likely to occur.

Starting with the definition of the Mach number

$$M'=\frac{V}{a}=\frac{V}{a_{01}}\frac{a_{01}}{a} \quad . \quad . \quad . \quad . \quad . \quad (11)$$

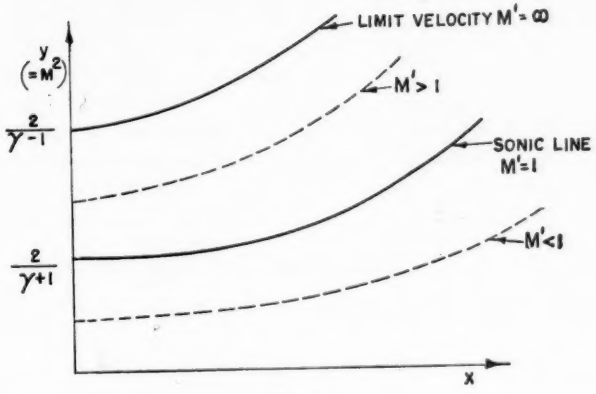

Fig. 3.

we substitute from equation (5*c*) so that

$$M'^2 = \frac{M^2}{1 - \frac{\gamma-1}{2}M^2 + \frac{\gamma-1}{2}G^2x^2} \quad . \quad . \quad . \quad . \quad . \quad (12)$$

and lines of constant Mach number in the x, y-plane are parabolas given by

$$y = \frac{\frac{1}{2}(\gamma-1)G^2M'^2}{\frac{1}{2}(\gamma-1)M'^2+1}x^2 + \frac{M'^2}{\frac{1}{2}(\gamma-1)M'^2+1} \quad . \quad . \quad . \quad (12a)$$

where

$$y = M^2. \quad . \quad . \quad . \quad . \quad . \quad . \quad . \quad (12b)$$

They all have vertical axes and are sketched in Fig. 3. For $\omega = 0 (G = 0)$ the parabolas become straight horizontal lines as expected. The sonic line $M' = 1$ is the parabola

$$y = \frac{\gamma-1}{\gamma+1}G^2x^2 + \frac{2}{\gamma+1}. \quad . \quad . \quad . \quad . \quad (12c)$$

It intersects the axis $x = 0$ at

$$y_0 = \frac{2}{\gamma+1}$$

which corresponds to a sonic entrance velocity to the rotating arm.

For $M' \longrightarrow \infty$ the parabola becomes

$$y = G^2x^2 + \frac{2}{\gamma-1}. \quad . \quad . \quad . \quad . \quad . \quad (12d)$$

which intersects the line $x=0$ at the terminal entrance velocity

$$y_\infty = \frac{2}{\gamma-1}.$$

The parabola (12*d*) sets the upper limit above which the equation (12*a*) has no physical meaning, and the parabola (12*c*) divides the quadrant into a subsonic and a supersonic region.

5. Singular Points of the Differential Equation (10)

Taking into account the convention (12*b*), we re-write equation (10) as

$$\frac{dy}{dx} = \frac{2\,y(my-G^2x)}{1-py+qG^2x^2} \quad . \quad . \quad . \quad . \quad . \quad . \quad (13)$$

where

$$\left.\begin{aligned} m &= 2\lambda\gamma \\ p &= \tfrac{1}{2}(\gamma+1) \\ q &= \tfrac{1}{2}(\gamma-1) \end{aligned}\right\} \quad . \quad . \quad . \quad . \quad . \quad . \quad . \quad (13a)$$

We shall also write it in the form

$$\frac{dy}{dx} = \frac{Y(x,y)}{X(x,y)} \quad . \quad . \quad . \quad . \quad . \quad . \quad . \quad (14)$$

where

$$\left.\begin{aligned} X(x,y) &= 1-py+qG^2x^2 \\ Y(x,y) &= 2y(my-G^2x) \end{aligned}\right\} \quad . \quad . \quad . \quad . \quad . \quad (14a)$$

The vector (X, Y) is vertical on the line $X(x,y)=0$, *i.e.* on the parabola

$$y = \frac{q}{p}G^2x^2 + \frac{1}{p} \quad . \quad . \quad . \quad . \quad . \quad . \quad (15)$$

which is identical with the sonic line (12*c*), indicating that the integral curves have vertical tangents on crossing the sonic line, except at singular points. Since the vector (X, Y) turns, the integral curves have maxima or minima in x on it, but no points of inflection.

The vector (X, Y) is horizontal, indicating a maximum or minimum in y for the same reasons as before, on the straight line

$$y = \frac{G^2}{m}x \quad . \quad . \quad . \quad . \quad . \quad . \quad (15a)$$

on which $Y(x,y)=0$, as well as on the axis of abscissae $y=0$.

The intersections of the straight line (15*a*) with the parabola (15), if they exist, are *singular points* of equation (13). In view of the identity of equations (15) and (12*c*), singular points always coincide with sonic sections in the interior of the pipe. At singular points the theorems of existence and uniqueness of integral curves do not apply, and the usual methods of numerical integration[10, 11, 12] break down. On the other hand, a continuous passage across the sonic line is possible only through singular points; hence the latter play a crucial role in the determination of the pattern of integral curves. Their discussion must, therefore, precede any programme of numerical computation.

The abscissae of the singular points which satisfy (15) and (15*a*) simultaneously must satisfy the equation

$$x^2 - \frac{p}{qm}x + \frac{1}{qG^2} = 0 \qquad . \quad . \quad . \quad . \quad (16)$$

which has either no real roots, one double real root, or two real roots, depending on the sign of the discriminant

$$\Delta = \frac{p^2}{q^2m^2} - \frac{4}{qG^2}. \qquad . \quad . \quad . \quad . \quad (17)$$

Putting

$$G_{\text{crit}} = \frac{2mq^{\frac{1}{2}}}{p} = \frac{4\lambda\gamma\,[2\,(\gamma-1)]^{\frac{1}{2}}}{\gamma+1} \qquad . \quad . \quad . \quad . \quad (18)$$

we see that if $$G < G_{\text{crit}} \qquad . \quad . \quad . \quad . \quad . \quad (18a)$$

there are no singular points. Putting

$$\omega_{\text{crit}} = \frac{a_{01}}{D}G_{\text{crit}} = \frac{a_{01}}{D}\frac{4\lambda\gamma\,[2\,(\gamma-1)]^{\frac{1}{2}}}{\gamma+1} \qquad . \quad . \quad . \quad . \quad (19)$$

we see that if the angular velocity is smaller than the critical

$$\omega < \omega_{\text{crit}} \qquad . \quad . \quad . \quad . \quad . \quad (19a)$$

there are no singular points. Similarly for

$$G = G_{\text{crit}}, \quad \omega = \omega_{\text{crit}} \qquad . \quad . \quad . \quad . \quad (19b)$$

there is one double singular point for which x^* and y^* are positive, and for

$$G > G_{\text{crit}}, \quad \omega > \omega_{\text{crit}} \qquad . \quad . \quad . \quad . \quad (19c)$$

there are two distinct singular points, both in the first quadrant.

6. Asymptotic Behaviour of the Integral Curves of Equation (13)

Before a detailed discussion of the three families of solutions of equation (13), the asymptotic behaviour of the integral curves is examined, as this is independent of the particular value of the angular velocity. The best way of obtaining this information seems to be to transform equation (13) by inversion, substituting

$$\left.\begin{aligned} x &= \frac{\xi}{\xi^2+\eta^2} \\ y &= \frac{\eta}{\xi^2+\eta^2} \end{aligned}\right\} \quad . \quad . \quad . \quad . \quad . \quad . \quad (20)$$

as a result of which straight lines passing through the origin are transformed into themselves.

Equation (13) becomes

$$\frac{d\eta}{d\xi} = \frac{2\xi\eta\,[(\xi^2+\eta^2)^2 - p\eta\,(\xi^2+\eta^2) + qG^2\xi^2] + 2\eta\,(\eta^2-\xi^2)\,(m\eta - G^2\xi)}{(\xi^2-\eta^2)\,[(\xi^2+\eta^2)^2 - p\eta\,(\xi^2+\eta^2) + qG^2\xi^2] + 4\xi\eta^2\,(m\eta - G^2\xi)} \quad . \quad (21)$$

and the point at infinity is transformed into the origin, becoming at the same time a singular point of the new equation (21). Here the numerator and the denominator contain no terms of degree lower than 4. Denoting by $X_4(\xi,\eta)$ and $Y_4(\xi,\eta)$ the sums of terms of degree 4 in ξ,η in the expressions for $X(\xi,\eta)$ and $Y(\xi,\eta)$ respectively, we have

$$\left.\begin{aligned} X_4(\xi,\eta) &= qG^2\xi^2\,(\xi^2-\eta^2) + 4\xi\eta^2\,(m\eta - G^2\xi) \\ Y_4(\xi,\eta) &= 2qG^2\xi^3\eta + 2\eta\,(\eta^2-\xi^2)\,(m\eta - G^2\xi) \end{aligned}\right\} \quad . \quad . \quad (21a)$$

Hence the characteristic equation

$$\xi Y_4 - \eta X_4 = 0$$

becomes

$$\xi\eta\,(\xi^2+\eta^2)\,[(q+2)G^2\xi - 2m\eta] = 0 \quad . \quad . \quad . \quad . \quad (22)$$

so that there are the following three characteristic straight lines

$$(i) \qquad \xi = 0$$

$$(ii) \qquad \eta = 0$$

$$(iii) \qquad (q+2)G^2\xi - 2m\eta = 0$$

each of which is regular[14] and corresponds to a factor occurring only once in the characteristic equation (22). On the other hand, it is easy to verify that on the characteristic straight lines (*ii*) and (*iii*), we have $X_4(\xi,\eta) > 0$, and that in the

neighbourhood of line (*i*), $X_4(\xi, \eta) > 0$ when ξ and η are positive. Therefore, if we limit ourselves to the first quadrant, the expression

$$\frac{Y_4(\xi, \eta)}{X_4(\xi, \eta)} - \frac{\eta}{\xi} = \frac{\eta(\xi^2+\eta^2)[(q+2)G^2\xi - 2m\eta]}{\xi X_4(\xi, \eta)} \quad . \quad . \quad . \quad (22a)$$

is of the same sign, in the neighbourhood of the characteristic straight lines, as the left-hand side of (*iii*), and therefore positive above (*ii*) and below (*iii*) and negative above (*iii*) and near to (*i*). This shows[14] that there are exactly two integral curves

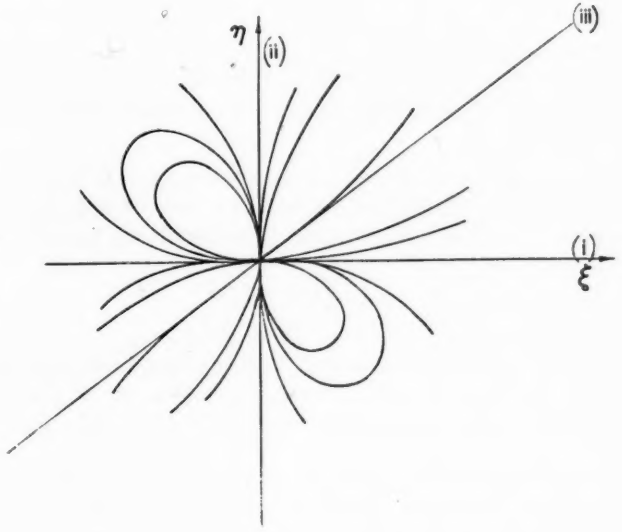

Fig. 4.

reaching the singular point tangentially to (*iii*), namely one from each side, whereas there are infinitely many integral curves reaching the origin from each side tangentially to (*i*) or (*ii*) (Fig. 4).

In view of the symmetry of the vector field represented by $X_4(\xi, \eta)$ and $Y_4(\xi, \eta)$, the shape of the integral curves of equation (2) in the neighbourhood of the point $\xi = \eta = 0$ can therefore be described as follows[14]. The first and the third quadrants are each divided by the only integral curves reaching the point $\xi = \eta = 0$ tangentially to (*iii*) into two parabolic sectors, swept by integral curves reaching the singular point tangentially to $\eta = 0$ and to $\xi = 0$ respectively, whereas the second and fourth quadrants are occupied by two elliptic sectors, swept by curves forming loops which start and finish at the singular point tangentially to the axes of co-ordinates.

Bearing in mind that $$\frac{y}{x}=\frac{\eta}{\xi}$$

it is seen that a tangent at the origin $\eta=\xi=0$ to an integral curve corresponds to an asymptotic *direction* of the image of this curve in the x, y-plane, the two slopes being equal. Reverting to the differential equation (13), *i.e.* in terms of the x, y-plane, and again limiting attention to the first quadrant only (the other quadrants having no physical significance), the previous results can be restated as follows:—

(*a*) There is exactly one integral curve with an asymptotic direction of slope

$$\lambda_\infty=\frac{(q+2)G^2}{2m}=\frac{(\gamma+1)G^2}{8\lambda\gamma}. \qquad (23)$$

It forms the boundary between the locus of the integral curves whose asymptotic direction is that of the x-axis and the locus of the integral curves whose asymptotic direction is the y-axis. This is true at least if we disregard a sufficiently large circle centred at the origin.

(*b*) The integral curves whose asymptotic direction is that of the axis of abscissae admit as an asymptote precisely this axis, which is itself an integral curve of equation (13). Indeed equation (13) can be written in the form

$$\frac{dy}{dx}=\frac{y}{x}\,\frac{2(my-G^2x)}{x^{-1}-pyx^{-1}+qG^2x} \qquad (24)$$

but if $x\longrightarrow\infty$ and $y/x\longrightarrow 0$, the second fraction on the right-hand side tends to $-2/q$. Hence, choosing an arbitrary positive number $k^2<2/q$ on any of the integral curves under consideration, it is found that for sufficiently large values of x,

$$\frac{dy}{dx}<-k^2\frac{y}{x}$$

so that $$y<Cx^{-k^2}$$

which completes the proof.

(*c*) Writing equation (13) in the form

$$\frac{dx}{dy}=\frac{X}{Y} \qquad (25)$$

it can be proved that its integral curves, admitting the y-axis as an asymptotic direction, cross from the first quadrant into the second as $y\longrightarrow\infty$.

It is first proved that on each of these integral curves x has a finite upper bound.

Assuming $$0<\varepsilon<m/G^2,$$

consider only points satisfying

$$0\leqslant x<\varepsilon y \quad\text{with}\quad y>1/p.$$

Then $$X(x, y) = 1 - py + pG^2x^2 < qG^2x^2$$

and $$Y(x, y) = 2y(my - G^2x) > 0,$$

so that $$\frac{dx}{dy} < \frac{qG^2x^2}{2(m - G^2\varepsilon)y^2}. \quad . \quad . \quad . \quad . \quad (25a)$$

In other terms if $$\nu = \frac{qG^2}{2(m - G^2\varepsilon)}. \quad . \quad . \quad . \quad . \quad . \quad (25b)$$

the integral curves of (25) satisfy

$$\frac{dx}{dy} < \nu \frac{x^2}{y^2} \quad . \quad . \quad . \quad . \quad . \quad . \quad (25c)$$

in the domain under consideration. Integrating the inequality (25*c*) gives

$$\frac{1}{x} > \frac{\nu}{y} + C \quad . \quad . \quad . \quad . \quad . \quad (25d)$$

where C is a constant depending on the particular integral curve under consideration. But from (25*d*) it follows that

$$x < \frac{1}{C}.$$

Now considering any particular integral curve which admits the direction of the y-axis as asymptotic, only the band

$$0 \leqslant x \leqslant b$$

need be considered, where b is so chosen equal to, or greater than, the upper bound of the abscissae on this particular integral curve. Moreover, being concerned with large values of y, y can be assumed to be larger than the larger of the two numbers

$$\frac{1 + qG^2b^2}{p} \quad \text{and} \quad \frac{G^2b}{m}.$$

Then $$0 < 2y(my - G^2x) \leqslant 2my^2$$

and $$1 - py + qG^2x^2 < 1 + qG^2b^2 - py < 0,$$

and therefore $$\frac{1 - py + qG^2x^2}{2y(my - G^2x)} < \frac{1 + qG^2b^2 - py}{2my^2}.$$

Hence[13, 15] comparing the solution of (25) determined by any initial point in the band $0 \leqslant x \leqslant b$ with the solution of

$$\frac{dx}{dy} = \frac{1 + qG^2b^2 - py}{2my^2} \quad . \quad . \quad . \quad . \quad . \quad (26)$$

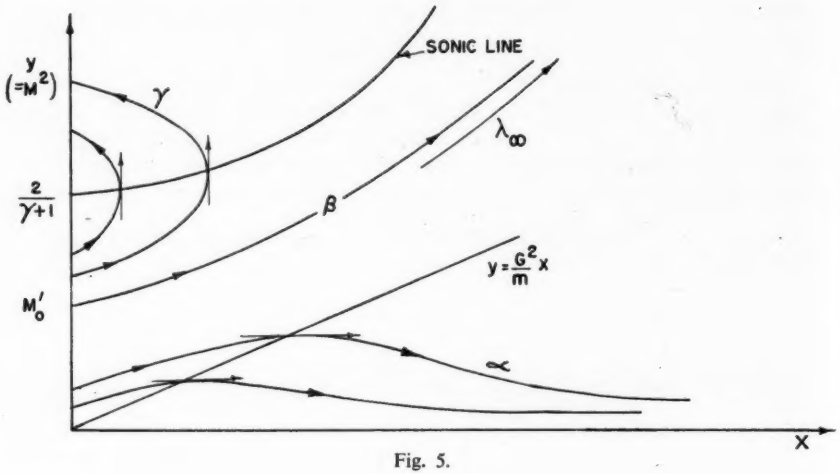

Fig. 5.

determined by the same initial condition, it is found that for any given value of y exceeding the ordinate of the initial point, the value of the solution of (26) is larger than that of the solution of (25), so long, at any rate, as x remains positive. But the solution of (26) is

$$x = -\frac{1+qG^2b^2}{2my} - \frac{p}{2m}\log_e y + C \quad . \quad . \quad . \quad . \quad (26a)$$

where C is the constant of integration. Evidently for any value of C, $x \longrightarrow -\infty$ as $y \longrightarrow +\infty$ and, in particular, x becomes negative for sufficiently large values of y. This applies to the solution of (25) all the more, and so the proof is complete.

7. The Case of Small Angular Velocities

When the angular velocity is less than the critical value (19) there are no singular points and the pattern of the integral curves can be sketched without much further analysis. This case is shown in Fig. 5, from which it is seen that there are three types of integral curves.

For values of the inlet velocity which are smaller than M_0' the curves denoted by α in the sketch have a maximum on the line (15a) and decrease asymptotically to the x-axis, as proved in Section 6.

For values of the inlet velocity which are greater than M_0' the curves, denoted by γ, cross the sonic line with a vertical tangent, and cross the y-axis, in accordance with Section 6. Evidently such high inlet velocities are admissible only if the length of the rotating arm does not exceed a given maximum which, for a given value of

G, depends only on the inlet velocity. An analogous phenomenon exists with stationary channels of constant cross-sectional area[6, 7] and is commonly referred to as choking.

The areas swept by these two types of integral curves are separated from each other by a border-line curve, denoted by β, which tends to infinity with an asymptotic direction λ_∞ defined by equation (23), and intersects neither the sonic line nor the line of maxima.

Finally it might be noted that the entrance velocity to the pipe area can never become sonic, although it may be supersonic, and that at these low angular velocities sonic flow may occur at the pipe exit only.

8. The Case of Large Angular Velocities

Leaving aside, for the time being, the case when the angular velocity is equal to the critical value (19), the case when it exceeds it is now discussed. There are then two singular points, which will be denoted by $P_1(x_1^*, y_1^*)$ and $P_2(x_2^*, y_2^*)$, assuming $x_1^* < x_2^*$ (Fig. 6). Their co-ordinates are given by

$$\left.\begin{aligned} x_{1,2}^* &= \frac{p}{2mq} \mp \frac{(p^2G^2 - 4m^2q)^{\frac{1}{2}}}{2mqG} \\ y_{1,2}^* &= \frac{pG^2}{2m^2q} \mp \frac{G(p^2G^2 - 4m^2q)^{\frac{1}{2}}}{2m^2q} \end{aligned}\right\} \quad . \quad . \quad . \quad . \quad . \quad (27)$$

Transferring the origin to any of the two singular points and substituting

$$\left.\begin{aligned} x &= x^* + \bar{x} \\ y &= y^* + \bar{y} \end{aligned}\right\} \quad . \quad . \quad . \quad . \quad . \quad (27a)$$

the linear parts of X and Y in the neighbourhood of the singular point can be expressed as

$$\left.\begin{aligned} X_1(\bar{x}, \bar{y}) &= 2qG^2x^*\bar{x} - p\bar{y} \\ Y_1(\bar{x}, \bar{y}) &= -2G^2y^*\bar{x} + 2my^*\bar{y} \end{aligned}\right\} \quad . \quad . \quad . \quad . \quad . \quad (27b)$$

Hence, at the singular points, the Jacobian is

$$J = 2G^2y^*(2mqx^* - p) \quad . \quad . \quad . \quad . \quad . \quad (28)$$

The characteristic equation, $\bar{x}Y_1 - \bar{y}X_1 = 0$, becomes

$$p\bar{y}^2 + 2(my^* - qG^2x^*)\bar{x}\bar{y} - 2G^2y^*\bar{x}^2 = 0.$$

or, introducing the slope λ,

$$p\lambda^2 + 2(1-q)my^*\lambda - 2G^2y^* = 0. \quad . \quad . \quad . \quad . \quad . \quad (29)$$

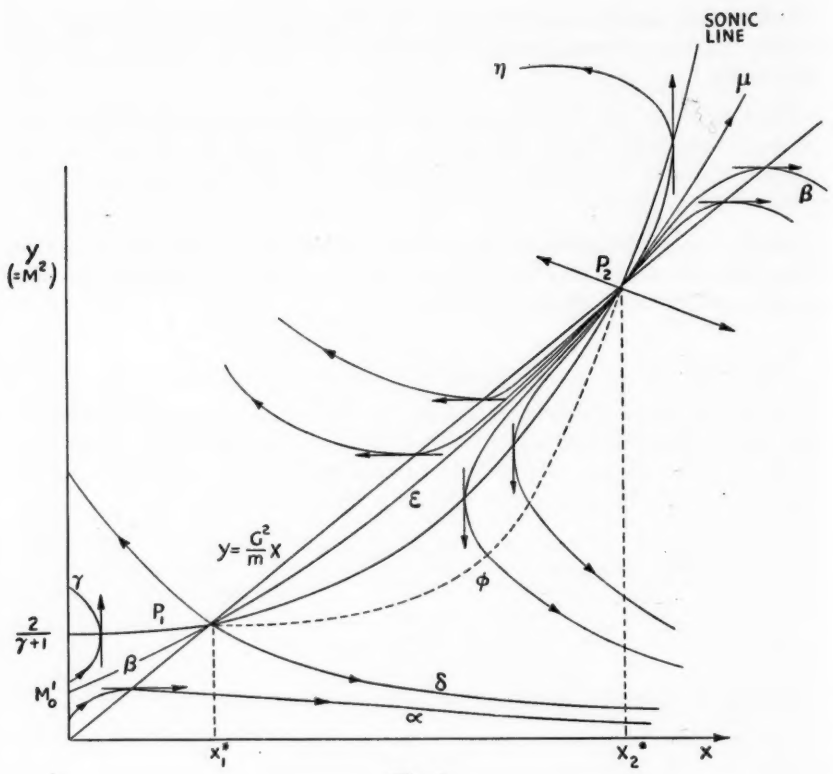

Fig. 6.

At each of the two singular points there are, therefore, two real characteristic directions with slopes of opposite signs. On the other hand, by comparing equation (28) with equations (27), it is easy to see that the Jacobian (28) is negative at P_1 and positive at P_2. Therefore P_1 is a saddle point and P_2 is a nodal point.

From what has been said before, it can easily be deduced that of the two integral curves starting from P_1 with negative slopes, one crosses back into the second quadrant, and the other, denoted by δ in Fig. 6, tends asymptotically to the x-axis. The integral curve starting from P_1 in the direction of the decreasing abscissae with a positive slope intersects the y-axis at a point M_0' of positive ordinate; it is denoted by β in Fig. 6. Curves starting from points of the y-axis situated below M_0' have points of maximum ordinate on the line (15a), after which their ordinate steadily diminishes, tending to zero in the limit; one of these curves is denoted by α in Fig. 6. On the other hand, integral curves like γ in Fig. 6, starting from points on the y-axis situated above M_0' cross the sonic line, turning there and subsequently intersecting again the axis of ordinates.

There remains to be considered the fourth integral curve originating at P_1, denoted by ε in Fig. 6, namely the curve which leaves this point with a positive slope in the direction of the increasing abscissae. Since, to the right of P_1, the slopes of integral curves at points situated either below the sonic line (15) or above the line (15*a*) are negative, the curve must enter the segment cut off from the parabola (15) by the line (15*a*). But above the parabola (15) $X<0$, so that if we proceed on ε away from P_1, we do so against the vector (X, Y). On the other hand the vector (X, Y) points away from the segment, both on the rectilinear and on the curvilinear part of its boundary, except at P_1 and P_2, where it vanishes. Therefore ε, which cannot have a vertical tangent inside the segment of parabola and which cannot leave it through any other point, is bound to reach P_2. It clearly does so with a positive slope.

Since the same reasoning applies to any other integral curve passing through the inside of the segment of parabola just mentioned, there are infinitely many integral curves arriving at P_2 tangentially to the characteristic line of positive slope, and therefore, according to the general theory of nodal points[16, 17], there is only one integral curve on each side arriving at P_2 tangentially to the characteristic line of negative slope.

Of the infinitely many integral curves tangent to ε at P_2, those which are above ε connect P_2 with the y-axis, whereas those which are below intersect the sonic parabola (15), turn there and are asymptotic to the x-axis. Of the two integral curves arriving at P_2 with negative slopes, again one connects P_2 with the y-axis and the other is asymptotic to the x-axis.

Finally, among the infinitely many integral curves leaving P_2 in the direction of the increasing abscissae with a tangent of positive slope, there must be the line whose asymptotic direction is defined by equation (23); the integral curves above it cross the sonic line and turn back, eventually crossing the y-axis, whereas the integral curves below are asymptotic to the axis of abscissae.

Thus the pattern shown in Fig. 6 can be completed.

The essential difference between the previous subcritical and the present supercritical pattern lies in the fact that at P_1 sonic velocity can be reached, and afterwards exceeded, *inside* the rotating tube.

The types of solution α and γ are identical with the corresponding solutions in the previous case. However, if at $r=0$, $M=M_0'$, the flow will reach $M'=1$ at x_1^*. From this point onwards, as in a convergent-divergent nozzle, it may further proceed either along δ into the subsonic region, or along ε into the supersonic region, where it is liable to shock formation. If the pipe is ended between x_1^* and x_2^* there exist two "correct" values of y at the exit, corresponding to two "correct" values for the back-pressure, for which the flow is continuous, becoming subsonic in one case, and supersonic in the other, in complete analogy with a de Laval nozzle.

If the pipe is continued beyond x_2^*, the solution which started with M_0' will become subsonic in a continuous way at x_2^*, from which it may now proceed along

any of the integral curves which emerge from P_2, either along a curve η, when it follows it until sonic velocity is again reached at exit, the Mach number having passed through a maximum, or along a curve of type θ which exhibits a maximum in y and continues asymptotically towards the x-axis. Finally it may proceed along the boundary curve μ, whose asymptotic direction is given by equation (23).

Here, however, there is no limiting length of pipe in the case of curves of type η, as they all emerge from P_2 and everything depends on the conditions at exit.

Since the net of parabolas of constant Mach number has been drawn previously, the drawing can be supplemented with a curve, denoted ϕ in Fig. 6, which indicates the Mach number after a normal shock along the supersonic solution connecting P_1 and P_2, and that enables us to include the study of shock formation.

9. Critical Angular Velocity

When the angular velocity ω has exactly the critical value (19), the two singular points coalesce. The resulting pattern of flow is simply the limit of that which corresponds to large angular velocities when the distance between the two singular points tends to zero; it is shown in Fig. 7. It will be appreciated that this is also the limit to which the pattern of flow for small angular velocities tends when ω tends, from below, to the critical value; indeed, as the sonic parabola (15) and the line (15*a*) come near to each other, the integral curves passing through the gap between the two diverge more and more violently.

In the case of the critical angular velocity, the singular point, whose co-ordinates are

$$\left.\begin{aligned} x^* &= \frac{p}{2mq} \\ y^* &= \frac{pG^2}{2m^2q} \end{aligned}\right\} \quad . \quad . \quad . \quad . \quad . \quad . \quad (30)$$

(*see* equation (27)) has a vanishing Jacobian, equation (28), so that it is not one of the types discussed by Poincaré[16] or Perron[17] but it can be studied directly, either by a rather complicated method of change of variables transforming it into one of the types discussed by Dulac ("point exceptionel")[18] or, more simply and directly by Frommer's method[14]. Substituting the values (30) of x^* and y^* in the characteristic equation (29), the two values of λ can be expressed as

$$\lambda_1 = -\frac{G^2}{mq}, \quad \lambda_2 = \frac{G^2}{m}, \quad . \quad . \quad . \quad . \quad . \quad (31)$$

of which the first corresponds to a regular characteristic direction, and the second to a singular one. It is easy to find then that there is exactly one integral curve on each side approaching the singular point with a slope equal to λ_1, and also exactly one doing so, from the left-hand side, with a slope equal to λ_2, but that there are

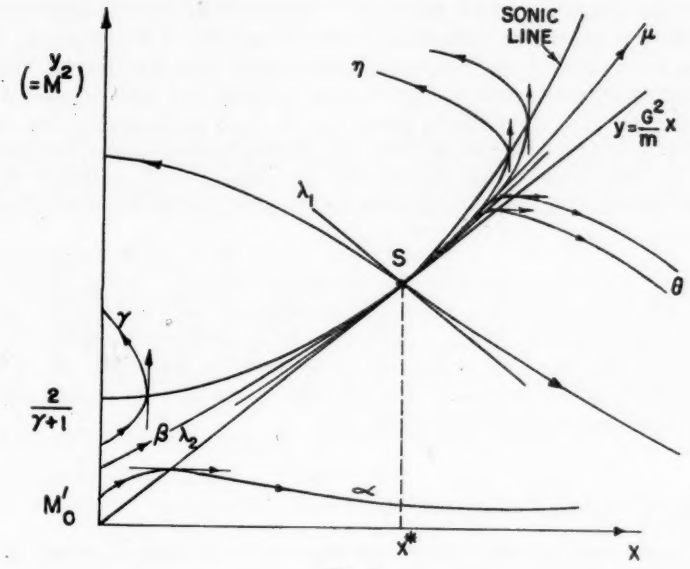

Fig. 7.

infinitely many integral curves leaving in the direction of the increasing abscissae with a slope equal to λ_2; among the latter integral curves, one (μ in Fig. 7) tends to infinity with an asymptotic direction defined by equation (23) and separates the area swept by integral curves crossing back into the second quadrant from that which is swept by integral curves asymptotic to the x-axis.

The interpretation of the curves in Fig. 7 should now present no difficulty.

10. Numerical or Graphical Integration

Since no expression giving the integrals of equation (10) in closed terms is available, it is necessary to resort to numerical or graphical methods[10, 11, 12, 13]. In view of the complexity of the right-hand side of equation (10), it seems that the most practical course is to adopt the simplest possible method, which is that of step-by-step integration; however, to obtain sufficiently accurate results, relatively small steps must be selected.

It is also possible to use the graphical method of isoclines; in this connection, it may be worth noting that these are conics given by the equation

$$kqG^2x^2+2G^2xy-2my^2-kpy+k=0 \quad . \quad . \quad . \quad (32)$$

where k is the slope of the integral curves.

As far as the neighbourhood of the singular points is concerned, it is clear that if there is only one integral curve reaching a singular point with a given slope, its

construction should start from the singular point; the error committed by assimilating the first arc of the curve to a rectilinear segment is minimised by the fact that, in going away from a singular point along such an integral curve, the neighbouring integral curves do not diverge violently and even actually converge if the singular point is a saddle point. In the case of integral curves reaching singular points tangentially to infinitely many other integral curves, the integration should, obviously, be carried out towards the singular point, and here again no difficulty should be experienced, as both the end point and the slope at it are known in advance.

If it is desired to determine the border-line curve, β in Fig. 5, $\beta-\varepsilon-\mu$ in Fig. 6, and $\beta-\mu$ in Fig. 7, it is possible to begin the calculation in the plane ξ, η considered in Section 6. The line starts there at the origin with a known slope (23) so that it can be traced, *e.g.* to the unit circle centred at the origin. Since the unit circle is transformed into itself, the calculation can now be continued in the x, y-plane starting from the unit circle there.

11. Approximate Solutions for Small Velocities

A useful approximate solution of equation (13) which is valid for small velocities, M, can be obtained by noting that if y is small, it changes very slowly, while the relative error in the denominator of the right-hand side of equation (13) due to an error in y is comparatively small. It is, therefore, natural to substitute a constant value for y *in the denominator only*. It will be appreciated that the approximation improves with increasing values of x, and that it does not change the shape of the integral curves, the locus of the maxima of their ordinates being still the line (15*a*).

Substituting
$$s=1-py \qquad . \quad . \quad . \quad . \quad . \quad (33)$$

the approximate form of equation (13) can be written

$$\frac{dy}{dx}=\frac{2y(my-G^2x)}{s+qG^2x^2}. \qquad . \quad . \quad . \quad (33a)$$

This is an equation of Bernoulli's type.

Assuming
$$\gamma=1{\cdot}4, \quad q=1/5,$$

its solution can be expressed by elementary functions in the form

$$\frac{1}{y}=\frac{mx}{s}\left[\frac{1}{5}+\frac{9}{40}\frac{u}{s}+\frac{21}{80}\frac{u^2}{s^2}+\frac{21}{64}\frac{u^3}{s^3}+\frac{63}{128}\frac{u^4}{s^4}\right]+$$
$$+\frac{63\sqrt{5}}{128}\frac{mu^5}{s^{11/2}G}\tan^{-1}\frac{Gx}{(5s)^{1/2}}+\frac{u^5}{y_1s^5} \qquad . \quad . \quad . \quad (33b)$$

with y_1 denoting the value of y at $x=0$, and where

$$u=s+\frac{1}{5}G^2x^2. \quad . \quad . \quad . \quad . \quad . \quad (33c)$$

The error can easily be estimated by noting that, by making s smaller than the actual values of $1-py$, the integral curves can be made steeper than the exact solution, whereas by taking s bigger than $1-py$ (*e.g.* $s=1$), they can be made flatter.

12. Determination of Initial Conditions

(*a*) In the *design problem* it is necessary to determine the throat area A^* of the driving nozzle for a given state "01" and given mass flow m' and angular velocity ω. In this case the integration can follow from section "1" to section "2," subject to obvious limitations which arise from the flow patterns discussed previously. This presupposes that M_1 is known, so that it is useful to deduce a direct relationship between mass flow m' and entrance velocity M_1.

The mass flow in section "1" is given by

$$m'=A\rho_1V_1=A\,(\rho_1/\rho_{01})(V_1/a_{01})\rho_{01}a_{01}.$$

From the condition of isentropic flow through the entrance nozzle

$$\frac{\rho_1}{\rho_{01}}=\left(\frac{h_1}{h_{01}}\right)^{\frac{1}{\gamma-1}},$$

and from the energy equation

$$V=\left[2h_{01}\left(1-\frac{h_1}{h_{01}}\right)\right]^{\frac{1}{2}},$$

neglecting the small value of x_1. Introducing M from equation (7) gives

$$m'=AM_1\left(1-\frac{\gamma-1}{2}M_1^2\right)^{\frac{1}{\gamma-1}}. \quad . \quad . \quad . \quad . \quad (34)$$

where a_{01} was substituted for h_{01} from equation (6). This can be shortened to

$$m'=A\Omega_1\rho_{01}a_{01}$$

$$=A\gamma\Omega_1P_{01}/a_{01} \quad . \quad . \quad . \quad . \quad . \quad (34a)$$

with

$$\Omega=M\left(1-\frac{\gamma-1}{2}M^2\right)^{\frac{1}{\gamma-1}}. \quad . \quad . \quad . \quad . \quad (34b)$$

The functions $\Omega(M)$ and $\gamma\Omega(M)$ were calculated for air with $\gamma=1{\cdot}400$. They are given in Table I and Fig. 8.

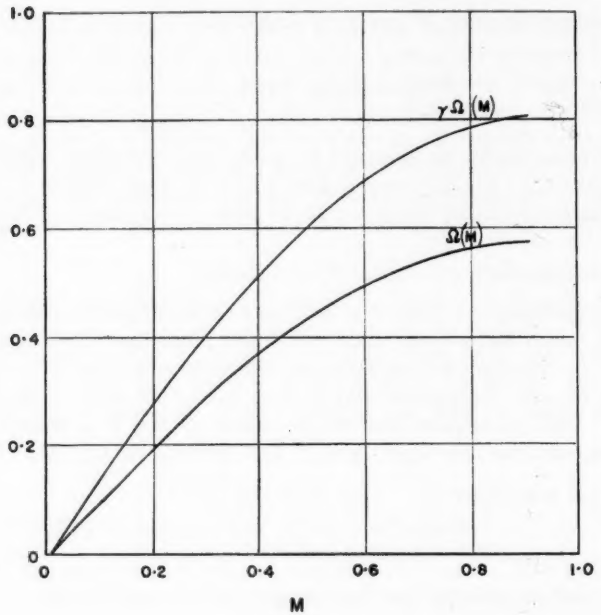

Fig. 8.

For small values of M the functions are nearly linear and in the range of values $0{\cdot}185 \leqslant M \leqslant 0{\cdot}325$ they can be approximated by

$$\left.\begin{aligned} \Omega &= 0{\cdot}9066\,M + 0{\cdot}0147 \\ \gamma\Omega &= 1{\cdot}2692\,M + 0{\cdot}0206 \end{aligned}\right\} \quad . \quad . \quad . \quad . \quad . \quad . \quad (34c)$$

with an error not exceeding 0·4 per cent. The straight lines (34*c*) give exact values for $M = 0{\cdot}2$ and $M = 0{\cdot}3$.

In the *performance problem* the cross-sectional area A^* of the driving nozzle is given and it is necessary to determine the state "01" for a given mass flow m', or to determine the mass flow for a given initial state. In this case it is preferable to perform the integration from section "2" to section "1." When T_{01} (or a_{01}) is given, T_{02} (or a_{02}) can be calculated without integration, directly from the energy equation (5*d*). The mass flow through area A^* can be represented by†

$$m' = A^*(2P_{02}\rho_{02})^{\frac{1}{2}}\left(\frac{P_3}{P_{02}}\right)^{\frac{1}{\gamma}}\left\{\frac{\gamma}{\gamma-1}\left[1-\left(\frac{P_3}{P_{02}}\right)^{\frac{\gamma-1}{\gamma}}\right]\right\}^{\frac{1}{2}}.$$

Eliminating ρ_{02} with the aid of the equation of state gives

$$m' = A^*\Psi\,P_a/a_{02} \quad . \quad . \quad . \quad . \quad . \quad (35)$$

† *See* equations (304) and (304*a*) on p. 336 in Ref. 9.

TABLE I

The functions $\Omega(M)$ and $\gamma\Omega(M)$ from equation (34*b*) with $\gamma = 1{\cdot}400$

M	Ω	$\gamma\Omega$
0·0	0·0000	0·0000
0·1	0·0995	0·1393
0·2	0·1960	0·2744
0·3	0·2867	0·4014
0·4	0·3688	0·5163
0·5	0·4398	0·6158
0·6	0·4978	0·6969
0·7	0·5409	0·7573
0·8	0·5680	0·7953
0·9	0·5787	0·8100
0·9129	0·5786	0·8102

TABLE II

The function $\Psi(\tilde{\omega})$ from equations (35*b*) and (35*c*) for air with $\gamma = 1{\cdot}400$

$\tilde{\omega}$	Ψ	$1/\tilde{\omega}$
1·000	0·0000	1·000
1·101	0·5306	0·908
1·205	0·7519	0·830
1·299	0·9050	0·770
1·399	1·0419	0·715
1·504	1·1669	0·665
1·600	1·2692	0·625
1·695	1·3617	0·590
1·802	1·4577	0·555
1·887	1·5288	0·530
1·8929	1·5336	0·5283
2·000	1·6204	0·500
4·000	3·2408	0·250

where
$$\Psi = \gamma\left(\frac{P_{02}}{P_a}\right)\left(\frac{P_3}{P_{02}}\right)^{\frac{1}{\gamma}}\left\{\frac{2}{\gamma-1}\left[1-\left(\frac{P_3}{P_{02}}\right)^{\frac{\gamma-1}{\gamma}}\right]\right\}^{\frac{1}{2}} \quad . \quad . \quad (35a)$$

and where P_a is the external, atmospheric pressure. When the overall pressure ratio for the driving nozzle is subcritical, $P_3 = P_a$,

so that
$$\Psi = \gamma\tilde{\omega}^{-\frac{\gamma-1}{\gamma}}\left[\frac{2}{\gamma-1}\left(1-\tilde{\omega}^{-\frac{\gamma-1}{\gamma}}\right)\right]^{\frac{1}{2}} \quad . \quad . \quad . \quad . \quad (35b)$$

with
$$\tilde{\omega} = P_{02}/P_a. \quad . \quad . \quad . \quad . \quad . \quad (35c)$$

When, however, the flow at A^* is sonic, the ratio P_3/P_{02} has the critical value, and equation (35*a*) becomes

$$\Psi = \gamma\left(\frac{2}{\gamma+1}\right)^{\frac{1}{2}\cdot\frac{\gamma+1}{\gamma-1}}$$

$$= 0{\cdot}81019\,\tilde{\omega} \quad . \quad . \quad . \quad . \quad . \quad (35d)$$

with $\gamma = 1{\cdot}400$.

The function $\Psi(\tilde{\omega})$ appearing in equation (35) is seen to depend only on the overall pressure ratio. It has been calculated for $\gamma = 1{\cdot}400$ and is reproduced in graphical form in Fig. 9 and tabulated as Table II. Evidently equation (35) is only another form of equation (34*a*).

If, now, m' is given as a fraction of the normal mass flow, equation (35) permits calculation of Ψ from which the value of P_{02} can be deduced. Thus we know P_{02}, T_{02} and a_{02}, which permits us to calculate M^2 with the aid of equation (35*a*) and to proceed with the integration. It is necessary to remember to replace, in equation

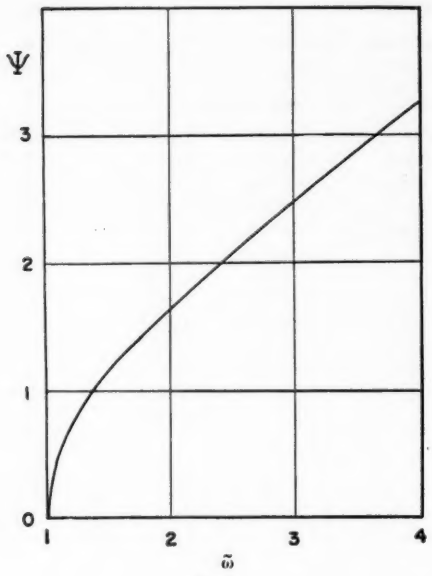

Fig. 9.

(34*a*), P_{01} and a_{01} by P_{02} and a_{02} respectively, if we neglect the difference between x_2 and x_3.

The rest of the calculation should now be obvious.

13. The Pressure Distribution

The pressure at any section of the duct is given by

$$P=\frac{\psi a_{01}}{\gamma M}\left(1-\frac{\gamma-1}{2}M^2+\frac{\gamma-1}{2}G^2x^2\right) . \quad . \quad . \quad . \quad (36)$$

which follows from equation (9). The last term in the bracket has been already tabulated when performing the numerical integration, so that the evaluation of the pressure distribution presents little difficulty. With the aid of equation (34*a*), equation (36) can be re-written in the following useful form:—

$$\frac{P}{P_{01}}=\Omega(M_1)\frac{1-\frac{\gamma-1}{2}M^2+\frac{\gamma-1}{2}G^2x^2}{M} . \quad . \quad . \quad . \quad (36a)$$

which gives the variation of the pressure ratio with x, in terms of the initial value M_1 and the local value M.

It should be noted that a maximum in M does not necessarily imply a minimum in P, and that the pressure variation along the pipe depends on the inlet conditions.

Acknowledgments

The problem was suggested to the authors by J. Tustanowski of Percival Aircraft Ltd. The authors are indebted to this firm for their consent to publish this paper. Thanks are also due to Z. Janczur, J. Moszynski and J. A. Owczarek for their help with the calculation of tables and with the checking of formulae, as well as to H. Zygalski for his efforts to solve equation (10) explicitly.

References

1. Doblhoff, F. L. W. (1950). The Helicopter Pressure Jet. *Aeronautical Engineering Review*, Vol. 9, pp. 36-42, 1950.
2. Johnson, J. A. and Eustis, R. H. (1951). An Analysis of Helicopter Propulsion Systems. Trans. A.S.M.E., Vol. 73, pp. 519-528, 1951.
3. Roxbee Cox, H. (1951). Some Fuel and Power Projects. *Engineering*, Vol. 172, pp. 726-728, 793-796, 823-825, 1951. Also Trans. I.Mech.E., Vol. 164, pp. 407-424.
4. Keenan, J. H. (1941). *Thermodynamics*. John Wiley, New York, 1941.
5. Kestin, J. and Oppenheim, A. K. (1948). The Calculation of Compressible Fluid Flow by the Use of a Generalised Entropy Chart. Trans. I.Mech.E., Vol. 159, pp. 313-334, W.E.P. No. 43, 1948.
6. Lukasiewicz, J. (1947). Adiabatic Flow in Pipes. *Aircraft Engineering*, Vol. 19, pp. 55-86, 1947.
7. Shapiro, A. H. and Hawthorne, W. R. (1947). The Mechanics and Thermodynamics of Steady One-dimensional Gas Flow. *Journal of Applied Mechanics*, Vol. 14, pp. A317-A336, 1947.
8. Prandtl, L. (1949). *Führer durch die Strömungslehre*. Vieweg, Braunschweig, 1949.
9. Schmidt, E. (transl. Kestin, J.) (1949). *Thermodynamics*. Clarendon Press, Oxford, 1949.
10. Collatz, L. (1951). *Numerische Behandlung von Differenzialgleichungen*. Springer, 1951.
11. Forsyth, A. R. (1929). *A Treatise on Differential Equations*. McMillan, London, 1929.
12. Schelkunoff, S. A. (1948). *Applied Mathematics for Engineers and Scientists*. Van Nostrand, New York, 1948.
13. Bieberbach, L. (1944). *Theorie der Differenzialgleichungen*. Dover, New York, 1944.
14. Frommer, M. (1928). Die Integralkurven einer gewöhnlichen Differenzialgleichung erster Ordnung in der Umgebung rationeller Unbestimmtheitsstellen. *Math. Annalen*, Vol. 99, pp. 222-272, 1928.
15. Kamke, E. (1944). Differenzialgleichungen. Lösungsmethoden und Lösungen. Akad. Verlagsges., Leipzig, 1944.
16. Poincaré, H. (1881, 1882, 1885, 1886). Sur les courbes définies par les équations différentielles. *Jour. Math. Pures et Appl.*, ser. 3, Vol. 7, pp. 375-420, 1881; ser. 3, Vol. 8, pp. 251-296, 1882; ser. 4, Vol. 1, pp. 187-244, 1885; ser. 4, Vol. 2, pp. 151-217, 1886.
17. Perron, O. (1922, 1923). Ueber die Gestalt der Integralkurven einer Differenzialgleichung erster Ordnung in der Umgebung eines singulären Punktes, I and II. *Mathematische Zeitschrift*, Vol. 15, pp. 121-146, 1922; Vol. 16, pp. 273-295, 1923.
18. Dulac, H. (1923). Sur les cycles limites. *Bull. Soc. Math. France*, vol. 51, pp. 45-188, 1923.

Apparatus for the Remote Recording of Flow Conditions

K. W. TODD, M.Eng., A.F.R.Ae.S., A.M.I.Mech.E.
(*Metropolitan-Vickers*)

Summary: An instrument is described which detects total pressure, total temperature, and direction of flow simultaneously in a stream tube of one-sixteenth inch diameter. The observed directions and pressures are transmitted electrically to a remote station where they appear as pencil traces on a paper record which moves at a rate proportional to the traverse rate of the instrument. The temperature is noted at intervals and added manually to the trace. Integrators are included which permit rapid assessment of mean pressure and direction at the conclusion of a traverse, the control and maintenance of setting of the instrument being semi-automatic. A further development is also noted whereby total pressure and direction in three dimensions can be observed either manually, or remotely, by automatic means.

1. Introduction

Instruments for the measurement of flow in restricted spaces such as Cascade Tunnels and experimental compressors have been described by the author in Ref. 1. These instruments were largely manually controlled, but where inaccessible, uncomfortable, or even slightly dangerous operating conditions are unavoidable, or where flow conditions are at high or fluctuating velocities, manual control and observation is a matter of difficulty fraught with inaccuracies due to noise, heat and inaccessibility.

Further development of some of these instruments has therefore been pursued with the aim of achieving automatic control of their setting in the air stream, remote control of their traversing position and remote recording at some distant station of the conditions prevailing in the flow.

The application of such instruments to flow conditions generated by rotating systems such as axial or radial flow compressors as part of the circuit, rather than by external pressure or suction plant, requires more precise knowledge of local temperature than is necessary in the latter plant, since energy is being put into the system. The basic pitot-yawmeter has therefore been adapted to include a thermometric head.

Elaboration of equipment invariably brings increased liability to breakdown, but in the apparatus to be described the chances of failure have been weighed against the many advantages and the recorder has been designed to present a picture of the flow which is orthogonal rather than polar, so being very easily interpreted.

Originally received January 1953.
[The Aeronautical Quarterly, Volume IV, February 1954]

Moreover, the rapid assessment of mean values at the conclusion of a traverse assists greatly in the utilisation of test plant, one of the major problems of the research engineer with limited funds and personnel.

2. Advantages

1. Increased accuracy, since the plot is continuous and the angle setting is always maintained.
2. Repeatability, since the trace can be reversed with reversal of traverse direction.
3. Simplified assessment of results, since the built-in integrators permit rapid calculation of mean values.
4. Instantaneous recording of temperature corresponding to stagnation pressure at a point in the flow.
5. Increase of traverse rate and hence, reduction of testing time, since angle setting is always maintained.
6. Improved operating conditions for personnel, since control is remote from test plant.
7. Greater safety where test plant is being used for research into stress conditions, as well as into aerodynamic conditions.
8. Portability allows application of the apparatus to various test plants.

3. The Measuring Heads

The combined pitot-yawmeter-thermocouple has been developed from an earlier design of cylindrical pitot-yawmeter already described[1]. Its successful construction depended on the manufacture by a firm of tube makers of steel tube of section shown in Fig. 1 and outside diameter 0·070 in. This design of tube having

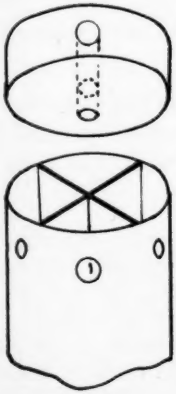

Fig. 1.
Design of pitot-yawmeter-thermocouple head.

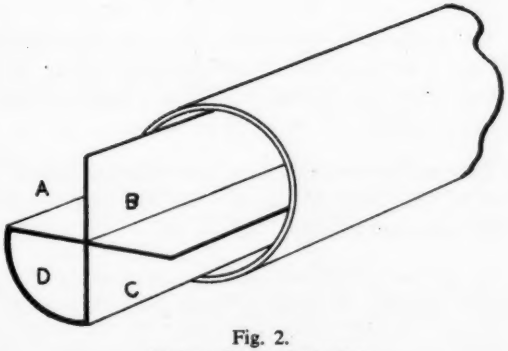

Fig. 2.
Design of two-plane pitot-yawmeter head.

been achieved by the drawing into an outer case of four tubes of quadrantal section, the combined instrument was built up by the addition of a steel end piece brazed to the end of a four way tube and drilled as shown in Fig. 1. Drilling of the forward quadrant then provided a tapping for pitot pressure, the side quadrants were drilled to provide tappings for the setting of direction and the drilling of the end cap fed a sample of air to the rear quadrant, in which was inserted a thermocouple of copper copper-nickel shellac insulated wire.

The included angle of the two yaw holes was 105°, and all four tappings were of 0·010 in. diameter. The four-way tube was sheathed in a stainless steel outer casing for strength purposes, the outer casing starting one inch from the measuring point. By this means an instrument of 8 inches reach, capable of standing up to velocities of the order of 900 ft./sec. was successfully constructed.

Where it was desired to measure direction of flow three-dimensionally, the four-way tube was treated as shown in Fig. 2. The outer case was carefully removed from three of the four quadrants for an axial length of 0·060 in., the complete head being 1·5 in. long. At the rear end of this length a hinge system was constructed so that the head became part of a pantograph linkage, by means of which it could be pivoted about horizontal and vertical axes intersecting at the common leading edge of the diametral dividing walls.

If then the measuring head be placed in an air stream with its axis lying along the direction of flow, the correction of differential pressures between segments *A* and *B* by pivoting about the vertical axis, and between *B* and *C* by pivoting about the horizontal axis, ensured true alignment. Segment *D* then provided a measure of pitot pressure at that point in the flow.

4. Directional Control

Cylindrical yawmeters rely for their control in an air stream on the maintenance of equal pressures in the two yaw holes.

The sensitivity to yaw of the pitot-yawmeter-thermocouple here described was such that a displacement of one degree produced an out-of-balance pressure of 4 per cent. of the velocity head, which at a Mach number of 0·2 was 0·5 in. water and at a Mach number of 0·6 was 5 in. water.

The double yawmeter was rather less sensitive to small angular displacements, giving 2·5 per cent. of velocity head per degree yaw, but this was still enough to allow accurate setting.

It will be understood that manual control of such yawmeters at the higher velocities becomes increasingly more arduous, and an automatic system is desirable.

Two systems were considered and examined experimentally. It was believed preferable to use a "hunting" rather than a "dead beat" control as the latter

inherently tends to come to rest slightly off balance, while a "hunting" control maintains a continuous motion, thus reducing random friction troubles, offering means of controlling "hunt" and indicating at all times that it is functioning.

The dead beat system, tried but discarded, consisted of a loop of heated platinum wire such that change of flow direction across the loop instantaneously involved resistance changes in the bridge circuit of which the loop was a part.

The hunting system finally preferred was made up by photo-electric cells and a small water manometer.

Figure 3 shows the basic system of control. If a light source consisting of a single filament is placed between the legs of a small water manometer and two photo-cells be placed on the outer sides, then the presence of liquid in one leg acts as a cylindrical lens to concentrate light which otherwise disperses. The cell adjacent

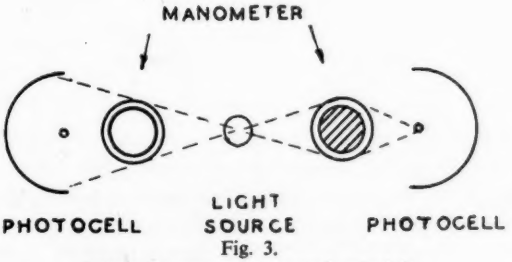

Fig. 3.
Automatic yawmeter control principle.

to the water-filled leg is thus activated more than the cell adjacent to the empty leg. This disturbance of electronic balance is amplified and used to drive a motor which tends, through a gearbox, to correct the setting of the yawmeter and to redress the water displacement in the manometer.

It is interesting to note that since most photo-cells are infra-red sensitive the presence of any liquid other than mercury, even though tinted, acts rather as a concentrator than an obstructor of the operative wavelengths in the light beam. The use of mercury however was unsatisfactory for this control mechanism because of its high density.

The sensitivity of this control was found to be such that a displacement of 0·09 in. water induced full restoring torque in the motor. Thus at a Mach number of 0·2 the response from the yawmeter would be 0·18 degrees and at a Mach number of 0·6 it would be 0·018 degrees.

This high sensitivity was reduced in practice, however, primarily by the pneumatic lag due to the yawholes and secondarily, by the length and bore of the conduits between yawmeter and manometer. Increase of yawhole diameter was limited for practical reasons to not more than one-fifth of the tube diameter and

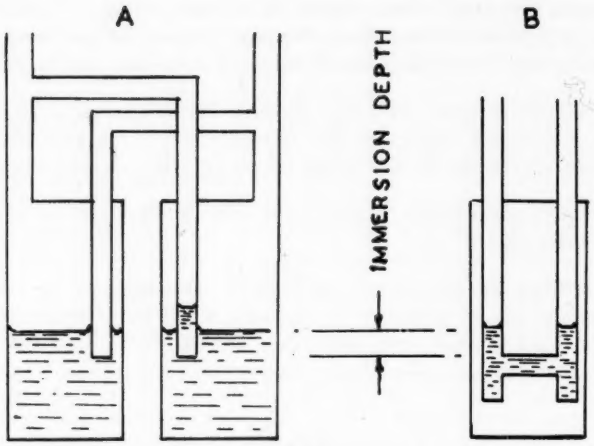

Fig. 4.
Safety-valve systems for yawmeter.

length of the conduits was governed by the necessity to remove the manometer far enough from the yawmeter to mount it in a vibration-free carrier.

Natural hunt of the system lessens with increase of operating velocity and the addition to the circuit of a "feed-back" on the driving motor, such that rate of restoration is proportional to out-of-balance signal, provides a means of reducing hunt when desired.

There is always a risk that when starting up, the yawmeter is so out of setting that a large differential pressure is set up before the control system is fully effective. To prevent this blow-over risk one of the safety devices shown in Fig. 4 was applied. It will be seen that any pressure beyond the pre-set immersion depth causes an air leakage across the system and prevents over-loading.

The selection of an appropriate gear ratio between the control motor and yawmeter depends on effective sensitivity. If too low a ratio is used the motor over-corrects because the full correction is applied before pneumatic lag allows the manometer to swing over, but too high a ratio involves sluggish correction and over-shoot in the manometer. Optimum gear ratio is thus best obtained by experiment and, for the instrument described, was of the order of 4,000:1.

The gear box design was such that the desired ratio was obtained with the minimum number of gears consistent with a compact unit, back lash being thus reduced. Further reduction was achieved by spring-loading the low speed end of the train, *i.e.* the yawmeter. Such loading was permissible by reason of adequate torque from the driving motor and because pneumatic lag was the operative factor in sensitivity, thus reducing the risk of such loading producing an asymmetric hunt condition.

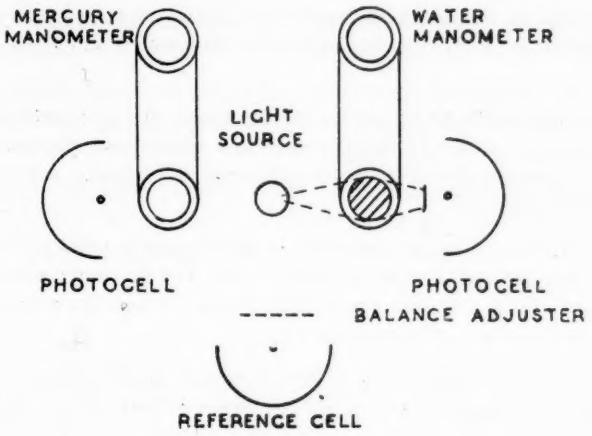

Fig. 5.
Pressure transmission principle.

5. Transmission of Angle Reading

Since in the foregoing system the revolutions of the motor per degree of instrument rotation are calculable once the gear ratio is known, it is possible to include in the gear box at an appropriate ratio a transmitter which will energise a remote follower motor so that it reproduces exactly the transmitter movement.

Such slave systems are usually achieved by D.C. impulses of the order of 12 per revolution, the follower moving in jerks. In the design described here the follower motor rotary movement was translated to linear motion of a pencil on a paper trace, and arrangements were such that one jerk of the pencil corresponded to a yawmeter rotation of less than the limit of angle measurement (say 0·25 degrees). The transmitter speed ratio to that of the instrument, and so to that of the control motor, was thus determined.

6. Transmission of Pressure Reading

There are many known methods of transmitting pressure observations to remote stations, but in the present case the pressure range desired was such that most systems were unsatisfactory.

To accommodate a range of pressure variation from a fraction of an inch water gauge to perhaps 20 inch mercury pressure or vacuum, it was decided to use 40 inch manometers as indicators and to arrange a photo-electric follower of meniscus level as transmitter recorder.

Having in mind the oscillatory nature of the pressures this apparatus was designed to record, it was decided to rely on selected U tubes calibrated against a master manometer so that the reading of the recording pencil against its scale gave

corrected pressure. Should more sensitive recording of pressure be required later, a modification to single leg precision tube manometers could be accomplished simply.

The system employed for the follower is shown in Fig. 5 where it will be seen that the presence of liquid between the light source and photo-cell upsets the electronic balance against a reference cell, since the liquid concentrates the light on to a metal stop.

Two manometers were arranged to have a common chaser and reference photo-cell, the one manometer accepting water and the other mercury, or tetra-bromoethane. The complete chaser was boxed up and chain-driven in vertical guide rails with incorporated balance weight.

The system is sensitive to 0·06 in. differential liquid pressure, response being adequate for the pressure variations encountered, and inertia keeping hunt to negligible proportions.

A driving motor with built-in feed-back operates the chaser and a suitably geared impulse transmitter reproduces motor rotation as inches differential pressure linearly at the recording pencil, the pressure equivalent of one impulse at the pencil being less than 0·10 inches liquid.

In the event of flow conditions lying near the upper limit of the water manometer, a mercury switch is included in the circuit so that it operates a relay to close a valve in the water manometer and switch to the alternative photo-cell follower. At the receiving end the pencil thus takes up a new position relative to its pressure scale, so indicating change in the operative liquid in the manometer. Reduction of pressure below the water manometer limit reverses the process and the pencil reverts to its water-gauge reading.

7. Tip Effect on Pitot-Yawmeter

The nearness of the pitot hole in the pitot-yawmeter-thermocouple to the tip of the instrument has an effect on the accuracy of the pitot pressure observed. Thus an extension beyond the pitot hole of one tube diameter involves a pitot error of 4 per cent. of the operative velocity head, two diameters reduces this error to 1·5 per cent., three diameters to 1·0 per cent., and four diameters to 0·7 per cent. For six or more diameters overhang, the error becomes negligible. This error has been found experimentally to be independent of subsonic Mach number.

8. Traversing the Instrument

The essence of the continuous trace system lies in the maintenance of a steady and uniform traverse rate for the measuring head itself. To this end a mains-operated driving motor was chosen with a built-in gear box such that traverse of the instrument and its holder could be achieved either linearly by rack and pinion, or circumferentially by worm drive, at a rate of about one tenth of an inch per

minute. This traverse rate is governed by the speed of follow of the chaser on the pressure manometer, and by the order of the pneumatic lag in the system.

Traverse limits can be pre-set by arranging micro switches to be operated by the instrument frame after the appropriate travel, and thus to de-energise the driving motor.

An impulse transmitter is again used to transfer instrument position to the receiving station, the following motor in this case being used to drive the paper upon which the two recording pencils operate. Paper movement is about five times that of instrument movement and is achieved by passing the paper between and over the uppermost of two rubber rollers, after which it is held taut by an attached weight.

The result of this paper movement is that an orthogonal plot of pressure and angle appears on a moving paper base in the form of a stepped line, where the length of each side of a step is designed to be less than $\frac{1}{4}°$, or 1/10 inch pressure, or 1/100 inch of instrument movement.

9. Temperature Measurement

The fact that in general the temperature variation is slight during a traverse, makes unnecessary the continuous recording of stagnation temperature, although this could be done by any of the conventional methods. In this design however, successive readings of thermocouple signal on a potentiometer enable temperatures to be added to the paper trace at intervals throughout a traverse, along with any reference temperature which may be desired.

The thermocouple cold junction can be ice if absolute measurement is desired, or it can be the reference temperature if temperature rise or fall is the important factor.

This very small thermocouple relies for its efficiency on the fact that it has little thermal inertia and lies at the end of a long reach instrument remote from random temperatures by conduction. Its recovery factor when tested in a high speed wind tunnel was 100 per cent. at Mach numbers between 0·2 and 0·9.

The control and transmission systems so far described are shown diagrammatically in Fig. 6, where it will be noted that each amplifier contains controls for balancing the zero settings of the pairs of photo-cells and controls for damping hunting by feed-back.

Power supply to the traversing motor, the amplifiers, and the transmitters is all controlled from the recording station, the only pre-operating adjustments necessary being magnitude of feed-back, zero balancing, and traverse length setting.

10. The Receiving Station

As already described, the receiving station consists of a moving paper scale upon which two side-by-side pencils plot pressure and angle simultaneously and orthogonally. The various drives from the follower motors are by gear boxes, chains, and

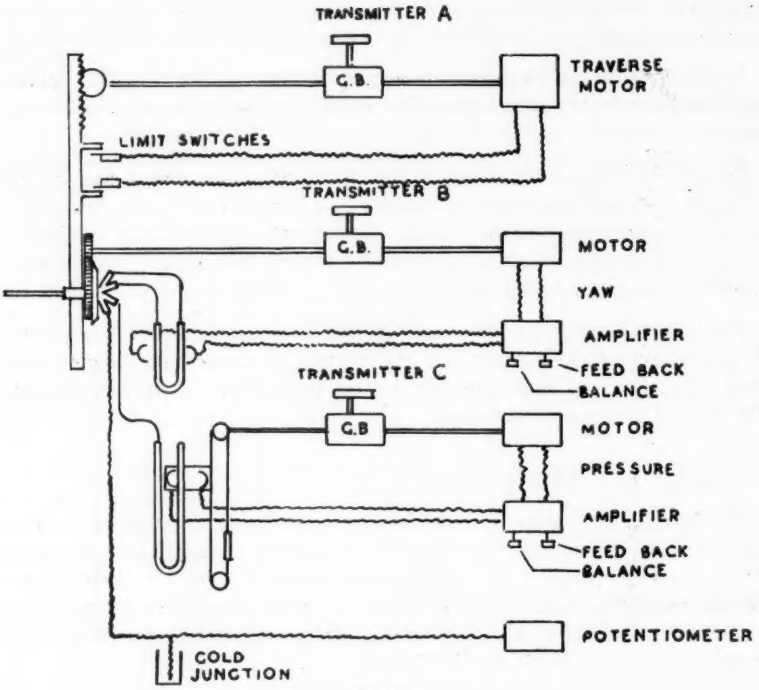

Fig. 6.
Diagrammatic layout of instrument control system.

sprockets with tensioning idler wheels to take up free play. The final drive to each pencil is by cord and pulley, there being a built-in tensioning pulley to eliminate slip at reversal, and to take up cord stretch.

The pencils are carried on trolleys guided by runners, and have attached pointers as indicators at any instant of pressure and angle conditions. In addition the outgoing paper passes under a Perspex screen scribed to enable the reading of the trace in terms of pressure or angle at any time during the run.

The supply roll of paper is prevented from free-running by a small friction brake, and the direction of paper movement relative to instrument traverse movement can be reversed at will.

Traversing can be started, stopped, or reversed from the panel and either pencil or paper can be isolated at any instant if required. The whole system is energised through fuses in the control panel.

In addition there are two integrators built into the recorder so that assessment of mean angle and pressure is simply achieved. Their operating system is as follows.

10.1. The integrators

Two small turntables are driven at a speed proportional to the paper traverse rate by the instrument traverse follower motor. On each of these turntables lies a wheel, the position of whose point of contact from the centre of rotation of the turntable is controlled directly by the position of the appropriate pencil relative to its zero setting. Thus the number of revolutions of the wheel is directly related to the distance of the plotting pencil from zero, and to the length of traverse of the instrument. It is, in fact, the area included by the pencil trace and the zero line, so that wheel revolutions divided by traverse length gives directly mean pressure, or mean angle if corrected by the appropriate calibration factor.

In this recorder an ingenious integrator which was found built into some obsolete aircraft equipment has been included, the wheel being here replaced by two ball bearings and an accurately ground cylinder, the whole assembly being held in series in contact with the rotating turntable by spring tension. The cylinder revolutions are totalled up on counters which can be reset to zero when required and which can be observed through a window in the top of the recorder.

Drive to the integrators from the follower motors is by friction between an appropriate diameter wheel and an emery paper lined shaft held in position by a spring-loaded idler wheel. This system successfully eliminates back lash and reduces integrator movement to a scale suitable to the turntable radius.

The diagrammatic arrangement of the recorder is shown in Fig. 7.

11. Automatic Control of Two-plane Yawmeter

Although this instrument has so far been operated manually, the control system necessary to its automatic operation has been developed as shown in Fig. 8.

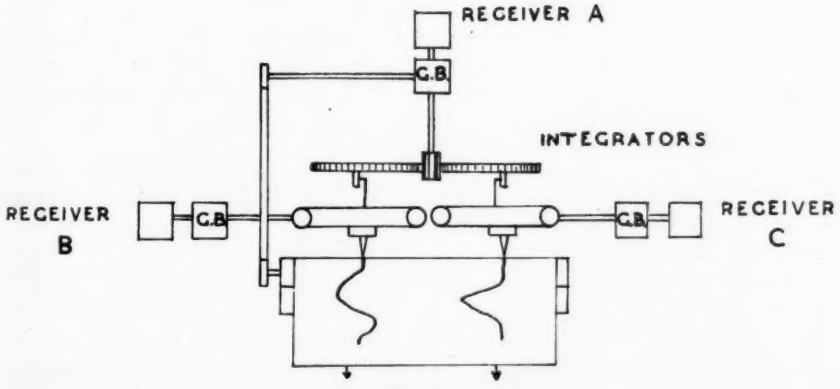

Fig. 7.
Diagrammatic layout of recorder.

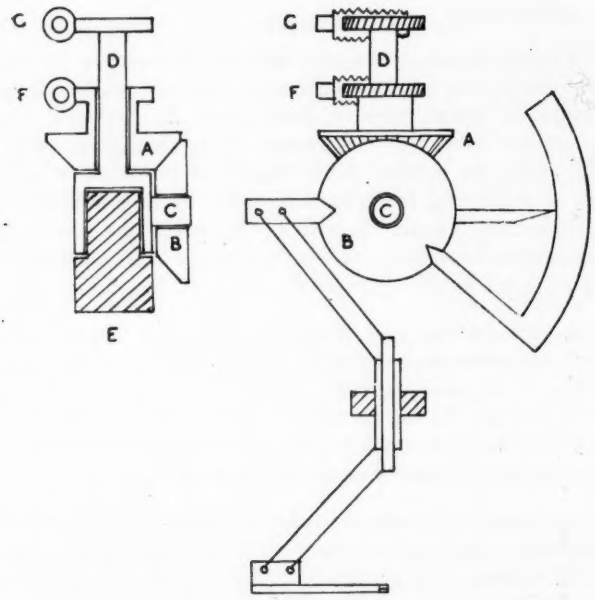

Fig. 8.
Mechanism for controlling two-plane yawmeter.

The pressure balance across each two quadrants can be achieved as in Fig. 3 for the cylindrical yawmeter, but the problem lies in converting the drives from two fixed motors to a pantograph linkage.

In Fig. 8, where the pantograph linkage is sketched, it will be seen that transfer of movement from the measuring head to the mechanism is by way of two concentric tubes, the outer of which is constricted to unidirectional movement; the inner tube carries the four pressure leads from the head. At their upper end the pantograph links are pivoted to a radius arm attached to a bevel wheel *B*, which floats on a spindle *C* attached to a spindle *D*, itself floating on a fixed base *E*. About *D* lies a free bevel wheel *A* intermeshing with *B*.

Pivoting of the instrument head about the horizontal axis is achieved through the pantograph links by a motor driving a worm wheel *F*, which thus rotates bevel *A* and hence, bevel *B*. Pivoting about the vertical axis is by motor drive on to worm wheel *G*, which thus rotates *D* and hence swings *C* and *B* about a vertical axis, taking the complete linkage and the instrument head with it. It will be seen that since the bevel wheels are permanently in mesh, rotation of *B* about a vertical axis also involves its rotation about a horizontal axis, resulting in out-of-balance at the instrument head. This, however, is immaterial since the motor driving *F* immediately compensates, not knowing for what reason out-of-balance occurs.

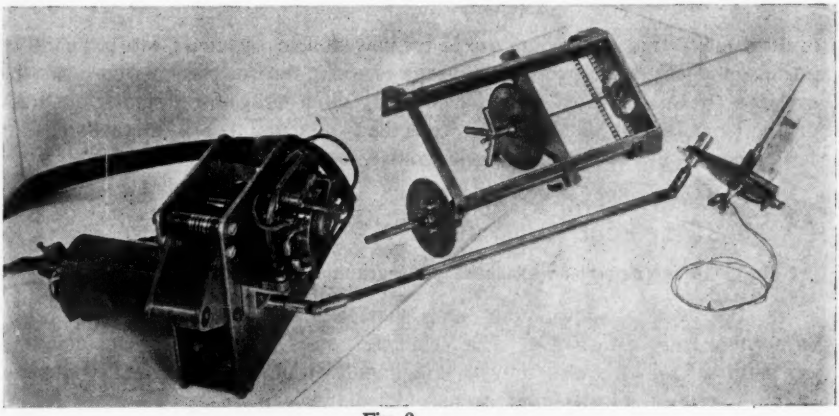

Fig. 9.
Pitot-yawmeter-thermocouple heads with driving gear.

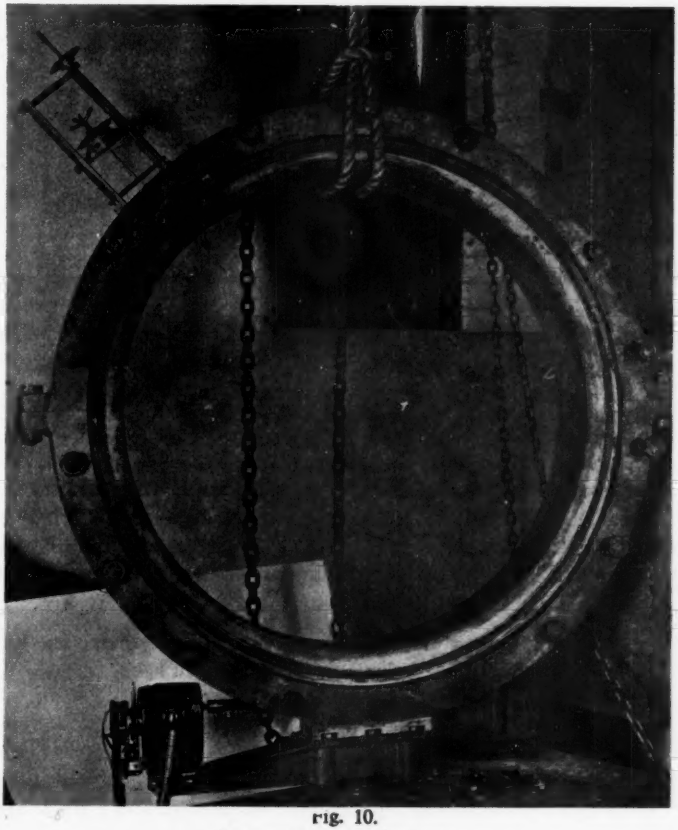

Fig. 10.
Instrument traversing gear.

If required, the two motor drives for this double yawmeter can be made to transmit remotely to the two pencils in the recorder, but for checking purposes the bevel *B* carries a graduated quadrant swinging about *C* against a similar quadrant lying horizontally and centred on *D*. Thus the two quadrants read mutually against each other to indicate vertical and horizontal flow angles.

12. Photographs of Apparatus

The gear described is illustrated photographically in Figs. 9-13.

In Fig. 9 are shown long and short reach combined pitot-yawmeter-thermocouples in their carriers. The Velodyne motor, gear box, and extending link with universal joints is also shown, with impulse transmitter attached. An anti-back-lash spring is also visible on one of the instruments.

Figure 10 shows the long reach instrument attached to the casing of an experimental single stage axial flow compressor. The section of the casing shown contains a carrier ring running on roller bearings and rotated by the motor and worm wheel at the bottom of the photograph. The impulse transmitter from the traverse motor may also be seen.

Figure 11 shows front and back views of the yawmeter control and pressure transmitting gear, together with amplifiers, mercury switch, solenoid valve for isolating the water manometer, and its attendant relay. The photo-cell chaser, driving chain and balance weight and safety valve for the yawmeter manometer are also visible.

Figure 12 shows internal and external views of the portable recorder showing the three follower motors, two integrators, revolution counters, chain drives, pulley drives, pencil trolleys and control panel. Externally the recorder is viewed from the observer's viewpoint showing the Perspex scales, pressure and angle scales, pencil trolleys and pointers with their pulley drives; the paper roller drive is also visible.

The battery of plug sockets attached to the recorder enables the instrument control systems to be plugged in at the traversing station so that 230 volt A.C. is supplied to the amplifier and to a transformer and rectifier from which 24 volt D.C. is fed to the transmitters. Returning signals to the recorder also come through these plug points, so that each section of the equipment can be isolated and removed without impairing the action of the remaining parts.

Figure 13 illustrates the two plane pitot yawmeter as built for manual control with back-lash free pantographic linkage to the measuring head.

13. Accuracy

The apparatus has been used both for low speed tunnel traverses, high speed cascade testing and circumferential traversing at various radii in a single stage axial flow compressor.

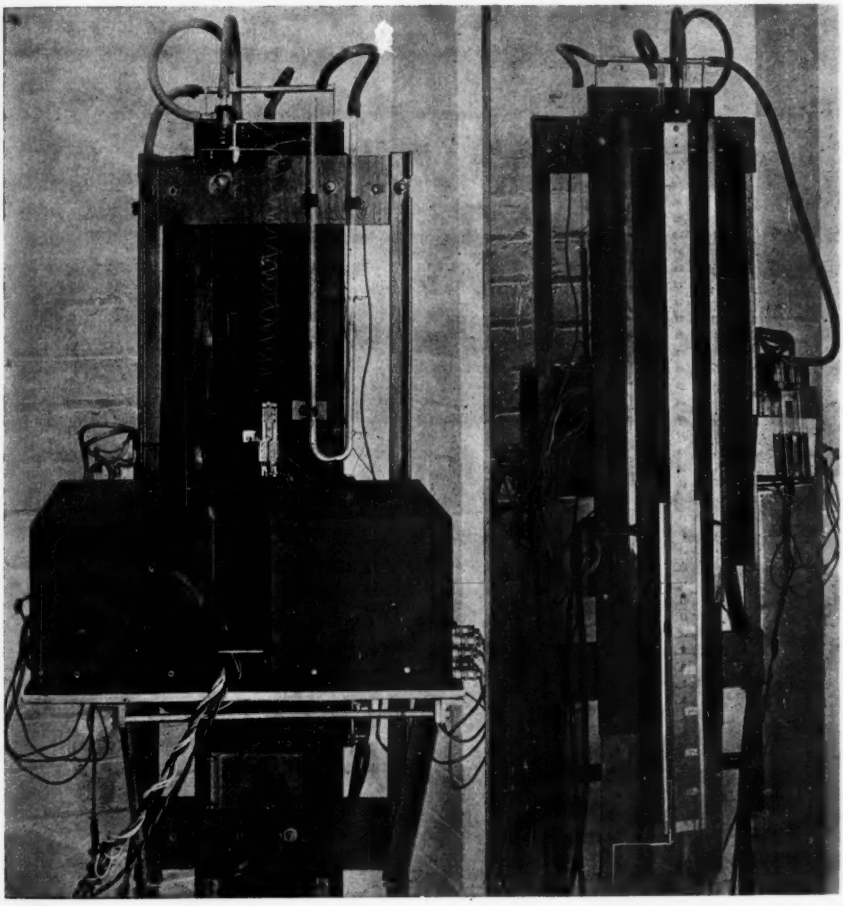

Back view Front view

Fig. 11.
Instrument control gear assembly.

Given consistent flow conditions, traverses can be back-played to yield two indistinguishable traces as far as mean pressure and angle are concerned, although back lash in the traversing motor system sometimes leads to slight phase displacement of the plots.

The yawmeter hunt is normally kept at about 2 degrees total, although at low air speeds it is rather higher. It could well be reduced at these speeds, if desired, by modifying the photo-cell arrangement, but for normal usage 2 degrees is found satisfactory as it assures freedom from sticking in the mechanism. Asymmetry of the hunt about the mean angle is not detectable.

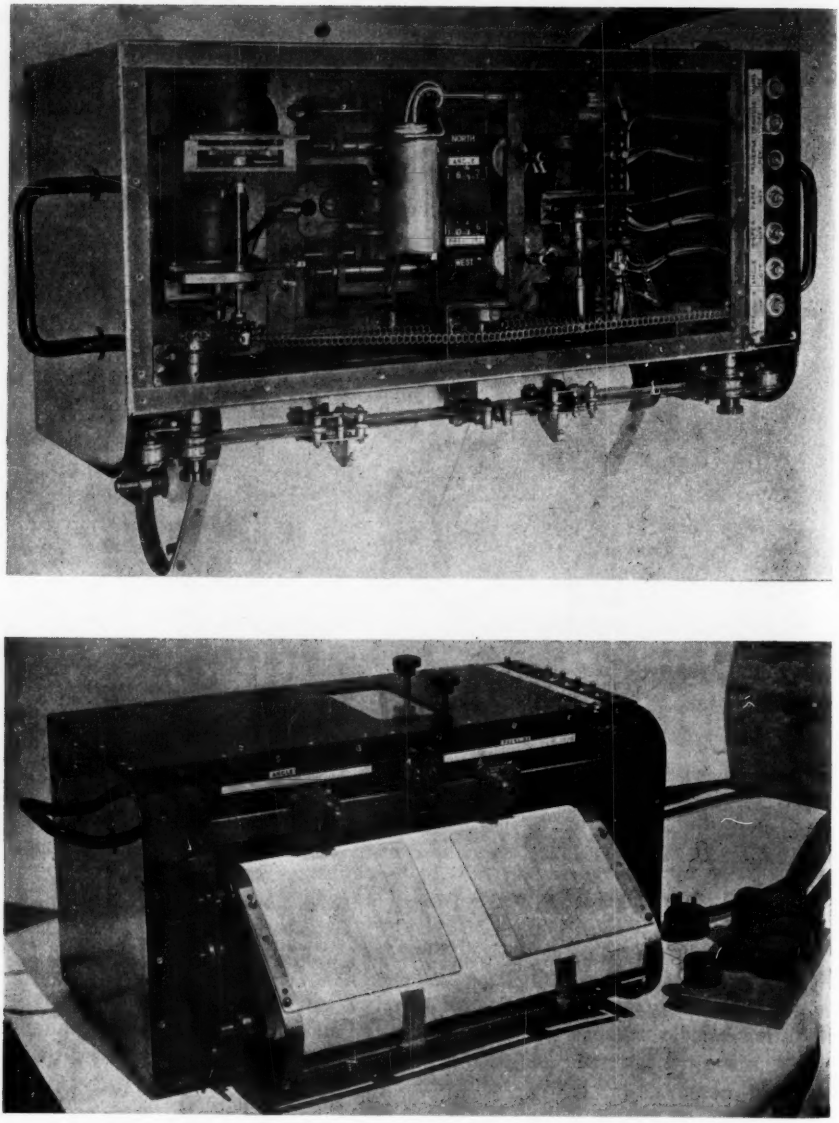

Fig. 12.
Recorder.

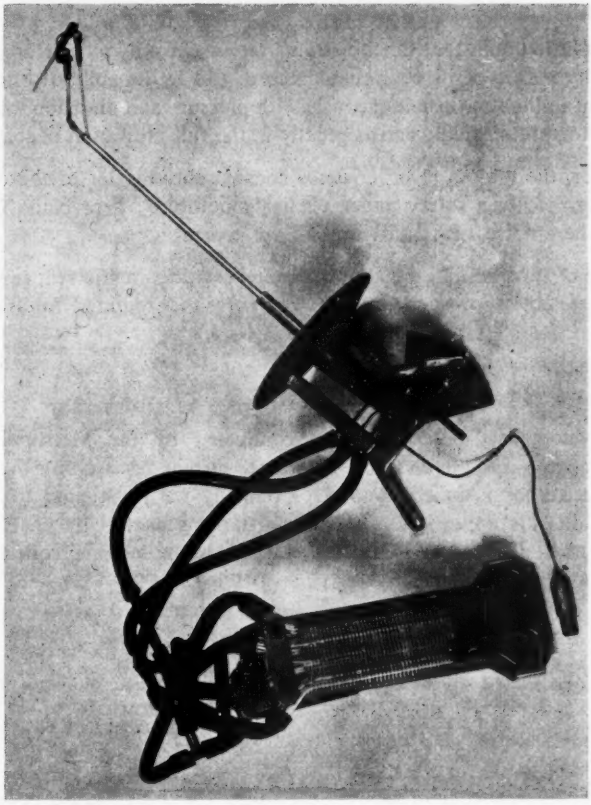

Fig. 13.
Two-plane yawmeter.

The integrators have been checked against planimetered areas and have been found to agree to 0·1 degrees and 0·1 in. of water, provided that their zero settings are carefully adjusted. Failure to do this can be caught up easily by checking the first traverse of a series against planimeter and then applying a zero correction if required.

In a single stage axial flow compressor, radial traverses at inlet have been obtained with this apparatus and used to assess mass flow. The values so obtained have been compared with assessments from segmental traverses downstream of the stage and have consistently yielded agreement within 3 per cent. and often within one per cent., the assessment including compensation for some 25° of swirl in the outgoing flow, and the assumption of uniform static pressure gradient across the annulus.

14. Conclusion

There is little doubt that this apparatus serves not only to increase accuracy of observation by reason of its continuous record, and by its ability to note temperature at a point in the flow instantaneously with pressure and direction, but the ability to assess mean values rapidly assists greatly in the full utilisation of testing time.

Moreover, the remote recorder eases considerably the lot of the observers, as well as adding to their safety under testing conditions where blade failures may occur, and where noise, heat and vibration are present.

The rate of traverse and the automatic angle setting greatly reduces testing time which, in turn, saves power and reduces the personnel required for traversing and computing.

Acknowledgment

The developments described were conducted by the Metropolitan-Vickers Electrical Company Ltd., in connection with gas turbine research for the Ministry of Supply. The author is indebted to the Company for permission to publish this paper, and adds his appreciation of the assistance rendered by G. R. Scholes in connection with all electronic circuiting, and by numerous colleagues during manufacture.

Reference

1. Todd, K. W. (1949). Some Developments in Instrumentation for Air Flow Analysis. *Proc. I. Mech. E.*, Vol. 161, p. 243, 1949.

ERRATUM

Volume IV, Part II, February 1953.

The following correction should be made in Volume IV, Part II of the February 1953 number to "Mixing of Compressible Flows," by F. G. Irving: in equations (5), (8) and (14), replace

$$\left(\frac{L_3}{N_3}\right)^2 \quad \text{by} \quad \left(\frac{N_3}{L_3}\right)^2.$$

INDEX TO VOLUME IV

AERODYNAMICS
See also Gas Dynamics, Noise, Screens and Wind Tunnels.
Aerofoil Theory for Swallow Tail Wings of Small Aspect Ratio, A. Robinson, p. 69 (August 1952).
On the Conditions under which Energy can be Extracted from an Air Stream by an Oscillating Aerofoil, N. C. Lambourne, p. 54 (August 1952).
On the Low Aspect Ratio Oscillating Rectangular Wing in Supersonic Flow, John W. Miles, p. 231 (August 1953).
Some Aspects of Laminar Boundary Layer Separation in Compressible Flow with No Heat Transfer to the Wall, G. E. Gadd, p. 123 (February 1953).
Supersonic Flow Past Wing-Body Combinations, W. Chester, p. 287 (August 1953).
The Distribution of Lift over the Surface of Swept Wings, D. Küchemann, p. 261 (August 1953).
The Dust Problem in Hot-Wire Anemometry, D. C. Collis, p. 93 (August 1952).
The Flow Past Elliptic-nosed Cylinders and Bodies of Revolution in Supersonic Air Streams, D. W. Holder and A. Chinneck, p. 317 (February 1954).
The Sensitivity and Range Required in a Toepler Schlieren Apparatus for Photography of High-Speed Air Flow, W. A. Mair, p. 19 (August 1952).
Note on Mr. Mair's paper, D. W. Holder and R. J. North, p. 51 (August 1952).

CHESTER, W.
Supersonic Flow Past Wing-Body Combinations, p. 287 (August 1953).

CHILVER, A. H.
A Generalised Approach to the Local Instability of Certain Thin-Walled Struts, p. 245 (August 1953).

CHINNECK, A. and D. W. HOLDER
The Flow Past Elliptic-nosed Cylinders and Bodies of Revolution in Supersonic Air Streams, p. 317 (February 1954).

COLLIS, D. C.
The Dust Problem in Hot-Wire Anemometry, p. 93 (August 1952).

COX, H. L. and J. E. FIELD
The Initiation and Propagation of Fatigue Cracks in Mild Steel Pieces of Square Section, p. 1 (August 1952).

DAWSON, L. G.
Flow Changes in Gases in which Mass and Impulse are Conserved, p. 193 (February 1953).

DUCTED FANS
A Note on the Performance of Ducted Fans, Bryan Thwaites, p. 179 (February 1953).

DUST ON HOT-WIRE ANEMOMETERS
See Aerodynamics.

FATIGUE
The Initiation and Propagation of Fatigue Cracks in Mild Steel Pieces of Square Section, H. L. Cox and J. E. Field, p. 1 (August 1952).

FIELD EQUATIONS
The Arithmetic of Field Equations, A. Thom, p. 205 (August 1953).

FIELD, J. E. and H. L. COX
The Initiation and Propagation of Fatigue Cracks in Mild Steel Pieces of Square Section, p. 1 (August 1952).

GADD, G. E.
Some Aspects of Laminar Boundary Layer Separation in Compressible Flow with No Heat Transfer to the Wall, p. 123 (February 1953).

GAS DYNAMICS
See also Wind Tunnels.
Adiabatic One-Dimensional Flow of a Perfect Gas through a Rotating Tube of Uniform Cross Section, K. Kestin and S. K. Zaremba, p. 373 (February 1954).
Flow Changes in Gases in which Mass and Impulse are Conserved, L. G. Dawson, p. 193 (February 1953).

GAUZES
See Screens.

GOODEY, W. J.
Note on the Stabilisation of Long Struts by an Elastic Medium, p. 279 (August 1953).

HOLDER, D. W. and A. CHINNECK
The Flow Past Elliptic-nosed Cylinders and Bodies of Revolution in Supersonic Air Streams, p. 317 (February 1954).

HOLDER, D. W. and R. J. NORTH
Note on Mr. Mair's Paper, p. 51 (August 1952).

INSTRUMENTS AND INSTRUMENTATION
See also Aerodynamics.
Apparatus for the Remote Recording of Flow Conditions, K. W. Todd, p. 401 (February 1954).

IRVING, F. G.
A Note on the Theory of the Constant-Area Mixing of Compressible Flows as Applied to High-Speed Wind Tunnel Design, p. 164 (February 1953).
Erratum, p. 418 (February 1954).

KESTIN, K. and S. K. ZAREMBA
Adiabatic One-Dimensional Flow of a Perfect Gas through a Rotating Tube of Uniform Cross Section, p. 373 (February 1954).

KUCHEMANN, D.
The Distribution of Lift over the Surface of Swept Wings, p. 261 (August 1953).

LAMBOURNE, N. C.
On the Conditions under which Energy can be Extracted from an Air Stream by an Oscillating Aerofoil, p. 54 (August 1952).

MAIR, W. A.
The Sensitivity and Range Required in a Toepler Schlieren Apparatus for Photography of High-Speed Air Flow, p. 19 (August 1952).

METALLURGY
See Fatigue.

MILES, JOHN W.
On the Low Aspect Ratio Oscillating Rectangular Wing in Supersonic Flow, p. 231 (August 1953).

NOISE
On the Noise Emanating from a Two-Dimensional Jet Above the Critical Pressure, Alan Powell, p. 103 (February 1953).
The Influence of the Exit Velocity Profile on the Noise of a Jet, Alan Powell, p. 341 (February 1954).

NORTH, R. J. and D. W. HOLDER
Note on Mr. Mair's Paper, p. 51 (August 1952).

POWELL, ALAN
On the Noise Emanating from a Two-Dimensional Jet Above the Critical Pressure, p. 103 (February 1953).
The Influence of the Exit Velocity Profile on the Noise of a Jet, p. 341 (February 1954).

ROBINSON, A.
Aerofoil Theory for Swallow-Tail Wings of Small Aspect Ratio, p. 69 (August 1952).

SCHLIEREN PHOTOGRAPHS
See Aerodynamics.

SCREENS
On the Resistance of Screens, K. E. G. Wieghardt, p. 186 (February 1953).

SQUARES, METHOD OF
See Field Equations.

STRUCTURES
A Generalised Approach to the Local Instability of Certain Thin-Walled Struts, A. H. Chilver, p. 245 (August 1953).
Buckling of Oblique Plates with Clamped Edges under Uniform Compression, W. H. Wittrick, p. 151 (February 1953).
Correlation Between some Stability Problems for Orthotropic and Isotropic Plates under Bi-Axial and Uni-Axial Direct Stress, W. H. Wittrick, p. 83 (August 1952).
Note on the Stabilisation of Long Struts by an Elastic Medium, W. J. Goodey, p. 279 (August 1953).

SWALLOW TAIL WINGS
See Aerodynamics.

THOM, A.
The Arithmetic of Field Equations, p. 205 (August 1953).

THWAITES, BRYAN
A Note on the Performance of Ducted Fans, p. 179 (February 1953).

TODD, K. W.
Apparatus for the Remote Recording of Flow Conditions, p. 401 (February 1954).

WIEGHARDT, K. E. G.
On the Resistance of Screens, p. 186 (February 1953).

WIND TUNNELS
A Note on the Theory of the Constant-Area Mixing of Compressible Flows as Applied to High-Speed Wind Tunnel Design, F. G. Irving, p. 164 (February 1953). *Erratum*, p. 416 (February 1954).
The Second Order Terms in Two-Dimensional Tunnel Blockage, L. C. Woods, p. 361 (February 1954).

WITTRICK, W. H.
Buckling of Oblique Plates with Clamped Edges under Uniform Compression, p. 151 (February 1953).
Correlation Between some Stability Problems for Orthotropic and Isotropic Plates under Bi-Axial and Uni-Axial Direct Stress, p. 83 (August 1952).

WOODS, L. C.
The Second Order Terms in Two-Dimensional Tunnel Blockage, p. 361 (February 1954).
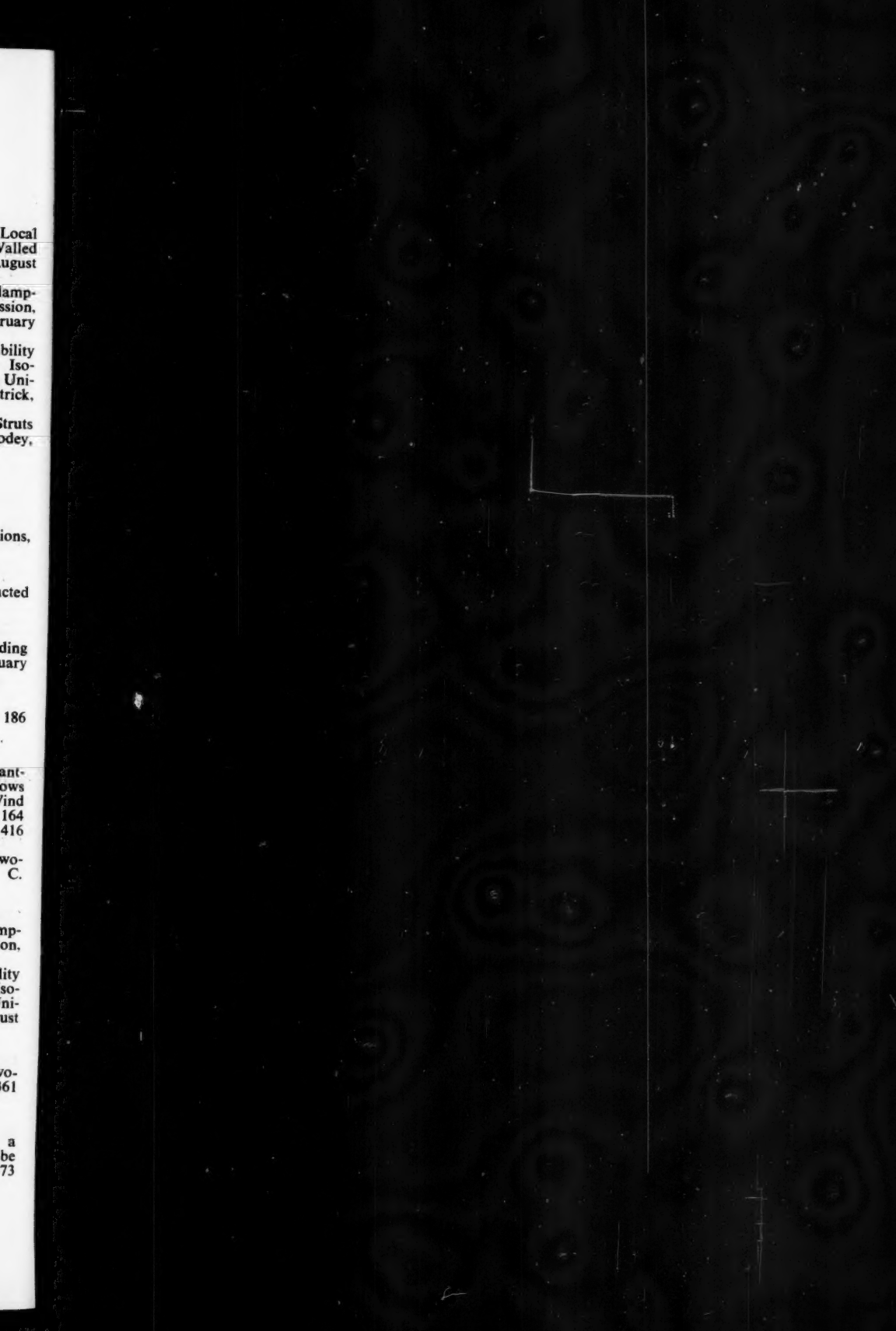
ZAREMBA, S. K. and K. KESTIN
Adiabatic One-Dimensional Flow of a Perfect Gas through a Rotating Tube of Uniform Cross Section, p. 373 (February 1954).